BOUNDARY-INTEGRAL STUDY OF VISCOUS DROPLETS IN COMPLEX GEOMETRIES

by

Rocío Navarro Vázquez de Parga

B.S., Universitat Rovira i Virgili, 2013

M.S., Universitat Rovira i Virgili, 2015

A dissertation submitted to the

Faculty of the Graduate School of the

University of Colorado in partial fulfillment

of the requirement for the degree of

Doctor of Philosophy

Chemical Engineering

2020

Robert H. Davis

Hendrik Heinz

Michael R. Shirts

Franck Vernerey

Alexander Z. Zinchenko

Navarro Vázquez de Parga, Rocío (Ph.D., Chemical Engineering)

Boundary-Integral Study of Viscous Droplets in Complex Geometries

Dissertation directed by Prof. Robert H. Davis and Dr. Alexander Z. Zinchenko

Abstract

Emulsions are present in multiple aspects of our everyday life, from food – mayonnaise, milk or vinaigrette -, to healthcare products – topical ointments or lotions -, to a broad variety of other products – ink, paints, insecticides, etc. An emulsion is a colloid of two or more immiscible liquids, where one liquid is dispersed in the form of drops in another liquid. The objective of the present dissertation is to describe the dynamics of the motion and deformation of those drops in narrow channels. Computational methods are developed and applied in different complex geometries that represent devices used in droplet microfluidics and emulsification.

A moving-frame, boundary-integral algorithm is presented, which makes it possible to follow a three-dimensional viscous droplet travelling through two- and three-dimensional microchannels. The behavior of a droplet, including its deformation and breakup conditions, is studied when moving through a T-shaped channel, different constricted membrane pores, or a channel with finite depth (3D).

The effect of the physical properties of the drop (i.e., size relative to the channel, capillary number and viscosity ratio with respect to the carrier fluid) on the different outcomes of each problem are studied, as well as the influence of the system characteristics (i.e. channel geometry, flow rates, depth).

When placed in one of the lateral branches of a T-channel, the drop behavior is strongly affected by the volumetric flow ratio between the outlets, exiting the channel through the branch with a larger flow. For cases with a flow ratio not far from unity, when the drop hits the corner and reaches impending breakup, the size of each daughter drop is calculated. Breakup occurs more frequently for drops with larger size and capillary number.

When a drop goes through a constricted pore, its fate is related to the pore geometry. Little to no breakup is observed in H (rectangular)- and circular-constricted pore networks, while drops always break (until they reach a critical size) in pores with Y-bifurcations.

The drop motion varies depending on the nature of the channel where it is travelling. When a third dimension is added to the geometry (i.e. channel depth), the drop is affected by two competing effects: (1) the imposed flow is higher near the middle of a channel with lower depth, causing the drop to move faster, and (2) the front and back channel walls causes more viscous drag and slow down the drop motion, especially in the case of larger drops. Thus, the drop velocity is maximized for channels of intermediate depth.

Finally, results obtained from experimental work are compared to the results obtained with the boundary-integral algorithm for a T-shaped channel and a cross-shaped channel. The algorithm is shown to successfully predict and reproduce the drop motion and deformation in the studied cases, especially in the simulations with three-dimensional channels.

para mamá, papá, y Garret

Acknowledgments

This thesis becomes a reality thanks to the kind support and help of many individuals. I would like to extend my sincere thanks to all of them.

Foremost, I would like to express my sincere gratitude to my advisor Prof. Davis for the continuous support of my Ph.D. and for imparting his knowledge and expertise, but most importantly, for his understanding, and for believing in me and pushing me farther than I thought I could go.

I would like to express my special gratitude to Dr. Zinchenko for his infinite patience during our meetings, email threads, “fights”… and, of course, for his infinite knowledge. I feel honored that he kindly shared a piece of it with me.

To Jake, Gesse, Noemí and Albert, for sharing their knowledge in our discussions at the office (and out of it) and for always being there to help.

To Cassy, Jenny and Ann, for all their hard work. I hope they learned from me as much as I learnt from them.

To all my friends and family in Spain, for supporting me from the distance and for helping me survive all the stress and craziness and not letting me give up. I never imagined a simple video-call could be so powerful.

To the friends I made here, for making me feel at home.

I would like to thank Pete Balsells for believing in young talents and making my dream of studying in one of the best universities in the world come true.

Last but not the least, I am very thankful to the members of my committee Prof. Davis, Prof. Heinz, Prof. Shirts, Prof. Vernerey and Dr. Zinchenko for having accompanied me during this journey, for their guidance and for sharing their wisdom, expertise and time.

Table of Contents

List of Figures

Chapter I

Introduction

1.1. What is an emulsion and why are they important?

Emulsions are mixtures of two or more immiscible liquids, where one liquid is dispersed in the form of drops (dispersed phase) in another liquid (continuous phase) (Becher, 1965). Due to their broad range of applicability, several authors have studied the conditions behind emulsion formation (Adams & Walstra, 1998; Bobra, 1990; Fingas et al., 1993; Fingas, 1995; Leal-Calderon, Schmitt, et al., 2007; Walstra, 1993).

Historically, emulsions were created using shear or impact stresses generated by agitation. However, those methods do not provide size-homogenous mixtures, so other methods like membrane emulsification (Giorno et al., 2009) or microfluidic emulsification (Shah et al., 2008) that allow controlled production of uniform droplets have been developed in the past decades. This improvement is very relevant in medical research (Sackmann et al., 2014), biological and chemical analysis (Kawakatsu et al., 1997; Mason & Bibette, 1997; Nakashima et al., 2000) and physics (Leal-Calderon, Thivilliers, et al., 2007), since these disciplines require well-characterized, miniaturized systems that can be achieved with microfluidics.

Microfluidics is the science and engineering that studies the flows that circulate in microsystems. Flows can be simple or complex, mono- or multiphasic, and their behavior is governed by the small length scale of the system (Nguyen et al., 2019; Tabeling, 2005). Nowadays, microfluidics is a technology that entails an important source of innovation in several fields of

study, as it explores both applications and commercialization, reducing the costs from working in large scales (Mashaghi et al., 2016).

The branch of microfluidics that studies drop generation and behavior through immiscible flows inside microchannels is known as droplet microfluidics (Mashaghi et al., 2016; Teh et al., 2008). This subcategory has a broad range of applications, like oil recovery (Huang & Varadaraj, 1996), in the pharmaceutical industry (Khan et al., 2011) for drug delivery (Nakano, 2000; Vasiljevic et al., 2006), and in food industry (Leal-Calderon, Thivilliers, et al., 2007; Muschiolik, 2007), amongst others (Shah et al., 2008). Depending on the motivation, interest in drop manipulation can be divided in two categories (Baroud et al., 2010): the first one consists on using microfluidics to produce droplets in a controlled and uniform manner – material science applications, food industry, pharmaceutical industry, etc. - (Shah et al., 2008; Umbanhowar et al., 2000). The second motivation is related to lab in a chip applications, where drops can operate as micro-reactors (H. Song et al., 2003; Tawfik & Griffiths, 1998). In both cases, being able to describe and predict droplet dynamics is crucial, however, the dynamics of drop motion, deformation and breakup are complex in these type of systems. For this reason, the study of drop motion dynamics in complex microchannels was chosen for this research.

1.2. Prior work

The dynamics of drops in microchannels and other complex networks has been extensively studied. In early studies, Taylor (1932) extended Einstein's expression for the viscosity of a shearing fluid containing solid spheres so that it can be used with drops. He also studied the deformation of a drop produced by the viscous forces exerted by another surrounding fluid (Taylor, 1934). Pan & Acrivos (1968) studied the shape of a gas bubble or liquid drop moving in

an unbounded viscous medium at low Reynolds number. In their study, they concluded that inertial forces did not affect the shape of the bubble and had a minor effect on drop deformation. Hetsroni et al. (1970) provided a solution for the flow field around a spherical droplet moving through a long circular tube containing a Poiseulle flow. Higdon & Muldowney (1970) developed a method for solving the Stokes equations via a spectral element discretization of the boundary-integral (BI) equation for rigid particles and deformable drops. Barthes-Biesel & Acrivos (1972) obtained a theoretical method for predicting the deformation and breakup conditions of a freely-suspended drop in a shear field. They compared their numerical results with available experimental data and found good agreement between them. Haber et al. (1973) studied the internal and external creeping flow of two spherical drops moving along their line-of-centers and presented the numerical results obtained. Rallison & Acrivos (1978) studied the deformation and breakup conditions of a freely-suspended viscous drop in an immiscible shear flow at zero Reynolds number. They formulated the problem as an integral equation for the velocity on the drop surface and solved it numerically. Levan (1981) developed a general solution for the motion of a spherical drop moving through an unbounded Newtonian fluid. Uijttewaal et al. (1992) used a boundary-integral (BI) technique to study the motion of a deformable drop in a shear flow close to a fixed wall. Stone (1994) described the drop deformation and breakup in a viscous flow at low at Reynolds number and provided a summary of investigations related to drop breakup in externally-imposed flows.

Over the last century, several authors demonstrated that the boundary-integral (BI) method (Pozrikidis, 1992) is a reliable technique for the analysis of flows at low Reynolds number. Professor Davis' research group has greatly contributed to advances in the study of single and multiple drop behavior in different scenarios using boundary-integral techniques. Some decades ago, Zinchenko et al. (1997) developed a new three-dimensional boundary-integral (BI) algorithm

for buoyancy-driven motion of deformable drops in viscous media at low Reynolds numbers. They included an iterative method for mean curvature calculation that improved the contour integration schemes. They also created a curvatureless 3D boundary-integral algorithm for interacting deformable drops in Stokes flow that can be used to analyze very large drop deformations and impending breakup situations (Zinchenko et al., 1999). In 2000, they developed a hybrid of boundary-integral method and economical multipole techniques algorithm to perform dynamical simulations of multiple drops with strong interactions at zero Reynolds numbers (Zinchenko & Davis, 2000). Later on, they studied the squeezing and trapping conditions of a freely-suspended deformable drop through a constriction formed by solid particles (Zinchenko & Davis, 2006). Griggs et al. (2007) analyzed the motion and deformation of a three-dimensional deformable drop between two parallel plane walls in a low-Reynolds-number, Poiseuille flow for different conditions (drop size, viscosity, initial position, etc.). Zinchenko & Davis (2008) simulated the squeezing of a drop contained in a periodic, highly concentrated emulsion through a cubic array of solid particles, emulating the drop-solid interaction of an emulsion flow going through granular materials. Related to drop squeezing as well, they simulated a deformable drop through a ring constriction using an axisymmetric boundary-integral algorithm based on the Hebeker representation (Hebeker, 1986) for the solid-particle contribution (Ratcliffe et al., 2010). For the same problem, they determined the shape of a drop trapped in the ring constriction (Ratcliffe & Davis, 2012) using an algorithm they developed (Ratcliffe et al., 2012) based on local deviation from the Young–Laplace equation and the adjacent solid shape relative to the trapped drop. In 2013, they developed a multidrop-multiparticle algorithm to simulate the squeezing of a concentrated emulsion through a randomly packed granular material at low Reynolds numbers (Zinchenko & Davis, 2013).

More recently, several other groups also explored the dynamics of drop behavior both experimentally and theoretically. Nisisako et al. (2002) were able to create a method to produce regular-sized droplets at a uniform speed in a microchannel network with a T-junction. On the same topic, Link et al. (2004) demonstrated two methods for breaking larger drops into daughter droplets in simple microfluidic configurations (a T-junction and isolated obstacles). However, they asserted that no microfluidic technology existed to control the size distribution of the daughter droplets. Cristini & Tan (2004) reviewed theoretical and numerical work about droplet deformation, breakup and coalescence related to drop generation and manipulation in microfluidics, concluding that simulations are a powerful tool in microfluidic design because they allow to explore different channel geometries and flow conditions. They also emphasized the importance of investigating a topic where previous studies have been limited: the interactions between the drop and the channel walls. Squires & Quake (2005) presented a review of the physics of microfluidics and expressed the importance of some dimensionless numbers in physical phenomena. They explained the importance of microfluidics in the large-scale automation of chemistry and biology, where viscous flows and small dimensions have a significant presence. On that note, Günther & Jensen (2006) also analyzed the transport characteristics of pressure-driven flows through microchannel networks, summarizing useful dimensionless parameters useful in the characterization of multiphase flows. Labrot et al. (2009) focused on understanding drop dynamics by studying the effective hydrodynamic resistance of drops in microchannels using a new method based on the analysis of droplet trajectories. Chung et al. (2010) studied, both experimentally and numerically, the dynamics of a drop going through obstructions in a microchannel and the effects of various physical parameters on the final outcome. Baroud et al. (2010) studied the progress and physical knowledge of drop formation, transport and merging. Some of the techniques have been

standardized, contributing to progress in drop microfluidic applications. Carlson et al. (2010) described the drop dynamics in a bifurcating channel using the Phase Field theory (Sekerka, 2001). They studied the motion of a drop in a bifurcating channel, identifying to regimes depending on the outcome: splitting and non-splitting. The authors suggested the study of the importance of the effects of the tip geometry and multiple drop works. Casadevall i Solvas & De Mello (2011) emphasized the importance of drop microfluidics in large-scale experimentation and summarized recent advances in the field. Jose & Cubaud (2014) performed an experimental study of drop production and transport in microchannels. Hoang et al. (2018) studied the dynamics of a drop in a contraction microchannel via three-dimensional numerical simulation and theoretical analysis and classified the outcome in three regimes as a function of the Capillary number (Ca) and concentration ratio (C): trap, squeeze and breakup. Bhardwaj et al. (2018) used the S-C lattice Boltzmann method to study the motion of a drop in a microchannel having a construction and showed that the drop dynamics are strongly affected by the capillary number.

1.3. Context and applications of current work

In this work, a boundary-integral (BI) algorithm is used to describe and predict drop motion and deformation in different channel geometries that represent devices used in droplet microfluidics and emulsification. The motion of small droplets through microfluidic channels, membrane pores, and other confined geometries presents considerable computational challenge due to drop deformation, small drop-wall clearances, and complex geometries. The objective of this work is to simulate the motion and deformation of a freely suspended, three-dimensional (3D), viscous drop inside channels with different two- and three- dimensional geometries that contain a Stokes flow. To do so, a moving-frame (MF) (Zinchenko et al., 2012) boundary-integral (BI)

(Pozrikidis, 1992) method is used, so integration is required only at the interfaces between the fluids (drop and carrier) or boundaries (fluid-wall), which allows for higher accuracy and performance (compared to finite-element method (FEM) or volume of fluid (VOF) method).

Interest in droplet microfluidics has raised in the past decade because of the advantages of low fabrication costs, reduced analysis times, small sample volumes, analytical efficiency and easy automation (Chou et al., 2015; Dressler et al., 2014). With the novel boundary-integral algorithm presented in this thesis, it is possible to characterize the dynamics of drop motion, deformation and breakup (and accurately predict the size of the daughter droplets) in different complex channel networks.

Channels with junctions are commonly used to provide control over droplet size, shape and path. The results presented in Chapters 2 & 4 of this dissertation can be used in the fabrication of low-cost, disposable, easy-to use, single-drop (He et al., 2005; Lorenz et al., 2006) microfluidic devices for use in medical diagnostics (Myers & Lee, 2008; Sato et al., 2008; Weigl et al., 2008; Zhao & Van Den Berg, 2008) for cell control –drop sorting and tracking, drug delivery –drop sorting and breakup-, amongst others. In the food industry, encapsulation, food processing, targeted delivery to specific areas in the digestive tract, and controlled release, are common applications (Maan et al., 2015; Shewan & Stokes, 2013) that can be described and enhanced with both of the algorithms here presented (for infinite- and finite-depth channels).

The immediate application for the results presented in Chapter 3 falls on any industry where emulsion filtration and/or premix membrane emulsification are used. The size and distribution of the daughter droplets after filtration in a Y-bifurcation pore is provided in the chapter. Preparation of uniform-sized emulsions has applications in the pharmaceutical science and technology in the area of drug-delivery-systems (Allen & Cullis, 2004; Liu et al., 2011) where

a narrow size distribution of drops gives better control over the released dose, and drugs can be in the form of proteins, virostatics, antibiotics, etc. Premix membrane emulsification is used in the food industry as well (Charcosset, 2009; Ramakrishnan et al., 2013; Surh et al., 2008), where water-in-oil and oil-in-water emulsions are widely used in food preparation.

Finally, the results obtained in Chapter 5 can be used as a starting point on the design of experiments to obtain different drop shapes, which affect the emulsion properties and functionality, and, therefore, its applications. Drop shape manipulation is important, for example, in the food industry for food and vitamin encapsulation to enhance their storage (Abbas et al., 2012; Desai & Jin Park, 2005; Dhakal & He, 2020; Sadek et al., 2013), or in the pharmaceutical industry (Ré, 2006; Vehring, 2008) for drug delivery, in the controlled release of vaccines, or in the production of intravenous or intramuscular injectables, amongst others.

1.4. Dissertation overview

In this section, a brief explanation of the work exposed in each of the remaining chapters of the thesis is presented.

1.4.1. Chapter 2: Boundary-integral study of a freely suspended drop in a T-shaped microchannel

In Chapter 2, a novel boundary-integral algorithm for the study of the motion and deformation of three-dimensional (3D) viscous drops in two-dimensional (2D) channels (i.e. channels with infinite depth) is presented and validated. The algorithm is used to determine the physical conditions under which a drop that is introduced in a T-shaped microchannel will go as a whole through one of the channel branches or will break into daughter droplets and split between two branches. A critical capillary number or size ratio is observed, below which the drop does not break. Above the critical value, the range of flow ratios over which impending breakup is predicted

increases with increasing capillary number and size ratio. For equal or similar flow rates between the branches, the volume partition ratio is essentially unity even though the geometry is asymmetric. When the flow rates between the ranches are different, the one with higher flow rate registers larger a volume partition, especially in the case of smaller drop sizes and capillary numbers. The viscosity ratio has a small but noticeable effect, with drops of similar viscosity to the carrier fluid breaking most easily.

1.4.2. Chapter 3: Simulation of drop motion and breakup in narrow pores

In Chapter 3, the study of the motion and possible breakup of 3D viscous drops passing through infinite-depth model membrane pores is presented. Three different pore geometries are studied (Y-bifurcation, H-constriction and circular constriction), and the drop behavior is classified into three different cases: no-breakup, direct breakup due to contact with a pore bifurcation and indirect breakup due to elongation. Pore geometry has a strong effect, with relatively little breakup when there is no bifurcation, regardless of the drop size and capillary number. Direct breakup was not observed for droplets in the H and circular constricted-pore networks. The distribution of droplet sizes after going through the pore is calculated for the geometry with a Y-bifurcation, which is relatively broad when the pre-pore size of the parent drops is large, but the post-pore size distribution is narrow for smaller parent drops (due to little or no breakup).

1.4.3. Chapter 4: Boundary-integral study of a viscous drop in three-dimensional channels

In Chapter 4, a new method is developed to describe the motion of 3D viscous drops in finite-depth channels. The analytical solution of Boussinesq (1868) for undisturbed flow in rectangular channels is used at the entrances and exits. It is also used on the moving-frame boundary to compare drop velocities in long, straight channels with different depths for droplets of size comparable to the channel depth and width. Larger drops that nearly fill the channel cross-

section register slower velocities than smaller drops in narrow channels due to the no-slip condition on the walls, since the drop is affected not only by the forces exerted by the imposed flow but also by hydrodynamic forces exerted by the channel wall; smaller drops are not affected by the proximity to the walls and travel faster in narrow channels due to the larger velocity at the center of the channel. Therefore, drop velocity has, for a given capillary number, relative radius and viscosity ratio, a maximum when, contrarily as what could be expected, the ratio between the channel height and depth is larger than the unity due two, competing effects. Then, the effect of the channel depth on the behavior of a droplet inside a channel with a Y-bifurcation is presented. The results show that the drop volume partition ratio is affected when the flow going through each channel branch is considerably different.

1.4.4. Chapter 5: Experiments on drops in microchannels

In Chapter 5, the steps followed to perform experiments to observe the drop motion and deformation inside a T-shaped channel and a cross-shaped channel are explained. The experiments were performed at the University of New South Wales (UNSW) in Australia during my visit at the laboratory of Professor Patrick Spicer. The results obtained from the experimental work were compared to the results obtained computationally (later dimensionalized) for two- and three-dimensional channels. Good agreement was obtained between the observed drop shapes and the simulations. The best agreement is when using the finite-depth-channel simulation algorithm of Chapter 4, as it accurately represents the 3D geometries used in the experiments.

1.4.5. Chapter 6: Concluding remarks

In Chapter 6, a summary of the most important findings of the work performed in the previous chapters is presented. The boundary-integral algorithm has been shown to accurately describe the motion of a drop in different channels. Drop properties have a large effect on the

outcomes of the different problems, but channel characteristics (i.e. geometry, flow rates, depth) are even more influential. A list of future work is also provided. Drop breakup and the subsequent motion and fate of the daughter drops is an interesting topic that should be considered in future studies.

Chapter II

Boundary-integral study of a freely suspended drop in a T-shaped microchannel

This work has been published in the *International Journal of Multiphase Flow*:

Navarro, R., Zinchenko, A. Z., & Davis, R. H. (2020). Boundary-integral study of a freely suspended drop in a T-shaped microchannel. *International Journal of Multiphase Flow*, 103379. https://doi.org/10.1016/j.ijmultiphaseflow.2020.103379

Abstract

The motion of small droplets through microfluidic channels, membrane pores, and other confined geometries presents considerable computational challenge due to drop deformation, small clearances, and complex geometries. This paper addresses the challenge by developing a moving-frame boundary-integral method and demonstrating its utility with simulations of a three-dimensional, freely-suspended deformable drop moving through a T-shaped microchannel at small Reynolds number. The drop size is comparable to the channel height, which is much smaller than the channel depth. The drop is fed into a straight channel or arm of the T-junction, with prescribed flow ratio through the other two branches. This setup typically results in strong drop interaction with the furthest corner of the junction. For computational efficiency, the base flow in the channel without the drop is first determined. Then, a "moving-frame" or computational cell around the drop is dynamically generated, using the first solution to provide the fluid velocity on the cell

boundary. This method is used to map the outcomes (movement into one branch or the other, or breakup and partitioning between the branches) as a function of the flow ratio between the two branches and the drop capillary number, size relative to the channel height, and viscosity ratio with the carrier fluid. A critical capillary number or size ratio is observed, below which the drop does not break. Above the critical value, the range of flow ratios over which impending breakup is predicted increases with increasing capillary number and size ratio. The volume partitioning in the range where breakup occurs is essentially unity for equal flow rates between the two branches, even though the geometry is asymmetric, and then the volume partition of the daughter drops favors the branch with higher flow rate and with a stronger dependence on the flow ratio for the smaller drop sizes and capillary numbers. The viscosity ratio has a small but noticeable effect, with drops of similar viscosity to the carrier fluid breaking most easily.

2.1. Introduction

2.1.1. Problem summary and importance

In this paper, we develop an efficient boundary-integral algorithm that allows us to simulate the pressure-driven flow and motion of a deformable drop through a complex junction at small Reynolds number. The drop is neutrally buoyant and its size is comparable to the channel height; the drop viscosity may differ from that of the carrier fluid. It is assumed that the channel depth or width is much greater than its height, and that it has planar walls, so that the flow in the channel in the absence of the drop is essentially two-dimensional (2D). We are interested in the shape that the drop will achieve during the process, its breaking conditions, whether or not it becomes stuck, and the path it will take inside a microchannel. This study permits us to determine the behavior that a drop might exhibit inside a microchannel, including if and how it breaks inside the channel (which

could be used in emulsification or medical applications such as the release of drugs inside the circulatory system), its residence time (important for microreactors in experimental laboratories), how it can be manipulated to take a particular branch of the channel (useful for drop sorting), and the conditions (capillary number, ratio of drop diameter to channel height, etc.) that the drop fluid should have for a desired purpose. This study has a wide range of applications in biomedical and cosmetic industries, food and beverage processing, membrane emulsification, and enhanced oil recovery.

2.1.2. Prior work and context for current work

Due to its importance, the dynamics of drops in microchannels and other confined geometries has been extensively studied. For example, Zhou & Pozrikidis (1994) numerically studied the motion of periodic emulsions with viscous 2D drops between two parallel plane walls. Instead of using the standard boundary-integral method, they used a version of it: the method of interfacial dynamics, where they solved for the velocity at the interface of the drops and advanced its position using a standard time-marching method (more convenient for a pressure-driven flow). As in our case, they analyzed the effect of the capillary number, and they also included a study of the effect of the number of drops; however, analysis of a straight channel does not include drop interactions with a corner or a side channel. Chung, et al. (2010) studied the dynamics of a droplet passing obstructions in a confined microchannel. They analyzed several different types of obstructions to determine the effect of their shapes and placement on the drop motion. In their case, they simulated 2D deformable droplets using the finite-element, front-tracking method (Chung et al., 2008). They observed discrepancies between their simulations and experiments, likely due to using a 2D model. Nourbakhsh et al. (2011) used a finite-difference, front-tracking method to analyze the motion of deformable drops suspended in Poiseuille flows. Using the

Navier-Stokes equations at non-zero Reynolds number, they observed that drops with small capillary numbers migrate according to the Segre-Silberberg effect, which arises due to inertia. When the capillary number is increased, the drop behaves as it would in a creeping flow, where migration is due to deformation. Other authors, including Chen et al. (2014), studied the migration dynamics and equilibrium positions of drops in microchannels due to the Segre-Silberberg effect. In the Stokes approximation of the present work, however, the drop migrates to an equilibrium position due to its deformation and not because of inertia, as also observed by Nourbakhsh et al. (2011).

Of more direct relevance to the current work are microchannels that have branches or side channels. In particular, T-shaped microchannels are widely used in microfluidic emulsification and drop formation. Several authors have studied and modelled drop formation from one phase into another in a T-junction (Garstecki et al. 2006; Xu et al., 2006; Wang et al., 2011; Vladisavljević et al., 2012). Typically, the droplet phase is introduced through the stem of the T, while the continuous phase enters at higher flow rate through one of the arms and causes droplets to form by detaching from the droplet phase at the junction. Early work on droplet formation using microchannels of several geometries was reviewed by Christopher & Anna (2007). A more recent study by Nekouei & Vanapalli (2017) used a volume-of-fluid (VOF) method to investigate the influence of the viscosity ratio on droplet formation at a T-junction. They provide a nice overview of prior work, and their simulations show good agreement with experiments.

Additional researchers have performed experiments on single drops moving through a continuous fluid in the branches of a T-shaped microchannel. In many of the cases, the drop is initially placed in the middle branch (i.e., stem of the symmetric T-junction) and then must turn 90 degrees to the left or right to continue along one of the lateral branches (due to flow entering

one arm of the top of the T and exiting the other), or undergo symmetric breakup when the exit flow is divided equally between the two arms of the top of the T. Link et al. (2004) performed experiments to break larger drops in a pressure-driven flow into smaller, size-controlled drops. They determined the breakup conditions at a T-junction, with drops introduced through the stem and then split when reaching the junction due to outward flow in each arm. They also demonstrated a sequential breakup using the same configuration for making very small drops at high dispersed phase volume fractions.

Jullien et al. (2009) performed experimental studies of the breakup of drops with small capillary numbers in microfluidic T-junctions, again with larger drops introduced in the stem and then splitting into the two arms when reaching the junction. Using a broad range of capillary numbers, they observed two different breakup regimes: in the first one, a gap exists between the drop and the wall of the micro-device, and the breakup process reasonably agrees with the analytical 2D theory of Leshansky & Pismen (2009); in the second one, the droplet touches the wall and obstructs the T-junction before breaking.

Other authors have modelled the motion and potential breakup of a drop in a T-shaped microchannel. Hoang et al. (2013) used OpenFoam software (based on the volume-of-fluid method) to simulate motion and breakup of a large, strongly deformable 3D drop in a T-junction at very small but nonzero Reynolds numbers. Both steady- and stop-flow protocols were implemented, with particular emphasis on the dynamics of neck thinning near breakup. Chen & Deng (2017) developed a lattice-Boltzmann algorithm to analyze the dynamics of a 2D droplet going through a microfluidic T-junction. They determined under which conditions (drop size and capillary number, viscosity ratio between disperse and continuous phases, and geometry of the T-junction microchannel) the drop does not break, it breaks with permanent obstruction of the

channel, or it breaks with tunnels, where the drop does not obstruct the channel after breakup. They also studied the pressure fields inside the microchannel. Both of these studies considered the common geometry of a large drop entering the stem of the T-junction and then potentially breaking into two smaller drops (one in each side-arm) due to the stretching flow and capillary neck pinchoff.

As a complement to the aforementioned modeling studies, we consider a drop that starts in one of the lateral branches (i.e., the arm or top of the T) in a pressure-driven flow and then may either continue straight or turn 90 degrees into the stem. This case is less studied than a drop entering the stem of the T, but is of particular interest in the current work due to the asymmetry of the geometry and the strong interaction of the drop with a corner of the junction. This flow geometry drastically effects the drop behavior and creates new simulation challenges, requiring a robust algorithm and high numerical resolution to reliably predict the simulation outcome.

In related experimental work, Ménétrier-Deremble & Tabeling (2006) studied how drop breakup is directly related to the microchannel geometry by using devices with junctions of arbitrary angles between the main branch and a side branch. In their work, drops were formed at a T-junction and then moved to a λ junction with an angled side branch. Breakup depended on flow rates and geometry and was correlated with the length of a "finger" into the side channel. The drops were relatively large, so that they nearly filled the main branch; the side channel was relatively small, so that a "finger" of the drop extended into it. In contrast, the drops in the current study are generally smaller than the channel dimensions, and the side channel is the same size as the main channel. In another related study, Wang et al. (2018) used an immersed-boundary, lattice-Boltzmann method to study the motion of deformable capsules through a straight channel with an orthogonal branch. Capsule breaking was not included, but the effects of the geometry of the side

branch on the capsule path selection was examined. Several other researchers (e. g. Barber et al., 2008; Secomb et al., 2007; Woolfenden & Blyth, 2011; Trofa et al., 2016; Villone et al., 2017) also simulated the motion of deformable capsules and elastic particles and their partitioning or sorting upon encountering an asymmetric junction. The current work considers deformable droplets instead, and includes potential breakup into smaller droplets that enter separate channels.

To meet the need for a high-resolution algorithm to follow the motion of deformable drops in microchannels, we adapt the approach of Zinchenko et al. (2012). They developed a "moving-frame" (MF) method to study the behavior of a spherical solid particle in a plane-parallel microchannel of arbitrary complex shape (but restricted to plane walls). In their work, the particle was assumed to be comparable in size with the narrowest channel dimension, but much smaller than the overall channel domain. To handle such geometries efficiently, a two-dimensional (2D) problem was first solved for the carrier or base flow in the entire channel without the particle. Then, the three-dimensional (3D) boundary-integral (BI) problem was solved in the dynamically constructed moving frame around the particle to determine the particle motion and fate. In the present work, we extend the moving-frame concept to simulate the motion of 3D deformable drops through complex channels. As shown below, the moving-frame boundary-integral method (MFBIM) allows us to study the properties under which the drop will break or will go as a whole through one of the branches (capture of the drop in a stable fashion on the corner was not observed, except potentially for small capillary numbers or small drops having small deformations). We are also able to predict an accurate volume partition ratio between the daughter drops formed after breakup for different fluid properties and flow ratios between the branches of the channel, which is of interest in drop formation because one would be able to form drops of specific sizes with a

fairly simple device. It could be used in combination with and/or as substitution for other emulsion formation techniques (Gañán-Calvo, 1998; Umbanhowar et al., 2000; Sugiura et al., 2001).

Another motivation for the present study was to compare our dynamics of drop neck thinning with the local, self-similar solution of Lister & Stone (1998), which was developed for an isolated neck at ultimate breakup, to examine the influence of a nearby corner or wall. In addition to our main focus of drops introduced into the lateral branch, we performed limited simulations for a large drop entering the T-channel by the stem branch, so that neck thinning was not affected by the presence of the corner(s) of the channel and the drop breakup is primarily due to capillary stresses. As shown below, our convergence-tested results compare favorably with the local theory (Lister & Stone, 1998), while other simulations by OpenFoam/VOF (Hoang et al., 2013) for the neck-thinning rate near breakup could not demonstrate such close agreement. These comparisons lend more credibility to the present MFBIM approach at small Reynolds numbers, allowing for much higher resolutions and more accurate drop breakup dynamics. Moreover, the algorithm described in the present work is suitable for future studies of the dynamic behavior of a drop in a more complex channel with multiple bifurcations.

2.2. Theoretical development

Consider a 3D deformable drop of dynamic viscosity μ' moving with velocity field $\boldsymbol{u}'$ (inside the drop) through a plane-parallel microchannel containing a fluid of viscosity μ_e and velocity field $\boldsymbol{u}^e$ at Reynolds number small compared to unity. The velocity on the walls of the channel is zero due to the no-slip condition. The drop and the fluid in the channel have closely matching densities so that sedimentation is negligible compared to the flow-driven motion. A schematic representation of the problem is shown in Figure 2.1. The third dimension

of the channel (in the direction normal to the plane of drawing in Figure 2.1) is assumed to effectively be infinite.

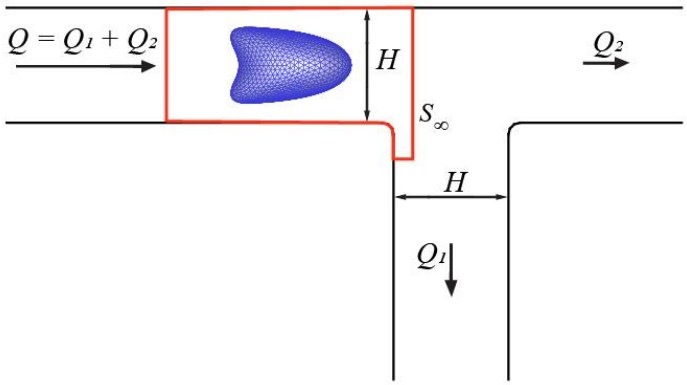

Figure 2.1. Schematic representation of the problem for a T-shaped microchannel.

Schematic representation of the problem for a T-shaped microchannel of height H, with input flow rate Q (per unit width in the third dimension) and two output flow rates: Q1 through the side branch and Q2 through the straight branch; S_∞ is the boundary of the computational box.

The goal is to solve for the drop deformation and motion in the microchannel and determine the conditions under which the drop will enter one of the branches without breaking and the conditions for which it will break and give rise to smaller droplets entering both branches. To do so, it is necessary to solve the Stokes equations, a linearization of the Navier-Stokes equations for a fluid at very small Reynolds numbers. The effects of the capillary number, $\mathrm{Ca} = \mu_e Q/(H\sigma)$, where σ is the interfacial tension, the viscosity ratio $\lambda = \mu'/\mu_e$ between the drop and the carrier fluid, and the relative radius $R = a/H$ of the drop in non-deformed state with respect to the channel height are studied to determine the range of critical flow ratios that govern when the drop passes through one or the other of the branches without breaking. To make the problem non-dimensional, we use the input channel height H as the length scale, the average input flow velocity $U = Q/H$ as the velocity scale, and H/U as the time scale.

We work in the low-Reynolds-number regime, $\mathrm{Re} = \rho UH/\mu_e \ll 1$, but we show that the analysis of the drop motion and deformation remains accurate to Re ~ 30 (see Section 2.5), with Ca = O(1), where ρ is the fluid density. Relevance of this problem formulation to microfluidic conditions is discussed in Section 2.5.

2.2.1. Moving frame or computational cell

Similar to the approach by Zinchenko et al. (2012) for a solid particle in a general-shape microchannel, a "moving-frame" (MF) computational cell with the surface S_∞ around the drop is used (Figure 1). The cell boundary S_∞ is obtained by intersecting a cubic box around the drop centroid with the channel walls. Zinchenko et al. (2012) also developed a general boundary-integral algorithm for the flow through a 2D microchannel without a particle or drop. These approaches are used in our problem, and it is assumed that the velocity $\boldsymbol{u}_\infty$ of the flow at the computational cell boundary S_∞ is not perturbed by the drop presence. Thus, the cell should be much larger than the drop so that the flow disturbance due to the drop is small on its boundaries, yet much smaller than the entire channel (or else there is no advantage in using a computational cell rather than the whole channel). In our case, the size of the moving frame is adjustable according to the drop deformation, so the length of the panels varies depending on the radius of the minimal circumscribed sphere around the drop centered at the drop centroid. As discussed in Section 2.3.1, most of the calculations used a moving frame with sides of length six times the radius of the smallest sphere that encloses the entire deformed drop.

2.2.2. Solution in the microchannel without the drop

To solve the problem, it is necessary to first calculate the velocity of the carrier fluid without the drop, $\boldsymbol{u}_\infty$, in the entire channel domain, as in Zinchenko et al. (2012). This fluid velocity is sought as a double-layer contribution from the channel boundaries:

$$\boldsymbol{u}_\infty(\boldsymbol{y}) = \sum_{i=1}^{M} 2 \int_{\mathcal{L}_i} \boldsymbol{q}_\infty(\boldsymbol{x}) \cdot \boldsymbol{\tau}^{2D}(\boldsymbol{r}) \cdot \boldsymbol{n}(\boldsymbol{x}) ds_x, \tag{2.1}$$

where $\boldsymbol{r} = \boldsymbol{x} - \boldsymbol{y}$, $\mathcal{L} = \mathcal{L}_1 \cup \mathcal{L}_2 \cup \ldots \mathcal{L}_M$ is the channel contour consisting of straight-line panels $\mathcal{L}_i$, ds is the length element, $\boldsymbol{\tau}^{2D}$ is the fundamental stresslet in two dimensions:

$$\boldsymbol{\tau}^{2D}(\boldsymbol{r}) = \frac{1}{\pi} \frac{\boldsymbol{rrr}}{r^4}, \quad r = |\boldsymbol{r}| , \tag{2.2}$$

$\boldsymbol{n}(\boldsymbol{x})$ is the outward unit normal to contour $\mathcal{L}$, and $\boldsymbol{q}_\infty(\boldsymbol{x})$ is a yet unknown potential density. The contour $\mathcal{L}$ includes inlet and outlet panels, where the velocity $\boldsymbol{u}_\infty$ is prescribed by Poiseuille flows. A fully deflated form of the BI equation for $\boldsymbol{q}_\infty$ is achieved by first representing the potential density $\boldsymbol{q}_\infty(\boldsymbol{x})$ as $\widetilde{\boldsymbol{q}}_\infty(\boldsymbol{x}) - \frac{1}{2}\widetilde{\boldsymbol{q}}'_\infty(\boldsymbol{x})$, where the prime denotes the rigid-body projection of $\widetilde{\boldsymbol{q}}_\infty(\boldsymbol{x})$:

$$\widetilde{\boldsymbol{q}}'_\infty(\boldsymbol{x}) = \boldsymbol{A} + \boldsymbol{B} \times (\boldsymbol{x} - \boldsymbol{x}_0) \tag{2.3}$$

(see Zinchenko et al. (2012) for details). Taking the limit $\boldsymbol{y} \to \mathcal{L}$ (from inside the contour $\mathcal{L}$) yields the desired BI equation for $\widetilde{\boldsymbol{q}}_\infty$:

$$\widetilde{\boldsymbol{q}}_\infty(\boldsymbol{y}) = \boldsymbol{u}^b(\boldsymbol{y}) - 2 \int_{\mathcal{L}} \widetilde{\boldsymbol{q}}_\infty(\boldsymbol{x}) \cdot \boldsymbol{\tau}^{2D}(\boldsymbol{r}) \cdot \boldsymbol{n}(\boldsymbol{x}) ds_x + \widetilde{\boldsymbol{q}}'_\infty(\boldsymbol{y}) - \frac{\boldsymbol{n}(\boldsymbol{y})}{L} \int_{\mathcal{L}} \widetilde{\boldsymbol{q}}_\infty(\boldsymbol{x}) \cdot \boldsymbol{n}(\boldsymbol{x}) ds_x , \tag{2.4}$$

where $\boldsymbol{u}^b$ is the prescribed velocity on $\mathcal{L}$ (i.e., zero on the channel walls, and Poiseuille flows on inlet and outlet panels); $\mathcal{L}$ is the total contour length. Due to sharp (or nearly sharp) corners in the 2D geometry, a special analytical desingularization (Zinchenko et al., 2012) is used for the double-layer contribution in equation (2.4). In principle, the fully-deflated equation (2.4) can be solved by successive substitutions, but this simplest approach can run into difficulties (again, due to sharp corners) with divergence (or very poor convergence) of iterations. Instead, more powerful biconjugate-gradient iterations were used as in (Zinchenko et al., 2012). Once the potential $\boldsymbol{q}_\infty(\boldsymbol{x})$

from the 2D solution is tabulated (prior to dynamical simulations with the drop), the form (2.1) (together with the proper regularization (Zinchenko et al., 2012) is used for fast calculation of $\boldsymbol{u}_\infty(\boldsymbol{y})$ inside the channel.

2.2.3. Boundary-integral formulation for a 3D drop in a channel

To solve the 3D problem for a deformable drop inside the moving frame S_∞, we use the fundamental solution due to a point force in a Stokes flow, the Stokeslet. Based on Green's theorem, the fluid velocity perturbation $\Delta\boldsymbol{u}^e(\boldsymbol{y}) = \boldsymbol{u}^e(\boldsymbol{y}) - \boldsymbol{u}_\infty(\boldsymbol{y})$ from the 2D solution $\boldsymbol{u}_\infty$ can be represented between the drop surface S_d and the MF surface S_∞ as

$$\Delta\boldsymbol{u}^e(\boldsymbol{y}) = \int_{S_\infty} \Delta\boldsymbol{u}^e(\boldsymbol{x}) \cdot \boldsymbol{\tau}(\boldsymbol{r}) \cdot \boldsymbol{n}(\boldsymbol{x}) dS_x - \frac{1}{\mu_e}\int_{S_\infty} \boldsymbol{G}(\boldsymbol{r}) \cdot \Delta\boldsymbol{f}^e(\boldsymbol{x}) dS_x + \frac{1}{\mu_e}\int_{S_d} \Delta\boldsymbol{f}^e(\boldsymbol{x}) \cdot \boldsymbol{G}(\boldsymbol{r}) dS_x \quad - \int_{S_d} \Delta\boldsymbol{u}^e(\boldsymbol{x}) \cdot \boldsymbol{\tau}(\boldsymbol{r}) \cdot \boldsymbol{n}(\boldsymbol{x}) dS_x, \tag{2.5}$$

where $\boldsymbol{r} = \boldsymbol{x} - \boldsymbol{y}$, $\boldsymbol{G}(\boldsymbol{r}) = -(8\pi)^{-1}(\boldsymbol{I}/r + \boldsymbol{rr}/r^3)$ is the free-space Green tensor, $\boldsymbol{\tau}(\boldsymbol{r}) = (3/4\pi)\boldsymbol{rrr}/r^5$ is the corresponding fundamental Stresslet, $\Delta\boldsymbol{f}^e = \boldsymbol{f}^e - \boldsymbol{f}_\infty$ is the stress vector perturbation, and index *e* marks quantities related to the carrier fluid. On the moving-frame boundary, $\boldsymbol{u}^e = \boldsymbol{u}_\infty$ and hence the first integral in (2.5) vanishes. Another observation is that $\Delta\boldsymbol{f}^e$ and $\Delta\boldsymbol{u}^e$ in the last two integrals of (2.5) can be simply replaced by $\boldsymbol{f}^e$ and $\boldsymbol{u}^e$, respectively. Indeed,

$$\frac{1}{\mu_e}\int_{S_d} \boldsymbol{f}_\infty(\boldsymbol{x}) \cdot \boldsymbol{G}(\boldsymbol{r}) dS_x - \int_{S_d} \boldsymbol{u}_\infty(\boldsymbol{x}) \cdot \boldsymbol{\tau}(\boldsymbol{r}) \cdot \boldsymbol{n}(\boldsymbol{x}) dS_x = 0 \tag{2.6}$$

due to the reciprocal theorem for flows $\boldsymbol{u}_\infty(\boldsymbol{x})$ and $\boldsymbol{G}(\boldsymbol{x} - \boldsymbol{y})$. Hence, for a point $\boldsymbol{y}$ between S_d and S_∞,

$$\boldsymbol{u^e}(\boldsymbol{y}) = \boldsymbol{u}_\infty(\boldsymbol{y}) - \frac{1}{\mu_e}\int_{S_\infty} \boldsymbol{G}(\boldsymbol{r}) \cdot \Delta \boldsymbol{f}^e(\boldsymbol{x}) dS_x + \frac{1}{\mu_e}\int_{S_d} \boldsymbol{f^e}(\boldsymbol{x}) \cdot \boldsymbol{G}(\boldsymbol{r}) dS_x - \int_{S_d} \boldsymbol{u^e}(\boldsymbol{x}) \cdot \boldsymbol{\tau}(\boldsymbol{r}) \cdot \boldsymbol{n}(\boldsymbol{x}) dS_x \quad . \tag{2.7}$$

Additionally, the reciprocal theorem applied to the inner flow $\boldsymbol{u}'(\boldsymbol{x})$ (inside the drop) and $\boldsymbol{G}(\boldsymbol{x}-\boldsymbol{y})$ gives for a point $\boldsymbol{y}$ between S_d and S_∞:

$$0 = \frac{1}{\mu'}\int_{S_d} \boldsymbol{f}'(\boldsymbol{x}) \cdot \boldsymbol{G}(\boldsymbol{r}) dS_x - \int_{S_d} \boldsymbol{u}'(\boldsymbol{x}) \cdot \boldsymbol{\tau}(\boldsymbol{r}) \cdot \boldsymbol{n}(\boldsymbol{x}) dS_x \,, \tag{2.8}$$

where the prime marks values for the interior fluid. Like in Rallison & Acrivos (1978), velocity continuity is used to combine (2.7) and (2.8), to arrive at:

$$\boldsymbol{u^e}(\boldsymbol{y}) = \boldsymbol{u}_\infty(\boldsymbol{y}) - \frac{1}{\mu_e}\int_{S_\infty} \boldsymbol{G}(\boldsymbol{r}) \cdot \Delta \boldsymbol{f}(\boldsymbol{x}) dS_x + \frac{1}{\mu_e}\int_{S_d} [\boldsymbol{f^e}(\boldsymbol{x}) - \boldsymbol{f}'(\boldsymbol{x})] \cdot \boldsymbol{G}(\boldsymbol{r}) dS_x + (\lambda - 1)\int_{S_d} \boldsymbol{u}(\boldsymbol{x}) \cdot \boldsymbol{\tau}(\boldsymbol{r}) \cdot \boldsymbol{n}(\boldsymbol{x}) dS_x \quad , \tag{2.9}$$

where $\boldsymbol{u} = \boldsymbol{u^e} = \boldsymbol{u}'$ is the common velocity on the interface S_d. Since the first integral on the right hand side of equation (2.9) has zero flux through S_∞, it can be represented inside S_∞ as a double-layer potential (Pozrikidis, 1992):

$$-\frac{1}{\mu_e}\int_{S_\infty} \boldsymbol{G}(\boldsymbol{r}) \cdot \Delta \boldsymbol{f}(\boldsymbol{x}) dS_x = 2\int \boldsymbol{q}(\boldsymbol{x}) \cdot \boldsymbol{\tau}(\boldsymbol{r}) \cdot \boldsymbol{n}(\boldsymbol{x}) dS_x, \tag{2.10}$$

with yet unknown potential density $\boldsymbol{q}(\boldsymbol{x})$. The choice of $\boldsymbol{q}(\boldsymbol{x})$ is not unique, since an arbitrary one-parameter eigensolution of the corresponding BI equation on S_∞ can be added without affecting the double-layer integral (2.10) for $\boldsymbol{y}$ inside S_∞. To remove this ambiguity, $\boldsymbol{q}(\boldsymbol{x})$ is constrained by the condition of zero-flux through S_∞. For a surfactant-free system, the stress vector jump on the interface is

$$\boldsymbol{f^e} - \boldsymbol{f'} = 2\sigma k(\boldsymbol{x})\boldsymbol{n}(\boldsymbol{x}), \tag{2.11}$$

where σ is the constant surface tension, and $k = (k_1 + k_2)/2$ is the local mean surface curvature at $\boldsymbol{x}$.

Taking the limit $\boldsymbol{y} \to S_d$ or S_∞ and using the jump properties of the double-layer potentials (Pozrikidis, 1992),we arrive at two BI equations for $\boldsymbol{u}(\boldsymbol{y})$ on S_d and $\boldsymbol{q}(\boldsymbol{y})$ on S_∞:

$$\boldsymbol{u}(\boldsymbol{y}) = \frac{2}{(\lambda+1)}\left[\boldsymbol{u}_\infty(\boldsymbol{y}) + \boldsymbol{F}(\boldsymbol{y}) + 2\int_{S_\infty} \boldsymbol{q}(\boldsymbol{x}) \cdot \boldsymbol{\tau}(\boldsymbol{r}) \cdot \boldsymbol{n}(\boldsymbol{x})\, dS_x\right] + \frac{2(\lambda-1)}{(\lambda+1)}\int_{S_d} \boldsymbol{u}(\boldsymbol{x}) \cdot \boldsymbol{\tau}(\boldsymbol{r}) \cdot \boldsymbol{n}(\boldsymbol{x})\, dS_x$$

for $\boldsymbol{y} \epsilon S_d$ (2.12)

and

$$\boldsymbol{q}(\boldsymbol{y}) = -\boldsymbol{F}(\boldsymbol{y}) - (\lambda - 1)\int_{S_d} \boldsymbol{u}(\boldsymbol{x}) \cdot \boldsymbol{\tau}(\boldsymbol{r}) \cdot \boldsymbol{n}(\boldsymbol{x})\, dS_x - 2\int_{S_\infty} \boldsymbol{q}(\boldsymbol{x}) \cdot \boldsymbol{\tau}(\boldsymbol{r}) \cdot \boldsymbol{n}(\boldsymbol{x})\, dS_x -$$

$$\frac{\boldsymbol{n}(\boldsymbol{y})}{S_\infty}\int_{S_\infty} \boldsymbol{q}(\boldsymbol{x}) \cdot \boldsymbol{n}(\boldsymbol{x})\, dS_x \quad \text{for } \boldsymbol{y} \epsilon S_\infty\ . \tag{2.13}$$

Here, the inhomogenous term is

$$\boldsymbol{F}(\boldsymbol{y}) = \frac{1}{\mu_e}\int_{S_d} \boldsymbol{G}(\boldsymbol{x} - \boldsymbol{y}) \cdot 2\sigma k(\boldsymbol{x})\boldsymbol{n}(\boldsymbol{x}) dS_x\ . \tag{2.14}$$

The role of the last term in (2.13) is to select the unique solution, with zero flux of $\boldsymbol{q}(\boldsymbol{x})$ through S_∞. As in (Zinchenko et al., 2012), the contribution of the top and bottom portions of the MF boundary are neglected, which is justified for a moving frame with depth in the third dimension much larger than the drop extent in that direction, as is the case in the present simulations.

2.2.4. Mesh generation and stabilization

To discretize the BI equations (2.12) - (2.14), the surface of the drop is divided into a triangular mesh. For the initial triangulation, the same methods as in Zinchenko et al. (1997) are used, which start with either a regular icosahedron or a regular dodecahedron inscribed into a sphere (the initial shape of the drop). In the first case, each face of the icosahedron is divided into four triangles, and the new vertices are projected onto the sphere. This process can be repeated as many times as required, with the final number of triangles being $20 \cdot 4^n$. In the second case, we first radially project the centers of the pentagons onto the sphere, connect the projection to the pentagon vertices to obtain triangles, and then we proceed as in the first case; the final number of triangles is then $60 \cdot 4^n$. For additional flexibility, these two schemes can be followed by subdividing each triangular face into m^2 equal triangles (with small m = 3 - 5) and projecting the new vertices radially onto the circumscribed sphere. These approaches produce almost uniform initial drop surface triangulations; each node (i.e. mesh triangle vertex) has six directly connected neighbors (except for just a few nodes with five neighbors).

As the drop moves and deforms, the quality of drop surface triangulation is maintained by the combination of three methods detailed in Zinchenko & Davis (2013): (1) 'passive mesh stabilization', (2) active mesh restructuring through minimization of potential 'mesh energy' and (3) node reconnection (edge swapping). Scheme (1) seeks to globally minimize, at each time step, the 'kinetic mesh energy' function as a quadratic function of the node velocities $\boldsymbol{V}_i = d\boldsymbol{x}_i/dt$ under the constraint $\boldsymbol{V_i} \cdot \boldsymbol{n}(\boldsymbol{x_i}) = \boldsymbol{u}(\boldsymbol{x_i}) \cdot \boldsymbol{n}(\boldsymbol{x_i})$ for each i, where the interfacial velocities $\boldsymbol{u}(\boldsymbol{x}_i)$ are provided by the BI solution. This scheme alone, with the carefully constructed, adaptive kinetic mesh energy function (Zinchenko & Davis, 2013) greatly slows down mesh degradation, so that the other two schemes need be used very infrequently. Scheme (2) uses a more complex form of

the potential mesh energy function, compared with the simplest, physically-motivated 'spring-like' form of (Cristini et al., 2001). The edge-swapping scheme (3) mostly follows their work; it is the only scheme of the three with topological mesh changes. Owing to powerful mesh control in schemes 1 and 2, more complex topological changes than edge swapping (Unverdi & Tryggvason, 1992) could be avoided altogether in the present simulations (as in Zinchenko & Davis (2013)).

Calculations of the normal vector $\boldsymbol{n}(\boldsymbol{x}_i)$ and principal curvatures k_1, k_2 in the drop mesh nodes $\boldsymbol{x}_i$ (required in the mesh operations and in the BI solution of eqs. (2.12) - (2.14)) were performed by the best-paraboloid-spline method (Zinchenko & Davis, 2000). This method generalizes the simplest best-paraboloid-scheme (Zinchenko et al., 1997) and usually gives much more accurate normal vectors $\boldsymbol{n}(\boldsymbol{x}_i)$.

To discretize the moving-frame surface, we use the non-adaptive version ($\alpha = 0$) of the algorithm from Zinchenko et al. (2012). Namely, the MF contour is first discretized, and this meshing is then extended to the third dimension of the moving frame. The neglect of contributions from the top and bottom portions of S_∞ greatly simplifies meshing, since these portions are generally of irregular shape. Also, it would be unwarranted to try using meshes adaptive to drop-wall surface clearance in our simulations; such adaptivity would greatly complicate the algorithm, but can hardly resolve difficulties inherent in close interaction of the drop and a sharp corner for attainable resolutions. Typically, a total of $\sim 10000-20000$ boundary elements on the drop and on the MF surface S_∞ was used in the simulations. The contributions of individual rectangular panels of S_∞ to the boundary integrals (2.12) and (2.13) were desingularized analytically, as described in Zinchenko et al. (2012), complemented by standard (near) singularity subtractions for drop-surface contributions. The resulting discretized system of equations for $\boldsymbol{q}(\boldsymbol{x})$ on S_∞ and $\boldsymbol{u}(\boldsymbol{x}_i)$ on S_d is solved iteratively by GMRES at each time step.

2.2.5. Corner smoothing

For a sharp corner of 90 degrees in the T-junction, lubrication is not strong enough to prevent drop-corner contact (neither for the simulation nor in a physical experiment), at which point the simulation would necessarily stop. To extend the time for which the drop is in the close proximity of the corner (but without physical contact), it was decided to slightly smooth the corners of the channel in the simulations. Namely, a circle of small radius h inscribed into the corner (Figure 2.2a) is divided into three equal parts, and the corner is smoothed (Figure 2.2b) by adding three corresponding straight-line segments, each of length $2h\sin 15^\circ$, to the channel geometry. For most of the calculations, a small value of $h = 0.1H$ was used, although a few other values were tested to determine the effect of the degree of smoothing (see Section 2.4.1). This smoothed geometry allows us to proceed further in the simulations until the drop reaches an impending breakup shape (with a thin neck), due to the obtuse vs. 90° angles comprising the corner as shown in Figure 2.2. Note that a perfectly smooth corner, with a continuous vs. discontinuous slope, would be required for lubrication to prevent any contact (Barnocky & Davis, 1989); however, the moving-frame algorithm is based on straight lines rather than curved segments.

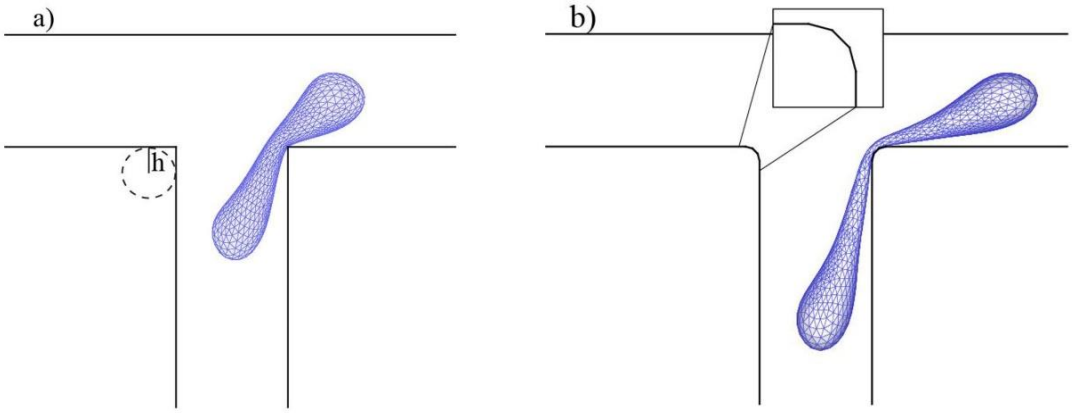

Figure 2.2. Drop in a T-shaped channel with sharp and smooth corners.

Last snapshot (before the code failed due to drop-corner impending contact) of a drop with relative radius R = 0.4, capillary number Ca = 0.8, viscosity ratio λ = 1.0, and number of triangles on its surface $N_{\triangle}$ = 2160 in a channel with a) a 90-degree sharp corner and b) a smooth corner divided into three segments of length 0.052H, representing the bases of three isosceles triangles for which the two equal sides are of length 0.1H. The drop is able to achieve a more elongated shape and approach an impending breakup when the corner of the channel is smooth.

2.3. Method validation

Since some of the findings for drop breakup by the present moving-frame boundary-integral method (MFBIM) algorithm are perhaps unexpected (Section 2.4.1), comprehensive algorithm validations by alternative methods are in order and described below.

2.3.1. Steady-shapes in a Poiseuille flow between two walls

The first test is for a drop freely suspended in a Poiseuille flow $\boldsymbol{u}_{\infty}$between two infinite, parallel plane walls, and approaching a steady-state shape and velocity. This Stokes problem was fist addressed by Griggs et al. (2007) based on the Liron & Mochon (1976) Green function $\boldsymbol{G}(\boldsymbol{x};\boldsymbol{y})$ for a two-wall geometry. However, in most of their simulations, Griggs et al. (2007) employed an approximation for $\boldsymbol{G}(\boldsymbol{x};\boldsymbol{y})$ which loses some accuracy for largest drop sizes. For more accurate

comparisons with MFBIM, an alternative Green function-based approach was used herein, following Staben et al. (2006), as described below.

Let $\boldsymbol{G^k}(\boldsymbol{x};\boldsymbol{y})$ be the flow velocity observed at $\boldsymbol{x}$ and generated by the Stokeslet $-(\boldsymbol{e}_k/r + r_k\,\boldsymbol{r}/r^3)/(8\pi)$ applied at $\boldsymbol{y}$, with $\boldsymbol{r} = \boldsymbol{x} - \boldsymbol{y}$ and no-slip $\boldsymbol{G^k}(\boldsymbol{x};\boldsymbol{y}) = \boldsymbol{0}$ on both walls. The MFBI system (13)-(14) is replaced by a single general equation (Pozrikidis, 1992; Rallison & Acrivos, 1978), with integrations over the drop surface only:

$$\boldsymbol{u}_k(\boldsymbol{y}) = \frac{2}{\lambda+1}\left[(\boldsymbol{u}_\infty)_{\boldsymbol{k}}(\boldsymbol{y}) + \frac{1}{\mu_e}\int_{S_d} 2\sigma k(x)\boldsymbol{G}^k(\boldsymbol{x};\boldsymbol{y})\cdot\boldsymbol{n}(\boldsymbol{x})dS_x\right] + \frac{2(\lambda-1)}{(\lambda+1)}\int_{S_d}\boldsymbol{u}(\boldsymbol{x})\cdot\boldsymbol{\tau}^k(\boldsymbol{x};\boldsymbol{y})\cdot \boldsymbol{n}(\boldsymbol{x})dS_x. \tag{2.15}$$

Here, $\boldsymbol{\tau}^k$ is the fundamental stresslet for $\boldsymbol{G^k}$; our Green function normalization has the sign opposite to Liron & Mochon (1976). As another advantage of (2.15), this formulation is for the infinite channel and, unlike the MFBIM method, it does not have a domain-size effect. An obvious drawback, though, is an extreme complexity of the Green function $\boldsymbol{G^k}$ and related stresslet. We follow an efficient approach from Staben et al. (2006) to represent $\boldsymbol{G}(\boldsymbol{x};\boldsymbol{y})$ as the free space plus analytical Blake's lower wall and upper wall corrections (Blake, 1971), plus the so-called two-wall interaction term. This last, cumbersome term involves a number of infinite Fourier-Bessel integrals, which are made fast convergent and smooth functions due to subtractions (Staben et al., 2006). With coordinates x_1 and x_2 along, and x_3 normal to the walls, these integrals and their derivatives are pretabulated as functions of x_3, y_3 and $(x_1 - y_1)^2 + (x_2 - y_2)^2$, which allows for feasible calculation of the kernels in (2.15) at each time step.

To compare our moving-frame boundary-integral results with the two-wall, Green function-based code (2WBIM, in what follows), we computed the value of the steady-state drop velocity, defined as the average of $\boldsymbol{u}$ over the drop volume:

$$\boldsymbol{U} = \frac{1}{V}\int_V \boldsymbol{u}(\boldsymbol{x})dV = \frac{1}{V}\int_S [\boldsymbol{u}(\boldsymbol{x}) \cdot \boldsymbol{n}(\boldsymbol{x})](\boldsymbol{x} - \boldsymbol{x_c})dS_x \,, \tag{2.16}$$

where $\boldsymbol{x_c}$ is the drop centroid. First, we studied the effect of the size of the moving frame around the drop in our boundary-integral calculations. The cubic box forming the moving frame has sides of length $2A^*R_d$, where A is a sizing factor and R_d is the radius of the circumscribed sphere containing the deformed drop at each time step. We then extrapolated the results for different sizes (A = 3.0, 4.5 and 5.0 for drops with R = 0.3 and A = 3.0, 4.5 and 6.0 for R > 0.3) (although such extrapolation carries some uncertainty) to obtain the average drop velocity component parallel to the channel walls in the limit $A \to \infty$. The resulting value was compared with that provided by the 2WBIM code.

The results are shown in Appendix A, where the steady-state drop velocity is scaled with the Poiseuille flow velocity U_c at the center of the channel in the absence of the drop. For equal viscosities, the extrapolated MF results and the 2WBIM results agree to three significant figures, with an average difference of only 0.04%. Moreover, the smallest MF frame (A = 3) yields steady-state drop velocities that differ by only 0.3% (on average) from the 2WBIM results, and so A = 3 was used in the rest of the calculations in this paper (unless noted otherwise). For $\lambda = 4$, the agreement is less close (1.6% difference for A = 3 and 0.3 % for the extrapolated MF result), but still quite acceptable. In this case, the flow perturbation caused by the drop is obviously larger than for $\lambda = 1$ (as expected from general principles), thus amplifying the effect of A on the MFBIM results.

Figure 2.3 shows excellent agreement of the two methods for the shapes calculation of a large drop as it moves through a straight channel. As studied by Griggs et al. (2007), for a subcritical Ca, a deformable, freely suspended drop in a Poiseuille flow between two infinitely long parallel plates eventually acquires a steady, bullet-like shape in the middle of the channel,

even if it starts off the center-plane. To reduce the number of parameters in our study, and avoid the need for long inlets, this shape (simulated separately for each different drop properties) was placed on the centerline of the input branch, as the initial condition for our drop simulations in the T-junction.

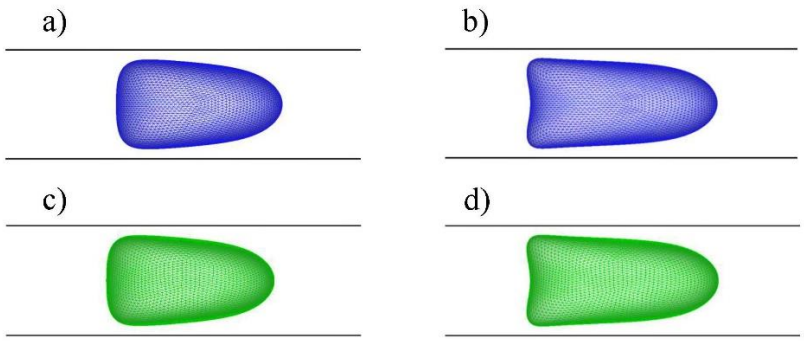

Figure 2.3. Shapes of a deformable drop at different non-dimensional times.

Deformable drop with capillary number Ca = 0.33, non-deformed radius relative to the channel height R = 0.635, viscosity ratio λ = 1.0, and $N_{\triangle}$ = 8640 triangles on its surface. Upper images: the shapes obtained by the MFBIM algorithm with A = 6 at non-dimensional times a) t = 5.0 and b) t = 12.0. Lower images: shapes obtained by the 2WBIM code at c) t = 5.0 and d) t = 12.0. In both simulations, the initial shape was an oblate spheroid with non-dimensional half-axes 0.8 and 0.4 centered in the channel. Good agreement is found between the drop shapes obtained with the two methods at different non-dimensional times.

2.3.2. Drop deformation due to Poiseuille flow through an opening in the bottom wall

In this test, an infinite straight channel of width H has an opening of length H at $|x_2| < H/2$ in the bottom wall $x_3 = 0$, with prescribed Poiseuille flow velocity:

$$\boldsymbol{u} = \frac{3}{2} Q[1 - (2x_2/H)^2]\boldsymbol{e}_3 \,, \tag{2.17}$$

entering the channel at the opening, and linear flux Q; $\boldsymbol{u} = \boldsymbol{0}$ on the other parts of the channel walls. The 3D drop is initially placed as an oblate spheroid against the opening, and it is of interest

to trace the drop shape evolution. The problem is made non-dimensional using *H* and *Q/H* as length and velocity scales, with $\mathrm{Ca} = \mu_e Q/(H\sigma)$. One could argue on physical grounds if (2.17) is a realistic boundary condition. Regardless, it provides a valuable and convincing test on the validity of our MFBIM algorithm (both 2D and 3D parts of it). First, the MFBIM set-up is different from that in the preceding subsection, namely, the opening must be implemented as a separate panel. Second, an alternative solution method is semi-analytical, as described below, to serve as a reliable benchmark.

The Green function approach and (2.15) are still applicable in this case, if $\boldsymbol{u}_\infty(\boldsymbol{y})$ is understood as the flow that would exist in the channel in the absence of the drop; indeed, it is only important for derivation of (2.15) that $\boldsymbol{u}_\infty(\boldsymbol{y})$ is the Stokes flow with zero $\boldsymbol{u}(\boldsymbol{y}) - \boldsymbol{u}_\infty(\boldsymbol{y})$ on the walls. The 2D flow $\boldsymbol{u}_\infty(\boldsymbol{y})$ is conveniently described by the bi-harmonic stream function ψ_∞. Using non-dimensional variables and simplified notations $y = x_2$, $z = x_3$, a general solution is sought as

$$\psi_\infty(y,z) = \int_0^\infty \frac{f(z,\Lambda)}{\Lambda}\sin(\Lambda y)\, d\Lambda\,, \tag{2.18}$$

where

$$f = A(\Lambda)e^{\Lambda(z-1)} + B(\Lambda)(z-1)e^{\Lambda(z-1)} + C(\Lambda)e^{-\Lambda z} + D(\Lambda)ze^{-\Lambda z}, \tag{2.19}$$

with the coefficients *A*, *B*, etc. found from the boundary conditions. The velocity components $\boldsymbol{u}_\infty(\boldsymbol{y})_z = \partial\psi_\infty/\partial y$, $\boldsymbol{u}_\infty(\boldsymbol{y})_y = -\partial\psi_\infty/\partial z$. Integrating (2.17) times $\cos(\Lambda y)$ over the opening $-1/2 < y < 1/2$ and using the inverse Fourier transform conveniently represents the lower wall boundary condition in the integral form, giving the equations for the coefficients at every Λ. The integral (2.18) is slowly convergent near the bottom wall (which may present difficulties for a drop

of large size). This difficulty is easily overcome by subtracting the lower- wall contribution from (2.19) and integrating the added-back terms analytically. The details on ψ_∞ are given in Appendix B. Figure 2.4 shows near-perfect agreement in a comparison between the results obtained with the two methods.

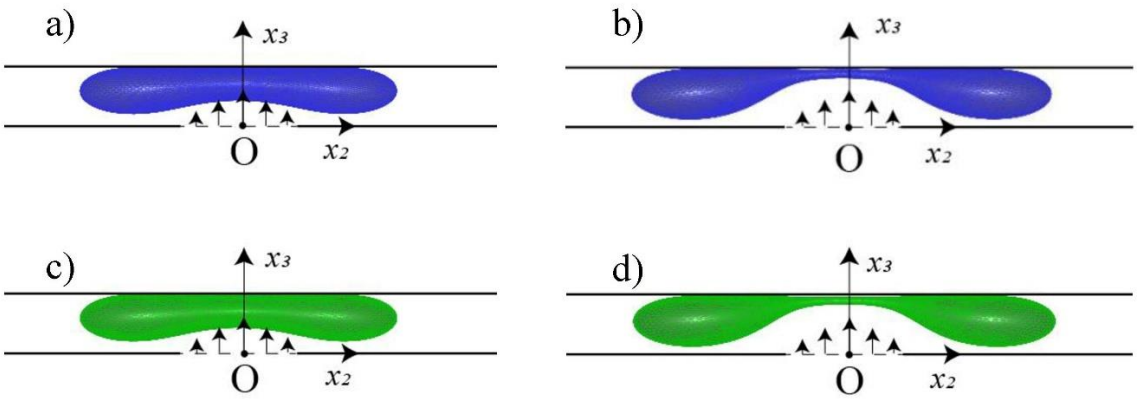

Figure 2.4. Shapes of a deformable drop in a channel with an opening at the bottom wall.

Deformable drop with capillary number Ca = 0.08, non-deformed radius relative to the channel height R = 0.635, viscosity ratio λ = 4.0, and $N_\triangle$ = 8640 triangles on its surface initially released in a channel with an opening at the bottom wall. Upper images: the MFBIM algorithm at non-dimensional times a) t = 4.5 and b) t = 7.5. Lower images: the 2WBIM code at c) t = 4.5 and d) t = 7.5. In both simulations, the initial shape was an oblate spheroid with half-axes 0.45 and 0.7543 centered at (0, 0, 0.5). Good agreement is found between the drop shapes obtained with the two methods at different non-dimensional times.

2.4. Results and discussion

2.4.1. Potential outcomes and volume partition

A simulation has three potential outcomes, as shown in Figure 2.5. First, when the flow ratio Q_1/Q_2 is small, the drop exits through the straight branch, in which the flow is strongest. Second, at intermediate flow ratios, the drop encounters the corner on the far side of the branch, where it stretches and approaches breakup into two smaller drops. Third, if the flow ratio Q_1/Q_2

is large, the drop exits through the stem branch, for which the flow is then strongest. Additionally, for sufficiently small drops or capillary numbers with equipartitioning of the flow, it was not possible to determine if the drop became stuck on the corner or would ultimately have one of the three aforementioned outcomes, as the deformation was small and the code would crash due to drop overlap with the corner before the outcome was clear.

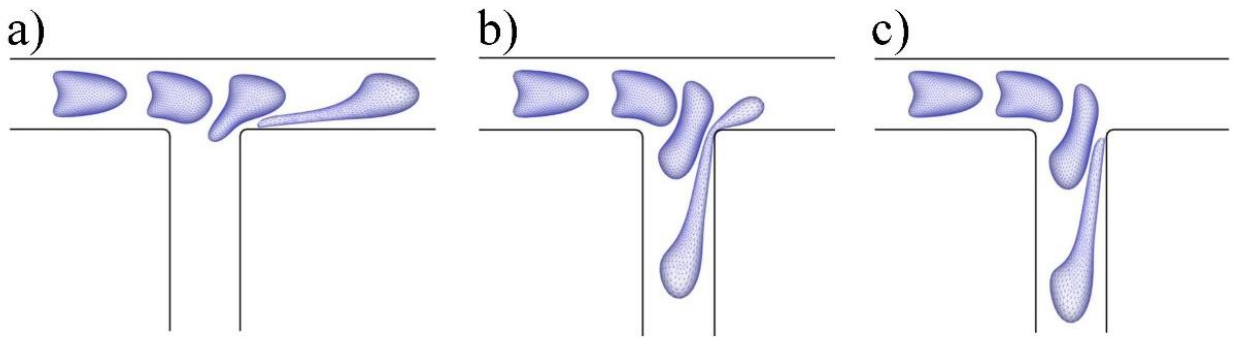

Figure 2.5. Potential outcomes for a drop in a T-shaped microchannel.

Drop with relative radius R = 0.4, capillary number Ca = 0.8, viscosity ratio λ = 1.0, number of surface triangles $N_{\triangle}$ = 2160, and flow ratios a) Q_1/Q_2 = 0.25 exiting through the straight (arm) branch of the microchannel, b) Q_1/Q_2 = 2.0 hitting the corner of the microchannel and approaching an impending breakup, and c) Q_1/Q_2 = 4.0 exiting through the side (stem) branch of the microchannel.

One objective of the simulations was to develop phase diagrams or outcome maps of the conditions leading to each of the three observed outcomes. For drops approaching an impending breakup, as shown in Figure 5b, a second objective was to determine the size of the daughter drop going through each branch or, equivalently, the volume partitioning between the two branches. The current simulations were carried out with sufficient resolution to demonstrate that breakup was imminent and to determine the volume of each daughter drop. However, the continued tracking of the two daughter drops after breakup, such as might be possible by adapting the method of

Zinchenko & Davis (2000), is beyond the scope of the current work (as the daughter drops would move far apart, invalidating the current use of a single moving frame). Below, we show an example of close approach to the corner and neck pinchoff.

To determine the volume partitioning, a cutting plane dividing the drop into two fragments just prior to breakup was constructed. For a chosen plane location and orientation, a relatively easy way to generate the neck contour is to find all intersection points of the plane with flat mesh triangle edges of the drop, and then reorder all such points in the cutting plane to form a closed contour. The location and orientation of the plane may then be chosen to minimize the polygon area S_{neck} inside the contour. To this end, it was sufficient to probe 10 - 15 different locations on the smoothing arc (Figure 2.2b, but on the corner adjacent to the drop) as the plane-corner intersection, and 10 - 15 different plane inclinations (in the range of $40^\circ - 50^\circ$ from the main-channel walls), choosing the thinnest portion of the neck, which occurred for a plane approximately bisecting the corner and oriented at $\approx 45^\circ$. Then, the volume of the drop within the region between the cutting plane and the side branch corresponds to V_1 that between the cutting plane and the straight branch corresponds to V_2. These volumes are calculated using the divergence theorem as the corresponding surface integrals over the two portions of the drop, e.g. $V_1 = 1/3 \int_{S_1} \boldsymbol{x} \cdot \boldsymbol{n}\, dS$, where $\boldsymbol{n}$ is the outward unit normal, and $\boldsymbol{x}$ is the radius-vector from an arbitrary point (chosen near the neck in the cutting plane to eliminate the neck contribution and minimize the numeral error of volume calculation). Figure 2.6 shows how the radius of the neck becomes thinner with time, with Figure 2.6c showing the cutting plane. As mentioned before, simulations after breakup are not intended in this work:, however, Figure 6d was generated using the fragmentation algorithm of Zinchenko & Davis (2013), based on the image of the drop at $t = 6.40$ before the simulations stopped,

to demonstrate that simulations could continue after the drop splits into two. A closeup of the cut neck is shown in Figure 2.6h.

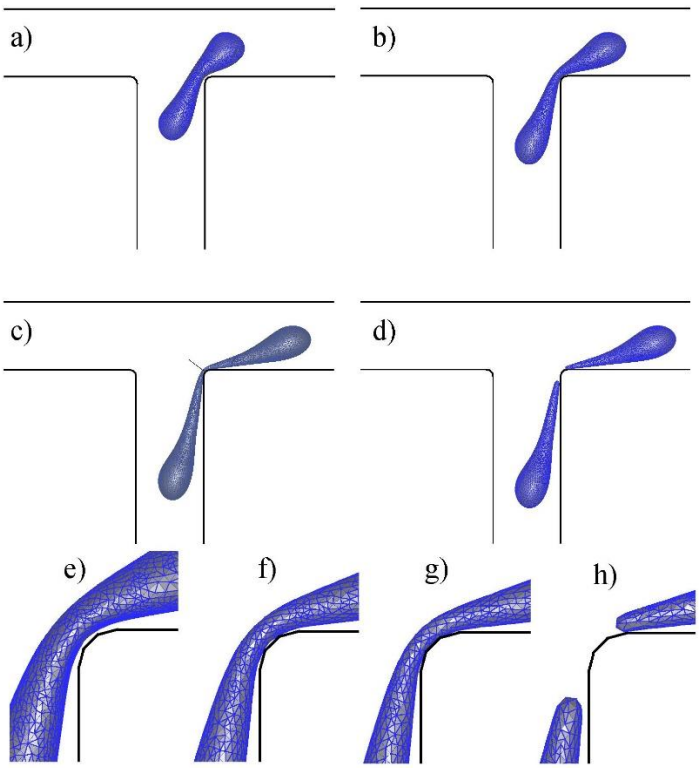

Figure 2.6. Neck shape evolution during drop breakup.

Drop with relative radius R = 0.4, capillary number Ca = 0.8, viscosity ratio λ = 1.0, number of triangles on its surface $N_{\triangle}$ = 8640, and flow ratio Q_1/Q_2 = 1.0 approaching breakup at non-dimensional times a) t = 4.60, b) t = 5.20, c) t = 6.09 and d) t = 6.40. In panel c), the cutting plane through the thinnest portion of the neck is shown as a dashed line, with the cutting plane perpendicular to the paper. Closeups of the neck region are shown at e) t = 5.50, f) t = 6.00, g) t = 6.30, and t = 6.40.

To demonstrate that drop breakup is indeed imminent, the dimensionless equivalent neck radius $r_{eq} = (S_{neck}/\pi)^{1/2}$ was plotted vs non-dimensional time. Figure 2.7 presents $r_{eq}(t)$ for the simulation from Figure 6, with $N_{\triangle}$ = 8640 drop mesh triangles and the whole moving-frame resolution (including the rightmost corner region) Δs_{mf} = 0.045 between neighboring mesh nodes

on the frame contour (see Figure 2.1) and along the third dimension (channel depth). For comparison, the dashed line in Figure 2.7 is for a similar simulation, when the drop resolution was increased to $N_{\triangle}$ = 11520 triangles, and the moving-frame resolution refined to Δs_{mf} = 0.0225. As follows from this convergence analysis, our neck-thinning dynamics can be quantitatively trusted to $t \approx 6.2-6.4$, and the tendency of $r_{eq}(t)$ to approach very small values is clearly seen. Figure 2.7 also shows the evolution of the neck shape in the simulation with $N_{\triangle}$ = 11520. The perspective in this figure is within the cutting plane that is at 45° to horizontal and looking down on this plane from the above right, so that the beveled corner is on the left. The neck shape is initially flattened or even dimpled due to lubrication forces and the proximity of the corner, but then becomes more circular due to capillary forces as breakup is approached. The neck also becomes thinner and moves closer to the corner as time proceeds. The round shape of the drop in our simulation near breakup warrants the comparison of our neck-thinning dynamics with the local self-similar, axisymmetrical solution of Lister & Stone (1998) for drop pinch-off in an unbounded flow. For λ = 1, they predicted the ultimate non-dimensional slope dr_{eq}/dt at breakup to be 0.034/Ca, or 0.0425 for the current example. Their result is expected to be universally applicable in general geometries, provided that the neck area (not necessarily the entire drop) remains away from flow boundaries (created e.g. by solid walls or other drops, etc.) at ultimate breakup. Indeed, for a 3D problem of drop breakup induced by the presence of another drop in gravity-driven motion (Zinchenko et al., 1999), very good agreement was observed for $\left|dr_{eq}/dt\right|$ with the result of Lister & Stone (1998). In the present case, it is not obvious a priori how closely our neck thinning dynamics would obey the unbounded axisymmetric solution, because the neck area remains near the corner at breakup. Nevertheless, our $\left|dr_{eq}/dt\right|$ values are fairly close to theoretical 0.0425 for the most part of the final neck thinning (e.g., the slope of $r_{eq}(t)$ is between 0.048 and 0.037 for t between 5.9 and 6.1 in

the $N_{\triangle}$ = 11520 simulation). Neck thinning continues to decelerate at larger times (e.g. $\left|dr_{eq}/dt\right|$ = 0.034 at t = 6.2). A likely explanation is that the drop neck becomes more curved when wrapping around the corner, and a larger portion of the neck meets lubrication resistance from the solid walls, causing more deviation from the unbounded theoretical solution of Lister & Stone (1998).

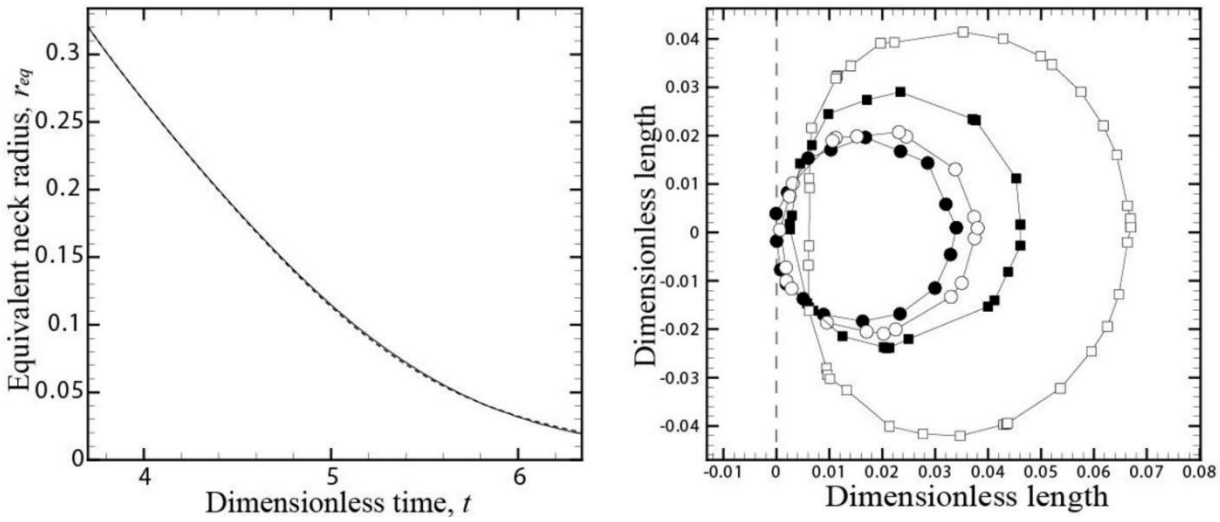

Figure 2.7. Drop neck thickness evolution.

The left panel shows the dimensionless equivalent neck radius vs. dimensionless time for a drop of relative radius R = 0.4, capillary number Ca = 0.8, viscosity ratio λ = 1.0, and number of triangles on its surface $N_{\triangle}$ = 8640 (solid line) and $N_{\triangle}$ = 11520 (dashed line) for a flow ratio Q_1/Q_2 = 1.0. The moving-frame resolution or discretization length (including the corner region) is Δs_{mf} = 0.045 for $N_{\triangle}$ = 8640, and 0.0225 for $N_{\triangle}$ = 11520. The right panel shows neck contours for $N_{\triangle}$ = 11520 at dimensionless times t = 5.91(□), 6.22(■), 6.38(○) and 6.46(●). The cutting plane is the plane of drawing, with the vertical dashed line representing the panels of the channel corner. The symbols in each contour are the intersection points of the plane with flat mesh triangle edges of the drop.

For a different setup, where a large drop is pushed by the flow into a symmetric T-junction through the side (stem) branch, 3D drop breakup simulations were performed at various viscosity ratios by Hoang et al. (2013) using OpenFoam/VOF software package, and the neck-thinning behavior they observed is quite different from the one observed here. In such simulations, the drop

neck also tends to become circular at breakup (with the pumping flow described by Nemer (2004) and Nemer et al. (2004) providing the mechanism to separate the neck from the wall), so the self-similar solution of Lister & Stone (1998) is still relevant. However, from Figure 6b of Hoang et al. (2013) at Ca = 6.25×10^{-3} and $\lambda = 1$, their ultimate non-dimensional slope *dr/dt* at breakup is 1.62, below the theoretical value of 5.44 from Lister & Stone (1998). Although their neck thinning does accelerate by the end of the simulation (because of the neck separation from the wall reducing the neck-wall hydrodynamic resistance), the 3.3-fold deviation from the theoretical slope is difficult to explain.

To explore what our MF BI solution code (fully verified in Section 2.3) would give for such a set-up at $\lambda = 1$, we performed simulations with the drop initial position in the stem of the T-channel (Figure 2.8). The external fluid flow was equally divided through both outlets, so the drop would break due to an extensional flow from the stem to the arms instead of due to the interaction with the corners of the channel. For comparison, simulations with 8640 and 11520 triangles on the drop surface were performed. The solid lines in the right panel of Figure 2.8 represent the equivalent drop neck radius at the middle of the geometry, while the dashed lines are for the neck radius of the narrowest cross-sections. The dynamics of $r_{eq}(t)$ in the middle is slightly affected by resolution (with no appreciable effect at smaller times $t < 4.5$), but the final value at breakup is insensitive to it. Lister & Stone's (1998) ultimate slope for the dashed lines at Ca = 0.15 would be 0.227; this prediction is expected to be relevant, since the narrowest neck is very small, round and well-separated from the walls at the end of our simulation in Figure 2.8. For $N_{\triangle}$ = 8640, the last good point on the dashed curve is at $t = 8.50$, with the slope $\left|dr_{eq}/dt\right| \approx 0.226$; for $N_{\triangle} = 11520$, it is $t = 8.55$, with slope of ≈ 0.213. Slight further increase in the slope could still be expected near pinch-off, judging by the curves in Figure 8. Regardless, this analysis confirms close

agreement of our breakup simulation with theory, as another validation of the present solution method and accuracy.

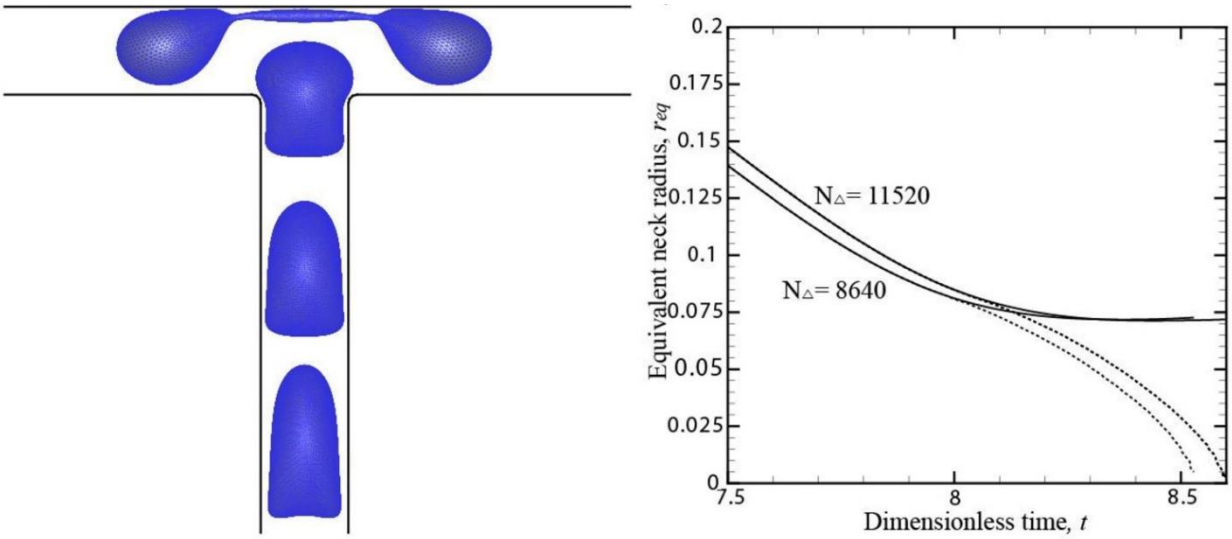

Figure 2.8. Visual and numerical neck analysis before and during drop breakup.

The left panel shows a drop with relative radius R = 0.635, capillary number Ca = 0.15, viscosity ratio λ = 1.0, number of surface triangles N_Δ = 11520, and A = 4.5 entering the T-channel through the stem branch and approaching an impending breakup due to an extensional flow created by the fluid exiting the channel through the upper branches. The right panel shows the dimensionless equivalent neck radius vs. dimensionless time for N_Δ = 11520. The solid lines represent the neck radius at the axis of symmetry of the drop and the dashed lines represent the value of the smallest equivalent neck radius present on the drop.

We further studied the effect of the number of mesh triangles $N_\triangle$ used to discretize the drop surface, on the volume partitioning for several flow ratios. The results are detailed in Appendix C and show excellent agreement between the partition volumes for the smallest and largest resolutions over a wide range of flow ratios. Thus, for the rest of the simulations, the results are shown for $N_\triangle$ = 2160, unless otherwise stated.

Smoothing the corners makes it easier for the drop to go through the branches without hitting a corner and becoming stuck or breaking. To determine the effect of corner smoothing,

different values of h (radius of a small circle inscribed into the corner of the channel, see Section 2.5) were studied. As detailed in Appendix C, drop breakup and partitioning are not sensitive to the degree of smoothing, except near the critical flow ratios, which determine whether the drop breaks or moves intact into one of the branches. When the corner smoothing panels are larger, the range between the critical flow ratios becomes smaller, because the blunt corners provide more lubrication to prevent the wall-drop contact. The smoothing sized used in the rest of the calculations is $h = 0.1H$.

2.4.2. Effect of the relative radius

Six different values for the drop relative radius were studied: R = a/H = 0.4, 0.3, 0.2, 0.15, 0.1 and 0.07. Figure 2.9 shows steady shapes for a long, straight channel for three of these simulations. As expected, the deformation is less for smaller drop sizes.

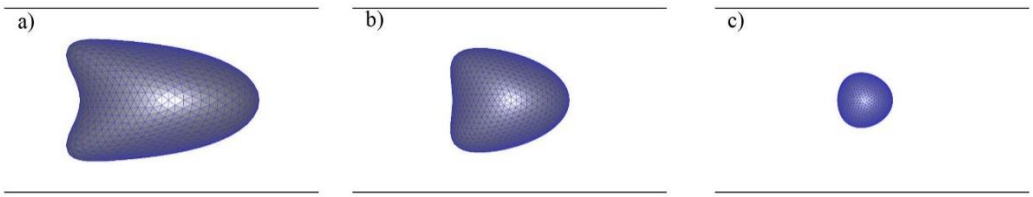

Figure 2.9. Steady-state shapes for drops with different relative radii.

Steady shape of drops released in a long microchannel with Ca = 0.8, λ = 1.0, $N_{\triangle}$ = 2160, and a) R = 0.4, b) R = 0.3 and c) R = 0.15.

The left panel of Figure 2.10 shows the outcome map or "phase diagram" for the six drop sizes. For large values of Q_1/Q_2, the drop moves into the side channel along with the flow Q_1. For small values of Q_1/Q_2, the drop continues along the straight channel with the flow Q2. For intermediate values of the flow ratio, the drop wraps around the far corner and then stretches and eventually breaks. These three outcomes are the same as those illustrated in Figure 2.4. The range

of flow ratios for impending breakup is reduced for a smaller drop, as it can move more easily through the side or straight channel and does not deform as easily as a larger drop. The simulations predict that a drop smaller than about $R = 0.1$ would not break for any flow ratio. The right panel of Figure 2.10 shows the volume partitioning of the drop for three of the drop sizes. Here, V_1/V is the fraction of the total drop volume that partitions to the side channel with flow Q_1. The slope of V_1/V versus Q_1/Q_2 is steeper when the drop is smaller, because the smaller drop breaks only over a narrow range of flow ratios.

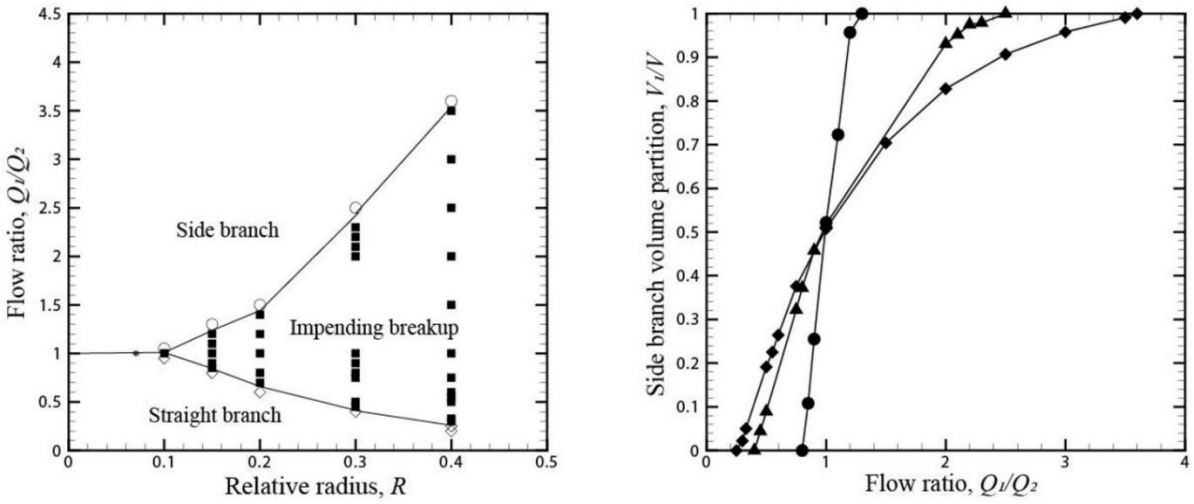

Figure 2.10. Outcome map and volume partition of drops with different relative radii.

Outcome map (left panel) showing the impending-breakup zone (■), the non-breakup zones (side branch (○) and straight branch (◊)), and where the simulation crashed (due to the drop hitting a sharp corner) before it was possible to determine if the drop was heading toward one of the branches or getting stuck (*), for drops with capillary number Ca = 0.8, viscosity ratio λ = 1.0, number of triangles on the surface $N_\triangle$ = 2160, and relative radii R = 0.07, 0.1, 0.15, 0.2, 0.3 and 0.4. The right panel shows the volume partition vs. flow ratio for relative radii R = 0.15 (●), 0.3 (▲) and 0.4 (◆).

2.4.3. Effect of the capillary number

Simulations were performed for different capillary numbers of a drop with a relative radius $R = 0.4$, viscosity ratio $\lambda = 1.0$, and number of triangles on the surface $N_{\triangle} = 2160$. The initial shapes of the drops released in the channel are presented in Figure 2.11 for three capillary numbers; these shapes are the steady-state shapes achieved by the drops in a long, straight channel. As expected, the deformation increases with increasing capillary number.

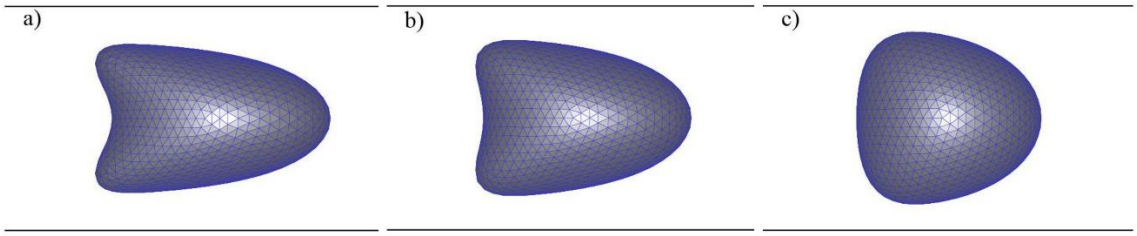

Figure 2.11. Steady-state shapes for drops with different capillary numbers.

Initial steady state shapes of drops released in the T-shaped microchannel with relative radius R = 0.4, viscosity ratio λ = 1.0, number of triangles $N_{\triangle}$ = 2160, and capillary numbers a) Ca = 0.8, b) Ca = 0.6 and c) Ca = 0.2.

Simulations for a drop with larger capillary numbers were also performed, but the surface tension was not strong enough to keep the drop from experiences large deformation and impending breakup, even long before reaching the junction. Typically, the upper and lower tails of the deformed drop (see Figure 2.11a) become elongated and then pinch off. For drops with relative radius $R = 0.4$, the critical capillary number above which a steady-state shape is not reached is $Ca_c = 0.85$, for drops of $R = 0.3$ the value is $Ca_c = 1.6$, and drops of $R = 0.15$ suffer mesh degradation over values above $Ca_c = 6.0$. Note that our definition of Ca does not include the drop size.

The left panel of Figure 2.12 shows the different outcomes for a drop with different capillary numbers. For smaller Ca, the drop does not deform as much and because of that it does not wrap around the corner and break, so the range of critical flow ratios in which breakage is

predicted is narrower. Indeed, it appears that no breakup is observed for Ca less than about 0.19. The right panel of Figure 2.12 shows the corresponding volume partition of the drop as a function of flow ratio for Ca = 0.4, 0.6 and 0.8. The partitioning is similar in the three cases, with nearly equal partitioning for $Q_1/Q_2 = 1.0$, but the range over which partitioning occurs is greater for larger Ca.

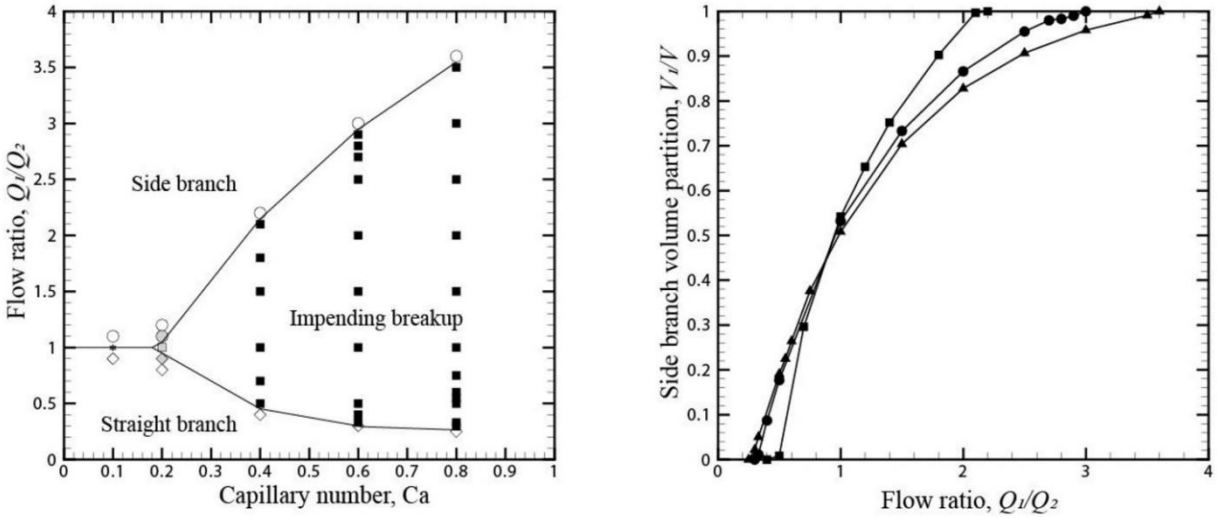

Figure 2.12. Outcome map and volume partition of drops with different capillary numbers.

Flow ratios (left panel) in the impending-breakup zone (■), in the non-breakup zones (side branch (○) and straight branch (◊)), and where the simulations crashed before it was possible to determine if it was heading toward one of the branches or getting stuck (*), for drops with relative radius R = 0.4, viscosity ratio λ = 1.0, number of triangles on the surface $N_\triangle$ = 2160, and capillary numbers Ca = 0.1, 0.2, 0.4, 0.6 and 0.8. The grey shaded symbols are for simulations that appeared to be headed for the outcomes indicated by the respective symbol shapes, but which crashed before the final outcome was certain. The right panel shows the volume partition vs. flow ratio for capillary numbers Ca = 0.4 (■), 0.6 (●) and 0.8 (▲).

For Ca ≤ 0.2, where the final outcome was not clear for flow ratios very close to unity, we introduced a node-correction procedure to preclude the contact between the drop and the walls of the channel and thereby extend the simulation time. To do so, the dimensionless distance between

the drop and the channel walls in the direction of the outward normal to each node on the drop surface is calculated and, if its value is smaller than the threshold δ (typically 0.0005), we move that node in the opposite direction just enough to keep the node-to-wall distance along the normal at δ. So, with this node correction, for Ca $\leq$ 0.2, the drop is able to go through the branches of the channel when $Q_1/Q_2 = 1$ without breaking. For Ca = 0.2 and $Q_1/Q_2 = 1$, the volume partition could not be specified since the calculations did not proceed to a point where the impending breakup is clear, because the neck of the drop had not stretched enough, as shown in Figure 2.13. For low resolution without node correction, the final snapshot before the drop hit the corner shows a neck just beginning to form. For higher resolution with node correction, the simulation proceeds to longer times and greater deformation, but it is still not clear whether or not breakup will occur. For Ca = 0.1, the drop does not deform enough to break for any flow ratio.

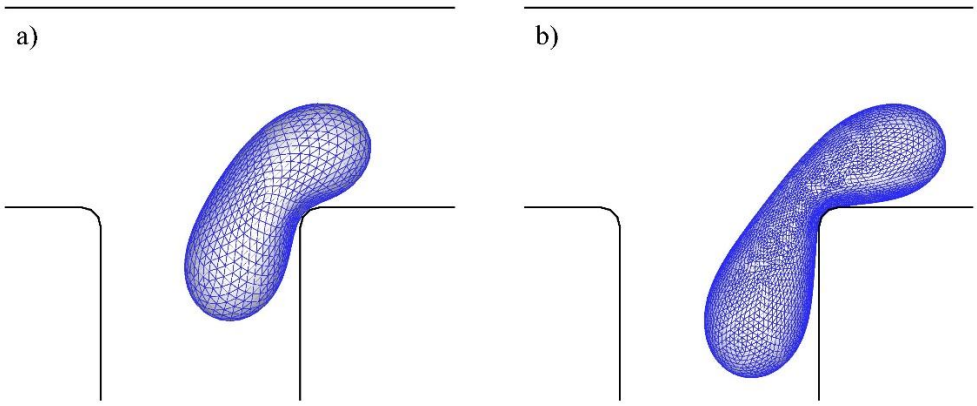

Figure 2.13. Effect of node correction on the final drop shape.

Final snapshots (before the code fails) of a drop with relative radius R = 0.4, Ca = 0.2, viscosity ratio λ = 1.0, and flow ratio Q_1/Q_2 = 1.0, with a) t = 4.70, $N_\triangle$ = 2160 and no node correction, and b) t = 5.90, $N_\triangle$ = 8640 and δ = 0.0005.

2.4.4. Effect of the viscosity ratio

Six different viscosity ratios between the drop and the bulk fluid were studied: $\lambda = 0.25$, 0.5, 1.0, 2.0, 3.0 and 5.0. Figure 2.14 shows for which flow ratios the drop goes through one of the channel branches versus breaking and partitioning between the branches. Stone et al. (1986) showed that flow-induced breakup is more difficult when the viscosity ratio is different from unity. Our results are consistent with this finding, as the critical flow ratio range decreases when the viscosities of the drop and the carrier fluid are different, because the drop then is more difficult to break. We found, also, that for drops with higher viscosity than the bulk fluid, the impending breakup range is wider than in the opposite case, and it does not substantially vary between the two values we studied.

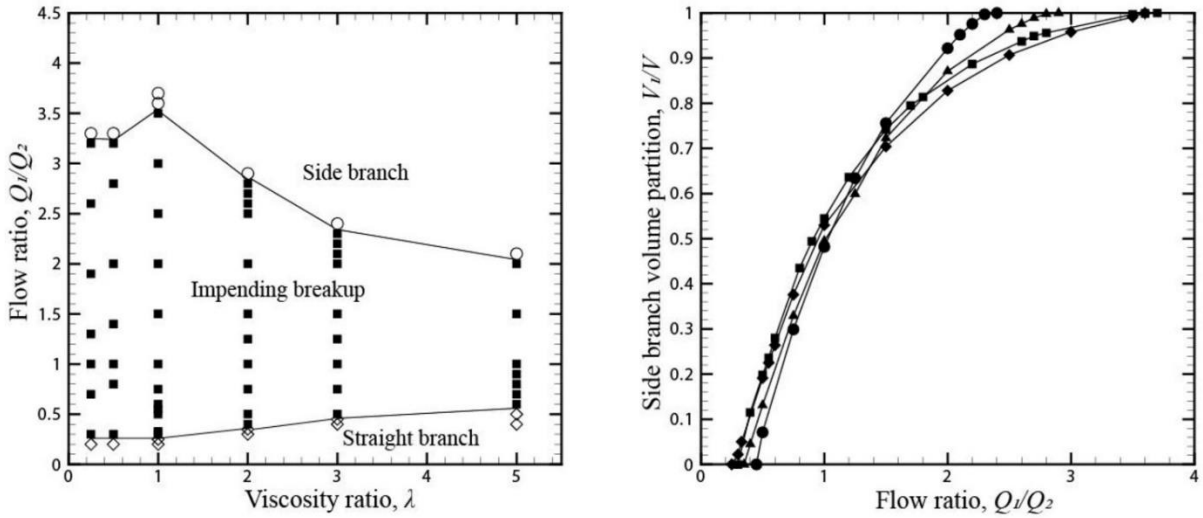

Figure 2.14. Outcome map and volume partition of drops with different viscosity ratios.

Flow ratios (left panel) in the impending-breakup zone (■) and in the non-breakup zones (side branch (○) and straight branch (◊)) for drops with relative radius R = 0.4, capillary number Ca = 0.8, number of triangles $N_\triangle$ = 2160, and viscosity ratios λ = 0.25, 0.5, 1.0, 2.0 3.0 and 5.0. The right panel shows volume partition vs. flow ratio for viscosity ratios λ = 0.25 (■), 1.0 (◆), 2.0 (▲), and 3.0 (●).

The right panel of Figure 2.14 provides a plot of the volume partitioning versus flow ratio. Again, the case of equal viscosities provides the largest range of flow ratios leading to breakup, as drops with viscosity the same as the surrounding fluid most easily break (Stone et al., 1986). The most viscous case ($\lambda = 5.0$) is not included, because the slower stretching of the more viscous drop with impending breakup was not sufficient to determine the partition ratio before the code crashed due to the close proximity of the drop and the corner. For $\lambda < 1$, only $\lambda = 0.25$ is represented, since both values ($\lambda = 0.25$ and 0.5) have the same critical flow ratio range.

2.5. Relevance to microfluidics

The present BI simulations assume small Reynolds numbers Re << 1 for the Stokes equations to apply, with moderate capillary numbers Ca = O(0.1 - 1) for substantial drop deformation. Satisfying both conditions formally requires very high viscosities and/or low interfacial tensions. First, of practical interest is to explore the relevance of the present simulations to flows in microfluidic devices with moderate Reynolds numbers. Without the full Navier-Stokes solution for a drop in our algorithm, a much easier (although not as rigorous) way to probe the importance of inertial effects is to replace the unperturbed Stokes flow solution $\mathbf{u}_\infty(\mathbf{y})$ on the drop surface in (2.13) by the moderate Reynolds number solution for a 2D flow in a T-junction without a drop. We then trace the effect of this change on the subsequent drop-shape dynamics. To this end, an in-house algorithm was used to generate $\mathbf{u}_\infty(\mathbf{y})$ on a fine Cartesian grid (of mesh size $\Delta x_i = 0.005H$) with Poiseuille flow boundary conditions on the inlet/outlet sections (all chosen to be $4H$ away from the nearest junction corners). No corner smoothing was used in this test. The Reynolds number $\mathrm{Re} = Q/\nu_e$ is based on the inlet flow rate per unit depth Q (see Section 2.2) and carrier-fluid kinematic viscosity ν_e. In the range $0 \leq \mathrm{Re} \leq 30$, the steady-state finite-difference

solution was obtained iteratively in the standard stream-function-vorticity formulation (Roache, 1972), with under-relaxation necessary for Re $\geq$ 10. The iterative nature of this method makes it applicable for Re = 0 as well. This solution was then interpolated to the drop surface in dynamical BI simulations. As elsewhere in this work, the bullet-like shape and drop centerline position close to the inlet were used as the initial condition. For R = 0.4, λ = 1, Ca = $\mu_e U/(H\sigma)$ = 0.8, and Q_1/Q_2 = 1, Figure 15 demonstrates the comparison of the drop shape and position achieved for different Reynolds numbers at the same time moment t = 1.7, when the drop is already well into the junction (but still not close to the sharp right corner, to avoid inaccuracies in the finite-difference solution for $\mathbf{u}_\infty(\mathbf{y})$). At Re << 1, there is a very good agreement for $\mathbf{u}_\infty(\mathbf{y})$ with the result obtained by our BI simulation. There are barely noticeable changes in the drop shape and position when Re varies from 0 to 10, and only modest changes when Re is further increased to 30, as shown in Figure 2.15. Hence, the formal requirement Re << 1 is too conservative, and the use of Stokes equations appears justified in the present problem for much higher Reynolds numbers. A possible explanation is that the Reynolds number here is based on the inlet conditions, where flow is the strongest but inertial effects are absent altogether (for $\mathbf{u}_\infty$).

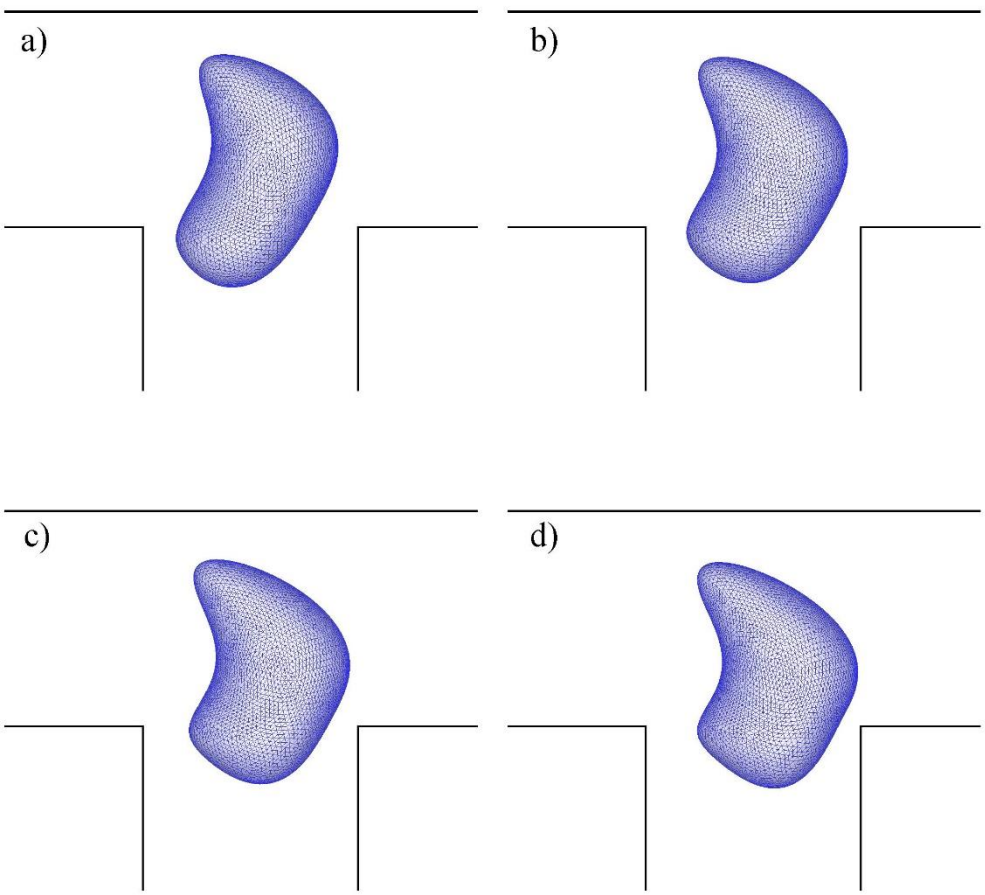

Figure 2.15. Drop shapes at different Reynolds numbers.

Drop with relative radius $R = 0.8$, capillary number $Ca = 0.8$, viscosity ratio $\lambda = 1.0$ in a channel with flow ratio $Q_1/Q_2 = 1.0$ at $t = 1.7$ for Reynolds numbers a) $Re << 1$, b) $Re = 10$, c) $Re = 20$ and a) $Re = 30$.

Armed with this knowledge, it is easy to demonstrate relevance of the present problem formulation to flow in practical microfluidic devices, if the carrier fluid is at least an order of magnitude more viscous than water (which still includes many liquids, such as glycerol or polymer solutions) or if a surfactant is used to lower the interfacial tension. Volumetric flow rates of 3 mL h^{-1} through channels of $H \sim$ 30 µm across are not uncommon (even for highly concentrated, effectively very viscous emulsions (Rosenfeld et al., 2014)), with average flow velocities $U \approx 1.5$

m s^{-1} in a channel. Such velocities can be even more realistic for single drops in wider channels $H \approx 100$ μm. For $v_e = 10^{-5}$ $m^2 s^{-1}$ (10X that of water) and surface tension of $\sigma = 30$ mN m^{-1} (typical), these estimates give the capillary number of Ca ≈ 0.5, close to the values used herein; the Reynolds numbers for H = 30 - 100 μm are Re 5 - 15, well within the effective Stokes regime, as the above analysis shows. In prior experiments on drops in a T-junction, smaller values of Ca were generally reported, rarely reaching 0.25 (Jullien et al., 2009). Those experiments, though, are for a very different setup, with relatively large tightly fitting drops fed through the central branch. Also, in such experiments, the capillary number was based on the drop velocity near the T-junction, not on the (larger) far-field velocity away from it.

2.6. Concluding remarks

Our moving-frame, boundary-integral algorithm has been shown to be effective in determining the motion and deformation of a viscous deformable 3D drop in a T-shaped microchannel. In most simulations, a drop is placed in one of the lateral arms of the microchannel. Depending of the flow ratio Q_1/Q_2, it may either continue straight, be diverted into the stem, or break due to the contact with the corner of the channel. For the latter, the size of the daughter droplet proceeding into each outlet channel is calculated. In all cases, the interaction between the drop and the corner of the channel was strong, so we chose to slightly smooth the corners of the microchannel in order to provide a lubricating layer that hampered early drop-wall contact and allowed the simulations to proceed further. The degree of smoothing did not have a substantial effect on the outcomes, so we selected corners smoothed by three flat panels, each of length 5.2% of the channel height, for most of the calculations. This smoothing allowed us to compare our dynamics of drop neck thinning prior to breakup with the local, self-similar solution

of Lister & Stone (1998) for a drop in unbounded fluid , where the ultimate non-dimensional slope $|dr_{eq}/dt|$ at breakup is 0.0341/Ca for a system with matching drop and carrier fluid viscosities. Unexpectedly, for most part of the final neck thinning, our slope $|dr_{eq}/dt|$ closely agrees with this prediction, despite close proximity of the corner to the neck. At larger times, when the neck becomes more curved and wraps around the corner, the thinning rate $|dr_{eq}/dt|$ falls below the prediction, because a larger portion of the neck meets lubrication resistance from the flat walls near the corner. In an additional simulation, with a drop entering the stem of the T-channel, so that it encountered a flat wall rather than a corner, excellent agreement of our numerical results with the self-similar solution of Lister & Stone (1998) was obtained.

We also studied the effect of varying the physical properties of the drop. When the relative radius of the drop is small (for the same capillary number), the range of flow ratios for impending breakup is small, since the drop does not deform much and can move through the side or straight channel and avoid contact with the corner. For small capillary numbers, the drop also does not deform much and it is able to avoid hitting the corner, so the range of critical flow ratios for which the drop breaks is narrower. Indeed, a critical drop size or capillary number was found, below which no breakup was observed. Finally, a drop of different viscosity than the bulk fluid also deforms less and is more difficult to break than a drop of the same viscosity as the bulk fluid, so it more easily passes into one of the branches of the channel without breaking.

In general, the moving-frame, boundary-integral method provides for a highly accurate description of drop dynamics, neck thinning, and breakup, which may offer an advantage over volume-of-fluid, front-tracking and other simulation methods. However, a potential limitation of boundary-integral methods is their restriction to linear equations, without inertia, and thus $Re << 1$. Although the present boundary-integral method is formally valid for $Re << 1$, it can be applied

to flow-driven motion of a deformable drop in a T-junction at much higher Reynolds numbers Re ~ 10 (and, approximately, even for Re = 30). In the future, our algorithm can be used in studies of the dynamic behavior of drops in more complex channel with multiple bifurcations. It may also be used to predict the conditions that give rise to a variety of desired shapes.

Chapter II Simulation of drop motion and breakup in narrow pores

This work has been published in the *Chemical Engineering Science*:

Navarro, R., Maristany, A., & Davis, R. H. (2021). Simulation of drop motion and breakup in narrow pores. *Chemical Engineering Science, 229*, 116057.

https://doi.org/10.1016/j.ces.2020.116057

Abstract

We used a boundary-integral algorithm to simulate drops passing through narrow pores, with three possible outcomes: passage without breaking, breakup due to contact with a bifurcation or corner, and breakup due to elongation. Smaller drops with low capillary numbers and high viscosities are more likely to go through the pores without breaking, larger drops are more prone to hit a pore bifurcation and break, and drops with large capillary numbers and same or lower viscosities than the bulk fluid are more likely to experience elongation and breakup. Pore geometry also has a strong effect, with relatively little breakup when there is no bifurcation. Finally, the post-pore size distribution of droplet sizes is relatively broad when the pre-pore size of the parent drops is large, but the post-pore size distribution is narrow for smaller parent drops (due to little or no breakup). These results may help guide emulsification processes.

3.1. Introduction

3.1.3. Importance of the problem

Separation processes account for 40 – 90% of capital and operating costs in the food, material processing, chemical and petrochemical industries, and filtration is one of the fastest and most profitable techniques among them (Haan & Bosch, 2013). Microfiltration of drops and particles is widely used in biopharmaceuticals (Davis, 2019) and other industries, accounting for 40% of the sales in the membrane market in the USA and Europe (Huisman, 2000) Another relevant and relatively novel application is membrane emulsification, which consists of producing single and multiple emulsions with nearly uniform droplet sizes and requires lower energy input than conventional mechanical methods (Charcosset, 2012; Joscelyne & Trägårdh, 2000). Due to the importance and popularity of membrane filtration and emulsification, these processes have received increased attention. While most efforts have been directed at particle trapping and membrane fouling (particulate microfiltration), and droplet formation techniques (direct emulsification), an important need is determine the conditions under which droplets passing through membrane pores will break into smaller droplets (premix emulsification).

3.1.2. Prior work and context for current study

There is a large body of experimental and modeling research on drop motion at small Reynolds numbers through tubes, with and without constrictions. Hetsroni et al. (1970) modeled a spherical drop moving axially within a circular tube, followed by experiments by Ho & Leal (1975) for drops of size comparable to the tube diameter. Olbricht & Leal (1982) performed experiments on droplet motion through a tube of varying diameter, whereas Tsai & Miksis (1994) analyzed the possibility of drop breakage as it moved through a constriction. Martinez & Udell

(1990) introduced the boundary-integral method for analyzing drop motion through a periodically constricted tube. Subsequent experiments by Cobos et al. (2009) examined the flow of oil-in-water emulsions through a constricted capillary, including blockage by drops larger than the constriction at small capillary numbers. More recently, Zhang et al. (2017) modeled droplet squeezing through a much smaller constriction, determining a minimum impulse to overcome the Young-Laplace pressure. Liang et al. (2015) identified a minimum pressure to push a drop through a constricted capillary and presented a nice review of related literature.

While the works cited above, as well as numerous related studies, provide important understanding of drop motion and possible trapping in pore-like structures, we are interested in the novel (but related) issue of possible breakup as a drop passes through a pore constriction that is larger than the drop diameter (so trapping does not occur). Moreover, we seek to understand the role of pore bifurcations on drop breakup, which is not addressed in prior work on droplet motion through single tubes with and without constrictions.

Another field of related research that has examined drop motion through bifurcations is microfluidics. T-junctions, in particular, have been widely used for the formation of drops of controlled size (Christopher & Anna, 2007; Navarro et al., 2020; Nekouei & Vanapalli, 2017). Of more direct relevance to the current work is the motion of pre-formed single drops through T-junctions. Most commonly, they are introduced through the stem and then undergo stretching and potential breakup when they reach the top of the stem, due to equal outflow through the two arms at the top of the T (e.g., Jullien et al., 2009; Link et al., 2004). Modeling drop motion, deformation, and breakup in microchannels with bifurcations has included volume-of-fluid methods (e.g., Hoang et al., 2013), lattice-Boltzmann algorithms (e.g., Chen & Deng, 2017), and boundary-integral methods (e.g., Navarro et al., 2020).

The flow of drops through porous media, along with potential breakup into smaller droplets, is also relevant. Prior studies have included flow through beds of both fibers (e.g., Mosler & Shaqfeh, 1997; Patel et al., 2003) and spheres (e.g., Davis & Zinchenko, 2009; Nazir et al., 2013; Zinchenko & Davis, 2013). A review of the motion of deformable drops through porous media was provided by Zinchenko & Davis (2017).

Turning our attention to membrane filtration of emulsion droplets, the current problem is closely related to "premix" membrane emulsification, in which a preformed coarse emulsion with a broad size distribution is filtered to form a more narrow distribution of smaller droplets. Early work on pre-mix emulsification demonstrated that membranes and thin packed beds could yield very narrow size distributions, especially with multiple passes (Liu et al., 2011; Suzuki et al., 1998; Van Der Zwan et al., 2006; Vladisavljević et al., 2004). More recent work has expanded this technique to include multiple emulsions and nanoemulsions (Alliod et al., 2019; Eisinaite et al., 2016; Gehrmann & Bunjes, 2017; Joseph & Bunjes, 2012; Nishihora et al., 2020). Excellent reviews are provided by Nazir et al. (2010) and Vladisavljević (2019). This technique differs from "direct" membrane emulsification, (c.f., Joscelyne & Trägårdh, 2000), in which the dispersed phase is pushed through the membrane and forms droplets at the membrane/continuous-phase interface. To achieve the smaller size distribution, either the larger drops must become trapped by the membrane, which would lead to undesirable membrane fouling and loss of dispersed phase, or break into smaller drops as they pass through the pores.

The conceptual process described by Vladisavljević et al. (2004) is that drops larger than the membrane pores squeeze into the pores when the pressure is above a critical value and then break into drops that can be smaller than the membrane pores when the breakup occurs at high shear stresses (see figure 2 in their paper). Indeed, they obtained mean droplet sizes with multiple

passes that are slightly smaller than the mean pore size of a porous glass membrane. Nazir et al. (2013) used a different geometry of premix emulsification or homogenization through a packed bed of small glass beads supported by a metal sieve, as previously studied by Van Der Zwan et al. (2008), and obtained droplet sizes typically 2 - 5 times smaller than the interstitial void size, with fluxes as high as 0.2 m/s (several orders-of-magnitude larger than for standard microfiltration membranes). Thus, the current simulation study is motivated by these experiments and is focused on droplets that are smaller than the pore or constriction sizes. Of particular interest is determining the conditions under which such droplets will break.

In this work, we present a general approach to predict whether viscous droplets (studied individually) will pass through different pore geometries without breaking or if smaller drops will be formed as a consequence of breakup. We consider drops that are smaller than the pores and break due to hydrodynamic interactions with the pore walls or due to capillary forces. We use a boundary-integral method (Pozrikidis, 1992), which has been widely used to study the behavior of drops in confined geometries such as parallel plates (Griggs et al., 2007; Janssen & Anderson, 2008), constricted tubes (Martinez & Udell, 2008), granular media (Davis & Zinchenko, 2009) and T-shaped channels (Navarro et al., 2020), amongst other geometries. The linearity of the Navier-Stokes equations for small Reynolds numbers (i.e., Stokes flow) allows us to develop an analytical solution for the whole domain calculated only on the nodes of a discretized surface. Although the work is primarily motivated by the flow of emulsion drops through membrane pores, it is expected to have broader applications, such as multiphase flow through porous media and droplet motion in microfluidic devices and capillary networks.

3.2. Methodology

3.2.1. Problem description

The objective of this work is to determine the conditions for which a deformable drop will pass through a narrow pore constriction without breaking, and the conditions for which it will break, by performing simulations that are fully resolved at the pore and droplet scale. A schematic of a droplet and one geometry is shown in Figure 3.1. The external carrier fluid has viscosity μ_e and density ρ_e, while the droplet has viscosity μ_d and density ρ_d. It is assumed that both fluids are Newtonian. For simplicity, we consider that the interface has constant interfacial tension σ, although it is noted that emulsions often include surfactants that lower the interfacial tension and cause interfacial tension gradients (Marangoni stresses) due to flow-induced gradients in surfactant concentration. Prior work (Gissinger et al., 2019) has shown that Marangoni stresses have only a modest effect on the critical conditions for drop trapping in constrictions. It is also assumed that the drop is neutrally buoyant ($\rho_d \approx \rho_e$) or is sufficiently small that gravitational sedimentation is negligible. The drop has undeformed radius a, and the pore constriction has height H. In the present study, $H > 2a$, so drop trapping does not occur – see prior work by our group on trapping by constrictions that are smaller than the drop (Ratcliffe et al., 2010, 2012; Ratcliffe & Davis, 2012; Zinchenko & Davis, 2006). Thus, our focus is on deformation and breakup of individual drops due to hydrodynamic stresses in narrow pores, rather than on emulsification or drop formation.

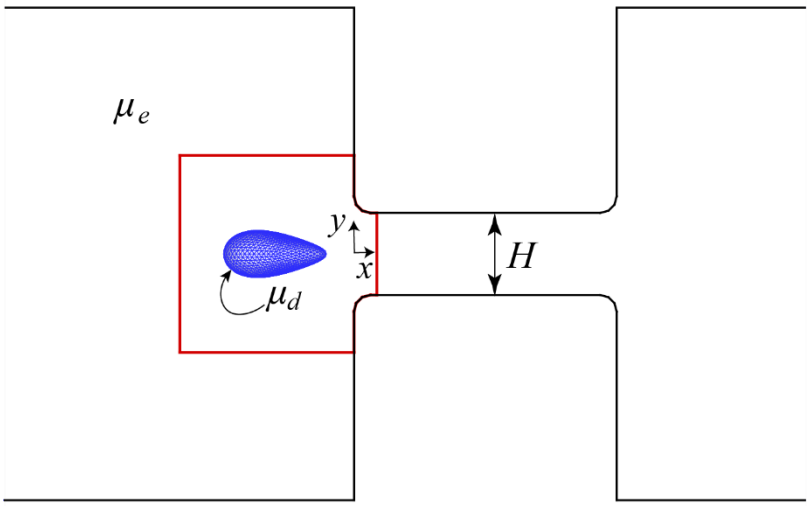

Figure 3.1. Schematic representation of a drop in a channel with a pore.

Schematic representation of a drop inside a computational box as it passes through a narrow pore with a constriction of height H.

We employ a moving-frame boundary-integral method (MFBIM), which provides high-accuracy resolution of particle (Zinchenko et al., 2012) and drop (Navarro et al., 2020) motion in complex microchannels. The computational box around the drop (see Figure 1) is referred as a "moving-frame", as described below. The pore is two-dimensional (i.e., it is wide in the direction perpendicular to the paper compared to its height H), due to limitations of the moving-frame algorithm (Zinchenko et al., 2012), but the drop and its motion and deformation are fully three-dimensional. The average velocity in the narrow constriction is $U = Q/H$, where Q is the volumetric flow rate per unit width through the pore.

Two primary dimensionless parameters governing this problem are the Reynolds number, $\mathrm{Re} = \rho_e UH/\mu_e$ and the modified capillary number $\mathrm{Ca_m} = \mu_e Ua/(\sigma H)$, where σ is the interfacial tension. The Reynolds number represents a ratio of fluid inertia and viscous forces and is assumed small ($\mathrm{Re} \ll 1$), so that viscous forces dominate and the linearized Stokes equations govern the

motion. As shown in a companion study (Navarro et al., 2020), however, the MFBIM is expected to be accurate up to Re ≈ 10. The modified capillary number represents a ratio of viscous deforming forces to interfacial restoring forces and is assumed moderate ($\mathrm{Ca_m} \approx 0.1$ - 1), so that deformation and breakup occur. Typical membrane emulsification systems involve vegetable or other oils in water, either with or without surfactants as emulsifiers. However, several studies have also been done on water-in-oil emulsification (Link et al., 2004; Suzuki et al., 1998; Zhou & Pozrikidis, 1994). Oil viscosities are typically $\mu_d \approx 2 - 60$ mPa-s (Holzapfel et al., 2013; Lepercq-Bost et al., 2008; Van Dijke et al., 2010). The continuous phase may have polymer additives, such as polyethylene glycol or sodium alginate, resulting in viscosities of $\mu_e \approx 1 - 100$ mPa-s (Holzapfel et al., 2013; Vladisavljević et al., 2004). Interfacial tensions are relatively low, especially in the presence of surfactants, with typical values of $\sigma \approx 1 - 10$ mN/m (Lepercq-Bost et al., 2008; Van Dijke et al., 2010). The fluxes for premix emulsification of up to 0.01 m/s (Vladisavljević et al., 2004) are much larger than for conventional direct membrane emulsification (with the velocities U in the pore necks even higher, depending on the porosity and pore structure), while superficial velocities through packed beds of glass beads for premix emulsification are as high as 0.2 m/s (Nazir et al., 2013). Typical pore constriction diameters are $H \approx 1 - 30$ μm (Holzapfel et al., 2013; Nazir et al., 2013; Vladisavljević et al., 2004). Using $\rho_e \approx 10^3$ kg/m^3, typical dimension parameters are Reynolds number of $\mathrm{Re} = \rho_e UH/\mu_e < 6$ and unmodified capillary numbers of $\mathrm{Ca} = \mu_e \mathrm{U}/\sigma < 0.2$ for pure water as the continuous phase, or $\mathrm{Re} < 0.3$ and $\mathrm{Ca} < 4$ if the continuous phase is oil or a water/polymer mix with viscosity 20 times that of water.

In this work, we consider $\mathrm{Re} \lesssim 1$ and $\mathrm{Ca_m} \approx 0.1 - 1$, so that the Stokes equations apply with negligible inertia and drop deformation is significant. The latter typically requires that the external fluid be more viscous than water (e.g., an oil or a polymer solution) and/or that the

interfacial tension is substantially reduced by surfactants. For computational ease, the viscosity ratio $\lambda = \mu_d/\mu_e$was set to unity for most of the simulations, but larger and smaller values were used in one parametric study. Besides the physical properties of the fluids, the initial position of the drop inside the pore entrance region also has a significant effect on the outcome of this problem.

3.2.2. Moving-frame boundary-integral method

When the Reynolds number is small compared to unity, viscous forces dominate over inertia, and the nonlinear Navier-Stokes equations simplify to the linear Stokes equations to describe fluid flows. Then, the fundamental solution to the Stokes equations (representing the flow and stresses generated due to a point force in a fluid) may be used along with the reciprocal theorem and divergence theorem to convert the governing differential equations within a volume domain to integral equations on the boundary of the domain (Temam, 1977). This so-called boundary-integral method is particularly effective for deforming droplets, since it allows for the drop position and shape to be followed in time (Zinchenko & Davis, 2006b). For the motion of deformable drops through a narrow pore, however, the pore length and complexity can be sufficiently great that the computational requirements to discretize the entire pore and drop boundaries are too large. Thus, our group previously developed a 'moving-frame' algorithm to efficiently handle such complex geometries, first for solid particles (Zinchenko et al., 2012) and later for deformable drops (Navarro et al., 2020). In this approach, a computational cell encloses the particle or drop, and the undisturbed velocity for the complex geometry (without the particle or drop) is applied to the boundary of the computational cell. The cell or moving frame then moves with the drop through the channel and stretches as the drop deforms.

As in Zinchenko et al., (2012), a two-dimensional moving-frame with surface S_∞ around the drop is used. The moving frame is built around the drop centroid as a cubic box that intercepts

the pore walls, so its boundaries consist on straight-line contour panels $\mathcal{L}_{i,i+1,\ldots,M}$ (see figure 3.2b). The moving frame is large enough so it can be assumed that, at its boundaries, the undisturbed velocity of the flow is not affected by the presence of the drop, yet is much smaller than the whole membrane pore (which significantly reduces the computational cost of our simulations). In our calculations, the cubic box initially had sides of length 3 times the undeformed drop diameter and then was stretched in proportion to the deformed drop length. Our previous work showed that this frame size gave results within 1% of the full BIM without a computational box (Navarro et al., 2020).

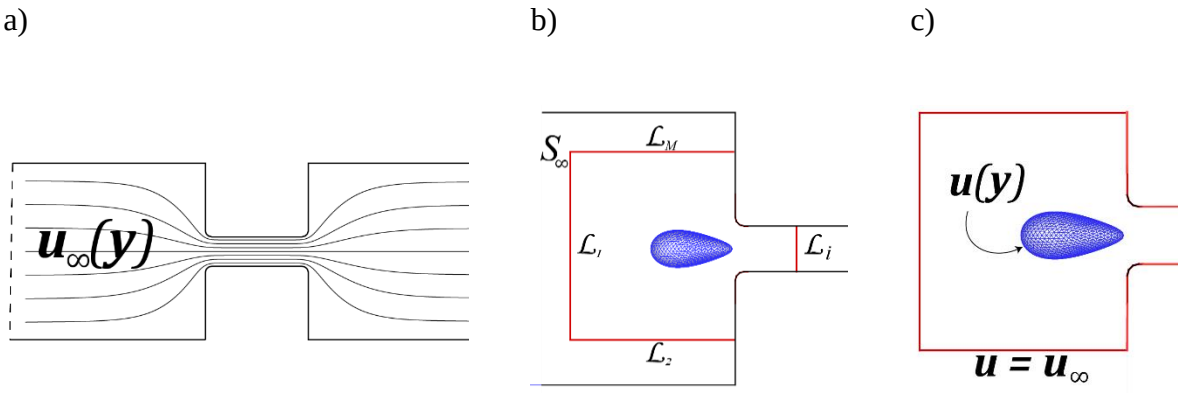

Figure 3.2. Schematic representation of the MF BI algorithm.

Schematic representation of the moving-frame boundary-integral algorithm, where a) is the 2D pore for which the velocity of the undisturbed fluid is initially calculated, b) represents the moving frame and its panels around the drop in the pore, and c) shows the velocity values on the drop surface and on the frame boundary.

First, the undisturbed velocity field $\boldsymbol{u}_\infty(\boldsymbol{y})$ inside the channel geometry (i.e., the flow inside the pore when the drop is not present, see figure 2a) is calculated (Zinchenko et al., 2012):

$$\boldsymbol{u}_\infty(\boldsymbol{y}) = \sum_{i=1}^{M} 2 \int_{\mathcal{L}_i} \boldsymbol{q}_\infty(\boldsymbol{x}) \cdot \boldsymbol{\tau}^{\boldsymbol{2D}}(\boldsymbol{r}) \cdot \boldsymbol{n}(\boldsymbol{x}) ds_x \,, \quad (3.1)$$

where $\boldsymbol{r} = \boldsymbol{x} - \boldsymbol{y}, \boldsymbol{y}$ is a location within the flow domain at which the velocity is calculated, $\boldsymbol{x}$ is a point on the domain boundary over which integration is made, $\mathcal{L}_i$ is the i-th contour panel, s_x is the length element, and $\boldsymbol{\tau^{2D}}$ is the fundamental stresslet in two dimensions: $\boldsymbol{\tau^{2D}}(\boldsymbol{r}) = \boldsymbol{rrr}/(\pi r^4)$. In the algorithm, the pore walls and other boundaries (entrances and exits) are discretized on a Cartesian grid to numerically perform the integration. The potential density $\boldsymbol{q}_\infty(\boldsymbol{x})$ on the domain boundary is calculated using the biconjugate-gradient method from the expression (Navarro et al., 2020):

$$\tilde{\boldsymbol{q}}_\infty(\boldsymbol{y}) = \boldsymbol{u^b}(\boldsymbol{y}) - 2\int_{\mathcal{L}} \tilde{\boldsymbol{q}}_\infty(\boldsymbol{x}) \cdot \boldsymbol{\tau^{2D}}(\boldsymbol{r}) \cdot \boldsymbol{n}(\boldsymbol{x}) ds_x + \tilde{\boldsymbol{q}}_\infty{}'(\boldsymbol{y}) - \frac{\boldsymbol{n(y)}}{L}\int_{\mathcal{L}} \tilde{\boldsymbol{q}}_\infty(\boldsymbol{x}) \cdot \boldsymbol{n}(\boldsymbol{x}) ds_x, \quad (3.2)$$

with $\mathcal{L}$ the total contour length, $\boldsymbol{u^b}$ the velocity on the boundaries, and the prime on $\tilde{\boldsymbol{q}}_\infty{}'$ denotes the projection of a vector field onto the space of rigid-body motions with a previous transformation $\boldsymbol{q}_\infty(\boldsymbol{x}) = \tilde{\boldsymbol{q}}_\infty(\boldsymbol{x}) - \frac{1}{2}\tilde{\boldsymbol{q}}_\infty{}'(\boldsymbol{x})$. The potential density is later tabulated for fast calculation of $\boldsymbol{u}_\infty(\boldsymbol{y})$. Then, $\boldsymbol{u}_\infty(\boldsymbol{y})$ is applied on the boundaries of the moving frame (figure 2b) and, as described in (Navarro et al., 2020), the velocity $\boldsymbol{u}(\boldsymbol{y})$ of the droplet at each of its surface nodes is calculated (see figure 2c):

$$\boldsymbol{u}(\boldsymbol{y}) = \frac{2}{(\lambda+1)}\left[\boldsymbol{u}_\infty(\boldsymbol{y}) + F(\boldsymbol{y}) + 2\int_{S_\infty} \boldsymbol{q}(\boldsymbol{x}) \cdot \boldsymbol{\tau}(\boldsymbol{x}-\boldsymbol{y}) \cdot \boldsymbol{n}(\boldsymbol{x}) dS_x\right] + \frac{2(\lambda-1)}{(\lambda+1)}\int_{Sd} \boldsymbol{u}(\boldsymbol{x}) \cdot \boldsymbol{\tau}(\boldsymbol{x} - \boldsymbol{y}) \cdot \boldsymbol{n}(\boldsymbol{y}) dS_x, \quad (3.3)$$

where S_∞ and S_d are the boundary (computational cell around the drop) and drop interface, respectively, and $\lambda = \mu_d/\mu_e$ is the ratio between the droplet and the fluid viscosities. The boundary-integral equation for the density function is described by (Navarro et al., 2020)

$$\boldsymbol{q}(\boldsymbol{y}) = -\boldsymbol{F}(\boldsymbol{y}) - (\lambda - 1)\int_{Sd} \boldsymbol{u}(\boldsymbol{x}) \cdot \boldsymbol{\tau}(\boldsymbol{x}-\boldsymbol{y}) \cdot \boldsymbol{n}(\boldsymbol{x}) dSx - 2\int_{S_\infty} \boldsymbol{q}(\boldsymbol{x}) \cdot \boldsymbol{\tau}(\boldsymbol{x}-\boldsymbol{y}) \cdot \boldsymbol{n}(\boldsymbol{x})\, dSx - \frac{\boldsymbol{n(y)}}{S_\infty}\int_{S_\infty} \boldsymbol{q}(\boldsymbol{x}) \cdot \boldsymbol{n}(\boldsymbol{x}) dS_x, \quad (3.4)$$

where $\boldsymbol{F}(\boldsymbol{y}) = \frac{1}{\mu_e}\int_{Sb} \boldsymbol{G}(\boldsymbol{x}-\boldsymbol{y}) \cdot 2\sigma k(\boldsymbol{x}) \cdot \boldsymbol{n}(\boldsymbol{x}) dSx$, $\boldsymbol{G}$ is the free-space Green tensor defined as $\boldsymbol{G} = (\boldsymbol{I}/r + \boldsymbol{rr}/r^3)/8\pi$, which is a velocity field associated with a point force acting at $\boldsymbol{y}$, $\boldsymbol{\tau}(\boldsymbol{x}-\boldsymbol{y}) = (3/4\pi)\boldsymbol{rrr}/r^5$ is the fundamental stresslet, and $k(\boldsymbol{x})$ is the curvature of the drop surface. By use of the density function along with the free-space Green's function, the effect of the bounding walls on the drop deformation and motion are fully taken into account.

To solve (3.3) and (3.4), the drop surface is discretized with triangles, while the flat boundaries are discretized with rectangles. For small drops not too close to the bounding walls, 3840 triangles on the drop and about 6000 rectangles on the walls gave accurate resolution. For larger drops and close drop-wall encounters, the resolution was increased to 6000 triangles on the drop and about 14,000 rectangles on the bounding walls. Further discussion of the method and its convergence is provided in Navarro et al. (2020).

3.2.3. Types of constrictions

The behavior of a deformable droplet through three idealized microchannel geometries was studied. The first model system represents a pore with a symmetric Y-bifurcation that comes after a constriction following a much wider reservoir or pore mouth (figure 3.3a). The second model system is similar to the first, but the constriction leads to another reservoir instead of a bifurcation (figure 3.3b), and is called an H-constriction. Finally, the third model system represents the flow between two circular beads or fibers (figure 3.3c), and is called a circular constriction. All pore geometries generated with flat panels because our algorithm is based on straight lines and not curved segments, but it was possible to create curved-like figures by connecting several short straight-line segments. This technique was also used to "smooth" (Navarro et al., 2020) sharp corners (where lubrication is not strong enough to prevent drop-wall contact and so simulations

fail) present in the pores with Y-bifurcations and H-constrictions. In these cases, three small segments were connected to give the corners a more round shape.

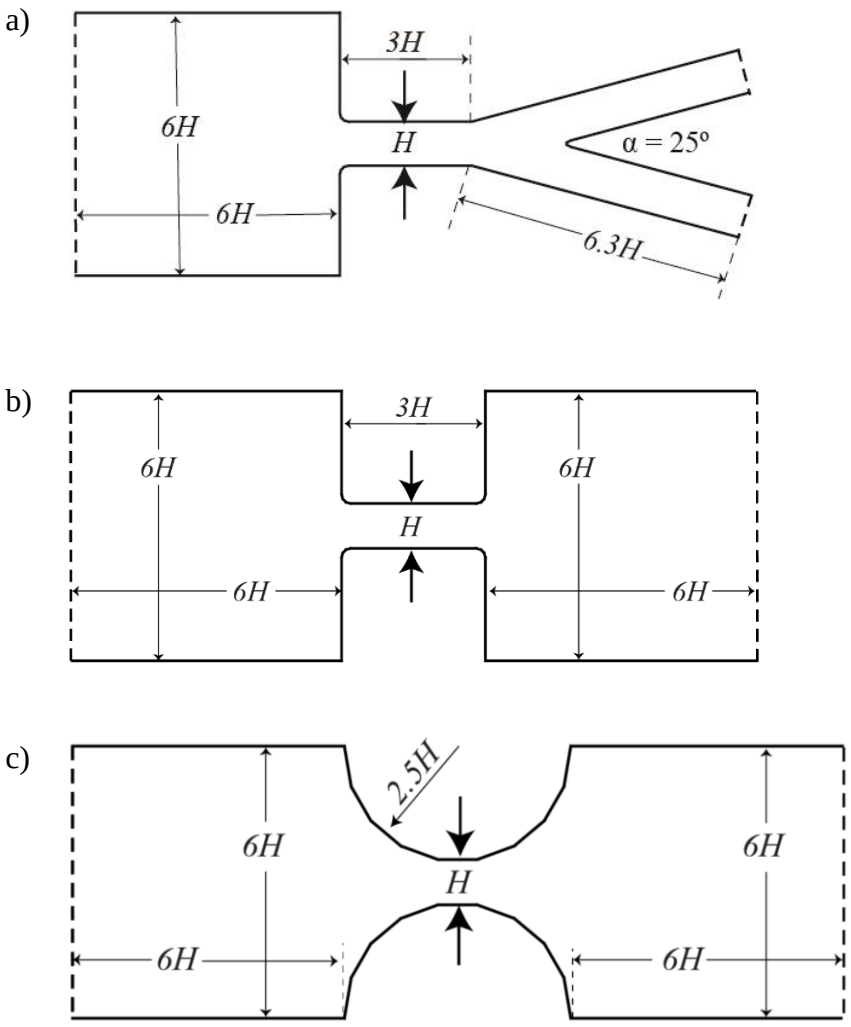

Figure 3.3. Schematic representation of the three different pore geometries.

Schematic representation of the three different pore geometries studied: a) Y-bifurcation, b) H-constriction and c) circular constriction. The solid lines represent the pore boundaries, while the dashed lines are the entrances and exits.

The three geometries were chosen as models of different types of pores found in porous media and microfiltration membranes. Y-bifurcation devices are used in microfluidic devices for drop sorting and formation (Vladisavljević et al., 2012) and are characteristic of membranes with interconnected pores (Vladisavljević et al., 2004); the H-constriction is a model of narrow pores that are connected by larger reservoirs and of thin membranes with straight-through pores connecting the feed and permeate reservoirs for dead-end microfiltration (Suarez & Veza, 2000; Moritz et al., 2001) and membrane emulsification (Nakashima et al., 2000; Piacentini et al., 2014); and the circular constriction is a representative of cellular membranes and packed beds of beads (or fibers, for 2D geometries) used in macroporous filtration and emulsification (Kaade et al., 2020; Nagy, 2018; Nazir et al., 2013). Figure 3.4 shows examples of magnified membranes with various pore distributions and sizes that approximate a) a Y-bifurcation (Apel, 2001), b) an H-constriction (Apel, 2001), and c) a circular constriction (Ciurans Oset et al., 2018).

a) b) c)

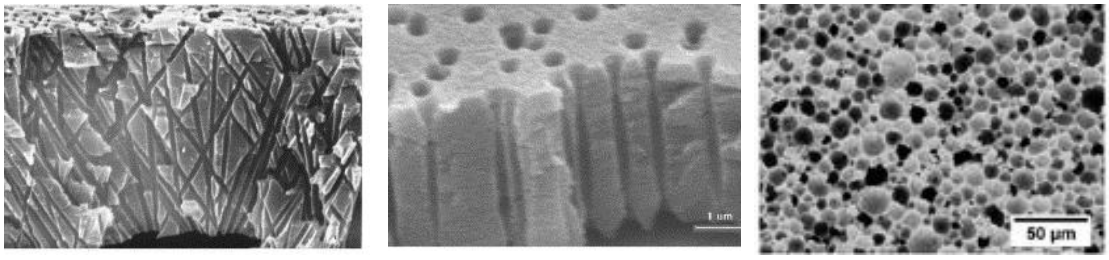

Figure 3.4. Magnified membrane cross sections with different pore types.

Magnified membrane cross sections with various pore distributions and sizes modeled by a) a Y-bifurcation made of polypropylene (from (Apel, 2001), copyright Elsevier), b) an H-constriction made of polyethylene terephthalate (from (Apel, 2001), copyright Elsevier), and c) a circular constriction made of cellular alumina foam (from (Ciurans Oset et al., 2018), copyright Elsevier).

3.2.4. Nondimensionalization and calculation procedures

In the calculations, the lengths were made nondimensional with the constriction height, *H*, and all the velocities were made nondimensional with the average velocity, *U*, in the narrowest part of the constriction. Time was nondimensionalized with *H/U*. Then, besides geometric parameters, the calculations have three dimensionless input parameters: (i) the capillary number $\mathrm{Ca} = \mu_e U/\sigma$ or modified capillary number $\mathrm{Ca_m} = \mu_e U a/(\sigma H)$, (ii) the viscosity ratio $\lambda = \mu_d/\mu_e$, and (iii) the ratio of drop diameter and constriction height, $d = 2a/H$. The Reynolds number $\mathrm{Re} = \rho_e U H/\mu_e$, is assumed small compared to unity, so that viscous effects dominate over fluid inertia and the Stokes equations (rather than the full Navier-Stokes equations) apply.

A Cartesian coordinate system is used, with *x* in the horizontal direction (in the direction of the inlet flows) and *y* is in the vertical direction (perpendicular to the inlet flow). The origin of the coordinate system is placed along the center plane at the inlet of the constriction (see Figure 1). Each calculation starts with an initially spherical drop, centered at a location $\boldsymbol{x_0} = (x_0, y_0)$ in this coordinate system. The studied range of starting positions was $x_0 = \{-6, -1\}$ in the horizontal direction and $y_0 = \{-3 + d/2, 3 - d/2\}$ in the vertical direction. The drop centers were not started within a distance a of the top and bottom walls or within a distance H of the vertical wall at the constriction entrance, to avoid overlap and prevent the code from falling due to tight drop-wall interactions near the constriction entrance. The simulation follows the drop motion and deformation as the drop passes through the constriction. All calculations were performed using a FORTRAN code written by our group. A typical calculation of one drop trajectory required about two days on a six-core processor machine. Over 1200 trajectories were calculated to map out the outcomes parameter space for the three geometries.

3.2.3. Potential outcomes

Case 1 is the scenario where the drop elongates and deforms, but does not reach a breakup situation, so it leaves the outlet of the pore intact (Figure 3.5a). In case 2, the drop breaks due to a strong interaction and contact with the corner at a bifurcation in the pore (Figure 3.5b). Finally, in case 3, the extensional component of the flow field and interaction with a side wall causes the drop to deform, making it longer and thinner (Figure 3.5c). Because of capillary hoop stresses, a neck that forms on a long drop will pinch off, resulting in the appearance of daughter droplets (Tan & Lee, 2005; Tjahjadi et al., 1992). In the current work, we stop the simulations just prior to neck pinch off, as following two (or more) daughter drops requires significant modifications to the moving-frame algorithm. Nevertheless, the simulations allow determination of the sizes of the daughter drops, which is of primary interest in the current work. Further details on neck pinch off and drop breakup are given in Navarro et al. (2020).

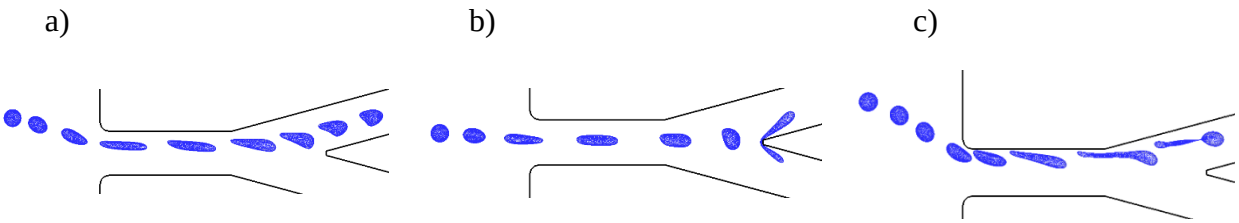

Figure 3.5. Potential outcomes for a drop in a membrane pore network.

Drop with relative diameter $d = 0.4$, modified capillary number $Ca_m = 0.6d = 0.24$, viscosity ratio λ = 1.0, and initial positions inside the pore entrance region of a) $\boldsymbol{x_0}$ = [-2.0 , 0.8] going through the pore without breakup, b) $\boldsymbol{x_0}$ = [-2.0 , 0.2] hitting one of the pore walls and breaking, and c) $\boldsymbol{x_0}$ = [-2.0 , 1.5] breaking due to elongation.

3.3. Results & Discussion

In this section, the results obtained for each geometry are presented and the effects of the physical properties of the drop are analyzed. Results are summarized as outcomes maps (showing

which starting locations lead to each of the three outcomes) and as tables showing the percentage of drops resulting in each of the three outcomes, assuming that they start with uniformly distributed initial positions.

3.3.1. Effect of the drop size and capillary number in the Y-bifurcation

The streamlines and velocity profiles for the undisturbed Stokes flow inside the Y-bifurcation are represented in Figure 3.6. Parabolic flow is imposed on the entrance and exits, with the total mass (and, hence, volume, since density is assumed constant) flow rate conserved. The entrance flow converges into the restriction, where the velocity is increased due to the smaller cross-sectional area. Then, the flow is equally split through the two branches of the Y-bifurcation. The dashed lines at the corners of the reservoir represent the boundary of the recirculation zones, which are outside the range of starting positions for the drops.

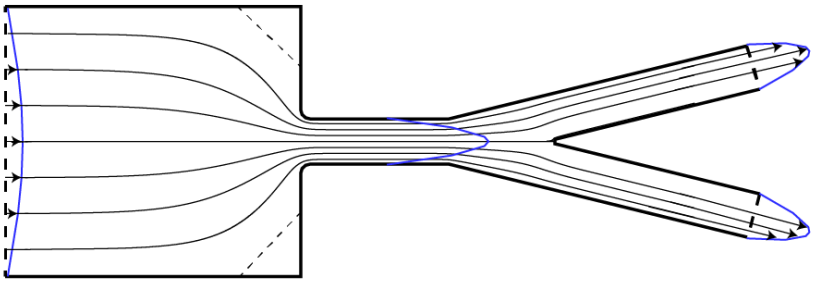

Figure 3.6. Schematic representation of a pore with a Y-bifurcation.

Flow streamlines, velocity profiles and recirculation zones inside a pore with a narrow constriction and Y-bifurcation.

Figure 3.7 shows outcomes maps for the Y-bifurcation for several drop sizes and capillary numbers. The outcomes maps were obtained by running numerous simulations with drops starting on a grid of initial locations (x_0, y_0) and then finding the boundaries of the different outcome

zones. The frequency of drop breakup increases with both the modified capillary number and the drop size, as expected, due to increased deformation. The drop size has a greater impact on the increase of starting locations for direct breakup (black), because larger drops are more likely to wrap around the Y-bifurcation, while an increase of the modified capillary number creates a larger area of starting locations resulting in indirect breakup (dark gray), due to greater drop deform action. Note that drops of dimensionless diameter $d = 0.8$ break in all cases, regardless of their initial position inside the pore entrance region.

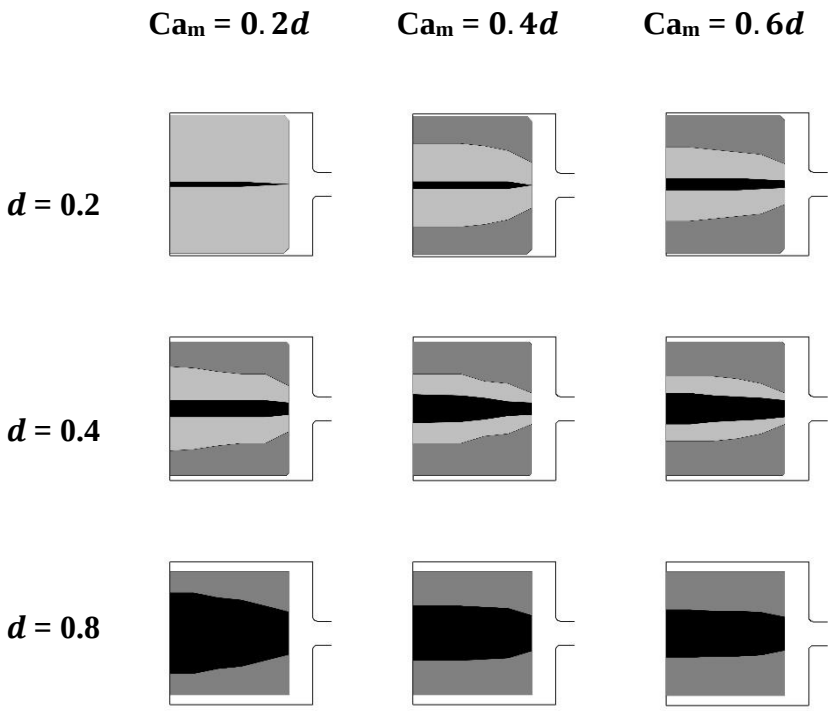

Figure 3.7. Outcome maps for a drop in a pore with a Y-bifurcation.

Outcomes maps for drops with viscosity ratio $\lambda = 1$, relative diameters d = 0.2, 0.4 and 0.8 and modified capillary numbers Ca_m = 0.2d, 0.4d and 0.6d. Light gray corresponds to the non-breakup zone, black corresponds to the direct breakup zone, and dark gray corresponds to the indirect breakup zone. The maps represent the initial drop locations associated with each outcome and span the range $-6 < x_0 < -1$ and $-3 + d/2 < y_m < 3 - d/2$, except there are small excluded regions in the top and bottom right corners for $d = 0.2$, due to the recirculation zones. When the capillary number is increased, the drop is more likely to break due to

elongational forces and, therefore, the indirect breakup zone is larger. Big drops are more prone to hit the corner of the bifurcation and break due to it.

The outcomes are further quantified in Table I. Here, "zone area" refers to the fraction of the initial drop locations within the inlet reservoir that result in a given outcome, as represented by the different shaded areas of the outcomes maps in Figure 7. In contrast, "inlet flux" refers to the percentage of droplets entering the left-hand-side of the inlet reservoir that subsequently experience a given outcome. It is again assumed that the drops are uniformly distributed initially, but they experience parabolic flow at the entrance and so there is a larger flux near the channel center plane than near its walls. Since the flow and outcomes are symmetric about the center plane, the inlet flux is given by

$$\% \text{ flux} = 100\% \quad \int_{y_{min}}^{y_{max}} [(1-(y/3)^2]\, dy \Big/ \int_0^{3-d/2} [(1-(y/3)^2] dy$$

$$= 100\% \ [y_{max} - y_{min} - (y_{max}^3 - y_{min}^3)/27] / [3 - d/2 - (3-d/2)^3/27], \qquad (3.5)$$

where y_{min} and y_{max} are the lower and upper boundaries of the zone of interest for positive y_0, on the left-hand-side (entrance) of the inlet reservoir. The constant 3 appears in (3.5) because the half-height of the inlet reservoir was set at $3H$ (see Figure 3a) for these simulations. As seen in Table 3.1, the inlet flux percentage leading to direct breakup is higher than the corresponding droplet fraction, due to the larger velocity near the channel center and the greater height of that zone at the reservoir entrance.

Table 3.1. Outcome percentages for a drop in a pore with a Y-bifurcation.

		% no breakup		% direct breakup		% indirect breakup	
	Ca_m	Inlet flux	Zone area	Inlet flux	Zone area	Inlet flux	Zone area
d = 0.2	0.2d	95%	97 %	5%	3 %	0%	0%
	0.4d	70%	43 %	8%	5 %	22%	52 %
	0.6d	58%	39 %	13%	8 %	29%	53 %
d = 0.4	0.2d	59%	41 %	17%	12 %	24%	47 %
	0.4d	37%	27 %	30%	17 %	33%	56 %
	0.6d	31%	21 %	32%	19 %	37%	60 %
d = 0.8	0.2d	0%	0%	70%	54%	30%	46%
	0.4d	0%	0%	56%	42%	44%	58%
	0.6d	0%	0%	49%	36%	51%	64%

Zone area and inlet flux percentages of each outcome for drops with d = 0.3, 0.4 and 0.8, Ca_m = 0.2d, 0.4d and 0.6d, and λ = 1.0 in a narrow pore with a Y-bifurcation.

3.3.2. Effect of the pore geometry

In this section, the effect of the pore geometry is presented, by examining the H-constriction and circular constriction. Figure 3.8 shows the outcomes map for the H-constriction. Only $d = 0.4$ and $\mathrm{Ca_m} = 0.24$ and 0.32 are shown, as smaller values of these parameters show no breakup, regardless of the initial position of the drop. As seen in this figure, most of the initial positions result in drops passing through the pore without breaking, and only those drops that start

near the upper or lower wall of the inlet reservoir experience indirect (elongational) breakup. Direct breakup was not observed.

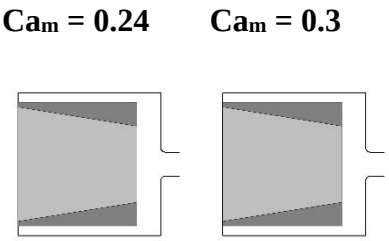

Figure 3.8. Outcome maps for a drop in an H-constricted pore.

Breakup maps for drops with viscosity ratio $\lambda = 1$, relative diameter $d = 0.4$, and capillary numbers Ca_m = 0.24 and 0.32 in an H-constriction. Light gray corresponds to the non-breakup zone and dark gray corresponds to the indirect breakup zone. Drop with initial positions closer to the wall experience indirect breakup, while drops starting away from the channel walls do not break.

Figure 3.9 shows snapshots of a drop trajectory without breakup and another one with indirect breakup. Indirect breakup occurs when the drop undergoes substantial stretching due to being very close to a wall as it passes through the constriction, and then undergoes neck thinning and pinch off as it relaxes upon exiting the constriction. The break occurs very close to the tail of the drop, so one of the daughter drops is much smaller than the other (see the final image of the lower drop in Figure 3.9). It is possible that the larger daughter drop would break again, but the current code does follow the daughter drops after the first break. For reference, the streamlines of the undisturbed flow in the H-constriction are included in Figure 3.9; the dashed lines in the corners represent the recirculation zones.

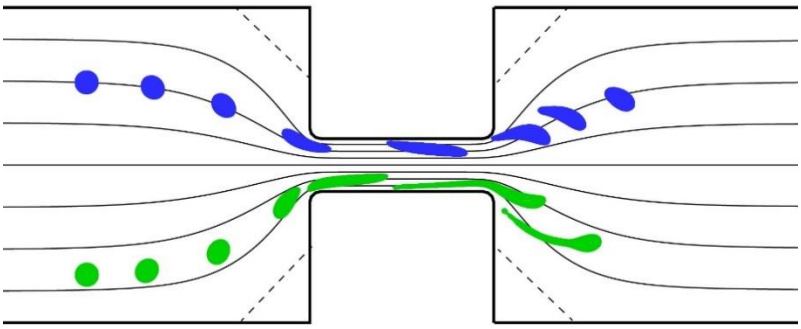

Figure 3.9. Outcomes for drops with different initial positions in an H-constriction.

Two drops with $\lambda = 1, d = 0.4$ and $Ca_m = 0.6d = 0.24$ going through a pore with an H-constriction. The lower drop starts closer to the wall and breaks, whereas the upper drop does not.

Perhaps surprisingly, a drop with a larger relative radius, $d = 0.8$, did not break for any of the entry locations and capillary numbers $(0.16 \leq \mathrm{Ca_m} \leq 0.64)$ studied for the H-constriction. As shown in Figure 3.10a, the larger drop undergoes substantial elongation as it passes through the constriction, but then it relaxes without sufficient capillary hoop stresses to cause neck pinch off. To examine if additional elongation could lead to breakup, we modified the H-constriction so that the pore length was 4.5*H* instead of 3*H*. As shown in Figure 3.10b, substantial drop deformation and elongation occurred for the longer pore, with breakup occurring after the drop exited the pore (see final image). We did not do systematic calculations with longer pores, as very high resolution and run times were required, due to drop elongation and close contact with the pore wall.

a) b)

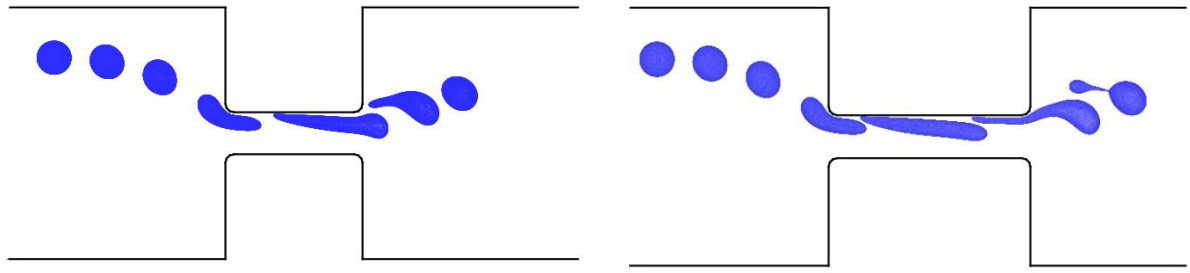

Figure 3.10. Comparison between H-constrictions with pores with different lengths.

Drop with $\lambda = 1.0$, $d = 0.8$ and $Ca_m = 0.4d = 0.32$ going through a pore with an H-constriction of length 3H, without breaking, or of (b) length 4.5H, with breaking. Large drops passing through the shorter pore do not break, while drops going through the longer pore can experience indirect breakup.

For the circular constriction, no breakup was observed for the entire parameter range investigated ($\lambda = 1, 0.2 \leq d \leq 0.8, 0.2d \leq \mathrm{Ca_m} \leq 0.6d$). As illustrated in Figure 3.11, the rounded shape of the constriction causes gentle elongation and allows the drop to return to spherical after exiting the constriction.

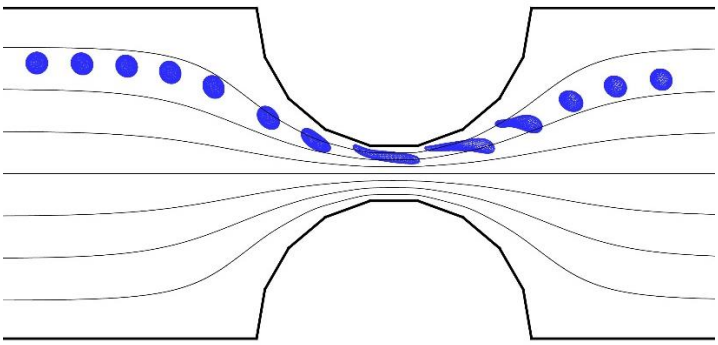

Figure 3.11. Drop going through a circular-constricted pore.

Drop with $\lambda = 1$, $d = 0.4$, and $Ca_m = 0.4d = 0.16$ going through a pore with a circular constriction without breaking.

Since little breakup was observed for the H-constriction, and none for the circular constriction, an outcomes table was not constructed for these geometries. For the H-constriction with $\lambda = 1$ and $d = 0.4$, the zone area percentages are 77% no breakup and 23% indirect breakup, for both $\mathrm{Ca_m} = 0.6d$ and $0.8d$. The corresponding inlet flux percentages are 95% for no breakup and 5% for indirect breakup. In all other cases examined for the H-constriction and circular constriction, there is > 98% no breakup (we could not definitely confirm if there is 100% no breakup, as the simulations could not be performed with initial drops nearly touching the top or bottom walls).

Since no breakup was observed in pores with a circular-constriction, we tested the effect of adding a circular-bifurcation after the constriction, as shown in Figure 3.12. This geometry represents a model for a second layer of fibers or beads in a packed bed or sintered membrane. We placed drops of $d = 0.4$ and $\mathrm{Ca_m} = 0.24$ close to the inlet reservoir walls and nearer to the centerline of the geometry, to see if we observed direct or indirect breakup. As observed in Figure 3.12, drops initially starting close to the reservoir walls have more interaction with the constriction walls and, therefore, tend to elongate more. In this case, instead of being released to another reservoir where the velocity is reduced considerably, the drops encounter a bifurcation that makes them elongate further. It appears that the lower drop in Figure 3.12 will break because of that elongation; however, the simulation could not proceed beyond the drop images shown, as the drop reached the pore exit. In contrast, drops closer to the centerline do not deform as much while going through the constriction and reach the bifurcation with a compact shape.

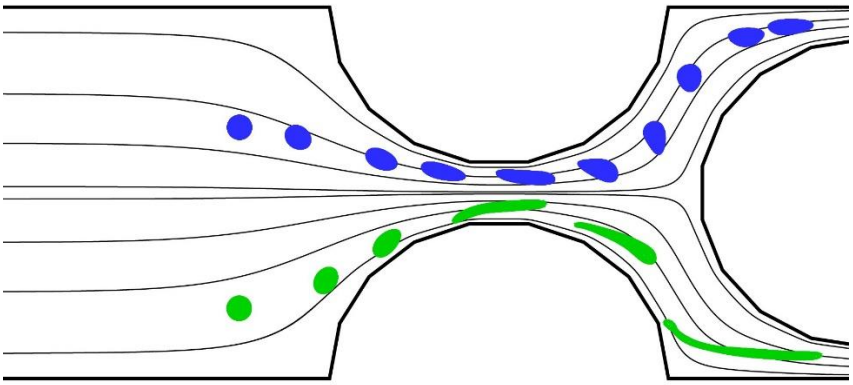

Figure 3.12. Outcomes for drops with different initial positions in an extended circular-constriction.

Drops of $\lambda = 1, d = 0.4$ and $Ca_m = 0.6d = 0.24$ with different initial positions inside a pore with an extended circular-constriction, and not breaking (upper drop) and with impending breakup due to viscous and capillary forces (lower drop).

3.3.3. Effect of the viscosity ratio

Since the Y-bifurcation results in the highest degree of drop breaking, we return to this geometry to examine the effects of viscosity ratio. Outcome maps for $d = 0.4, \mathrm{Ca_m} = 0.4d = 0.16$, and three different viscosity ratios are shown in Figure 3.13, and the corresponding inlet flux and zone area percentages are shown in Table 3.2. Both direct and indirect breakup are reduced for high-viscosity drops ($\lambda = 4$) compared to equal-viscosity drops ($\lambda = 1$). In contrast, breakup is increased slightly for low-viscosity drops ($\lambda = 0.25$), indicating that water-in-oil emulsions may more easily break during filtration. This latter finding is perhaps surprising, in that drops with $\lambda \approx 1$ most easily break in unconfined flows (Stone et al., 1986). However, for asymmetric flows in T-junctions, we previously found a large reduction in breaking of high-viscosity drops but little change for low-viscosity drops compared to $\lambda = 1$.

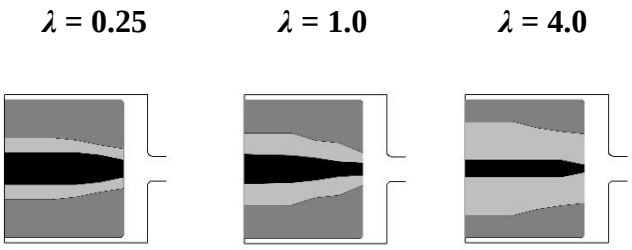

Figure 3.13. Outcome maps for drops with different viscosity ratios in a pore with a Y-bifurcation.

Outcome maps for drops with relative diameter $d = 0.4$, capillary number $Ca_m = 0.4d = 0.16$, and viscosity ratios between the drop and the bulk fluid of λ = 0.25, 1.0 and 4.0. Light gray corresponds to the non-breakup zone, black corresponds to the direct breakup zone and dark gray corresponds to the indirect breakup zone. Drops with smaller viscosity than the carrier fluid are more likely to break while going through the pore.

Table 3.2. Outcome percentages for drops with different viscosity ratios in a pore with a Y-bifurcation.

	% no breakup		**% direct breakup**		**% indirect breakup**	
	Inlet flux	**Zone area**	**Inlet flux**	**Total area**	**Inlet flux**	**Zone area**
λ = 0.25	27%	19%	32%	21%	41%	60%
λ = 1.0	37%	27 %	30%	17 %	33%	56 %
λ = 4.0	65%	49%	18%	12%	17%	39%

Percentages of each outcome for drops with $d = 0.4$, $Ca_m = 0.d = 0.16$, and λ = 0.25, 1.0 and 4.0 in a narrow pore with a Y-bifurcation.

3.3.4. Drop size distribution

Of particular interest in premix membrane emulsification is the size distribution of drops after passing through the pores. In the current work, the droplet sizes exiting a single pore depend

not only on the pore geometry and properties of the entering drop but also on the location across the channel at which the drop enters.

Figure 3.14 shows the volume (V_L) of the larger of two daughter drops relative to the volume of the parent drop (V_0) as a function of the vertical position (y_0, dimensionless distance from the pore centerplane) at which the parent drop enters. A Y-bifurcation is used, as it yields both direct and indirect breakup. The viscosity ratio and capillary number are fixed at $\lambda = 1$ and $Ca = 0.4$, respectively, but three parent drop diameters are considered: $d_0 = 0.2$, 0.4, and 0.8. At $y_0 = 0$ (parent drop entering along the centerplane), $V_L/V_0 = 0.5$ due to symmetry, as the parent drop breaks in half upon encountering the Y-bifurcation. As y_0 increases, direct breakup continues to occur, but it is asymmetric and so $V_L/V_0 > 0.5$. The volume partition to the larger daughter drop increases monotonically with increasing y_0, until either there is no longer breakup or the mode of breakup switches from direct to indirect. However, the three parent drop sizes examined exhibit three different behaviors.

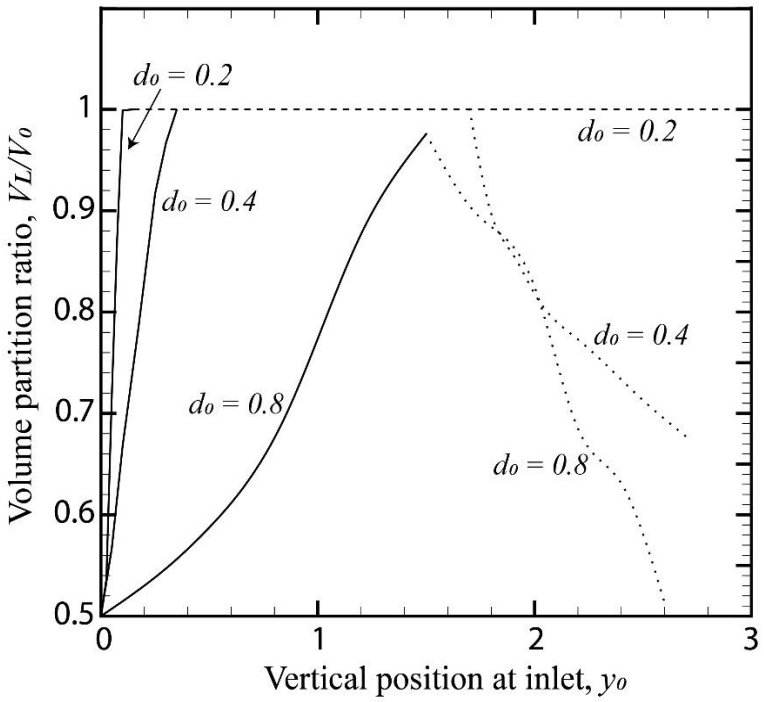

Figure 3.14. Volume of the larger daughter drop versus entry position.

Volume of the larger daughter drop, normalized by the volume of the parent drop, versus entry position, in a pore with a Y-bifurcation. The conditions are Ca = 0.4, λ = 1, and d_0 = 0.2, 0.4, and 0.8. The solid curves represent direct breakup, the dashed lines (V_L/V_0 = 1) are for no breakup, and the dotted curves represent indirect breakup.

For the smallest parent drop ($d_0 = 0.2$), direct breakup only occurs for a narrow range of entrance positions, $|y_0| \leq 0.10$, near the pore centerplane. For $|y_0| > 0.10$, the small parent drop proceeds into one of the branches of the Y-bifurcation without breaking; indirect breakup is not observed. For d_0 = 0.4, direct breakup occurs for a somewhat larger range of entrance positions, $|y_0| \leq 0.35$. Then, there is no breakup for $0.35 < |y_0| \leq 1.70$. However, for $|y_0| > 1.70$, the parent drop enters the pore constriction in close contact with a pore wall and so elongates and undergoes indirect breakup – similar to that shown in figure 5c. Finally, the largest drop ($d_0 = 0.8$) undergoes

direct breakup for a larger range of entry positions, $|y_0| \leq 1.50$, and then transitions to indirect breakup for $|y_0| > 1.50$; the outcome of no breakup is not observed for the larger drop.

From knowledge of the daughter drop sizes as a function of the inlet position, the post-pore droplet size distribution can be predicted, for a given distribution of drop locations across the pore entrance. The results are displayed as histograms based on the probability density function, $P(d)$, defined such that $P(d)\Delta d$ is the fraction of drops by volume that have diameters in the range of $d - \Delta d/2$ to $d + \Delta d/2$. Assuming parabolic flow at the entrance and a uniform distribution of inlet positions $0 \leq |y_0| < 3 - d_0/2$, where d_0 is the parent drop diameter, we have

$$P(d_i)\Delta d_i = \int_{y_i}^{y_{i+1}} [1 - (y/3)^2]\, \emptyset(y)\, dy \,/\, \int_0^{3-d_0/2} [1 - (y/3)^2]\, dy, \tag{3.6}$$

where $\emptyset(y) = V_L(y)/V_0$ is the volume partition fraction of the larger daughter drops, $\Delta d_i = d_{i+1} - d_i$, and y_{i+1} and y_i are the inlet positions that yield $\emptyset(y_i) = (d_i/d_0)^3$ and $\emptyset(y_{i+1}) = (d_{i+1}/d_0)^3$, respectively. The denominator of (3.6) is the same as the denominator of (3.5). Moreover, (3.6) only accounts for the larger daughter drops ($\emptyset \geq 0.5$), and so a similar accounting must be made for the smaller daughter drops, for which $V_S(y)/V_0 = 1 - \emptyset(y) \leq 0.5$. To determine the size distribution of drops after passing through a pore, Simpson's rule was used to numerically evaluate the numerator of (3.6), with $\emptyset(y)$ evaluated from Figure 14 or similar plots, based on numerous simulations of the outcome for a drop starting at different positions y at the pore entrance.

Figure 3.15 shows example results for the Y-bifurcation for $\mathrm{Ca} = 0.4$ and $\lambda = 1$. This single figure has three histograms of pore-exit droplet size distribution, starting with inlet drop sizes of $d_0 = 0.2$, 0.4, and 0.8 (left to right). The largest parent drops ($d_0 = 0.8$) break into a broad distribution of daughter drops, with $0.4 \lesssim d \lesssim 0.8$. Even though all drops break for this case (see Table 3.1, and Figures 3.7 and 3.14), there are some large daughter drops in the largest bin, $0.75 < d \leq 0.80$, due to highly asymmetric breakup; the smaller daughter drops are in the smaller bins.

In contrast, the medium-sized parent drops ($d_0 = 0.4$) experience breakup only 59% of the time (see Table 3.1), and have a more narrow distribution of daughter drops. Finally, the smallest parent drops ($d_0 = 0.2$), experience very little direct breakup and no indirect breakup, with over 99% of the drops by volume in the pore exit remaining in the largest bin.

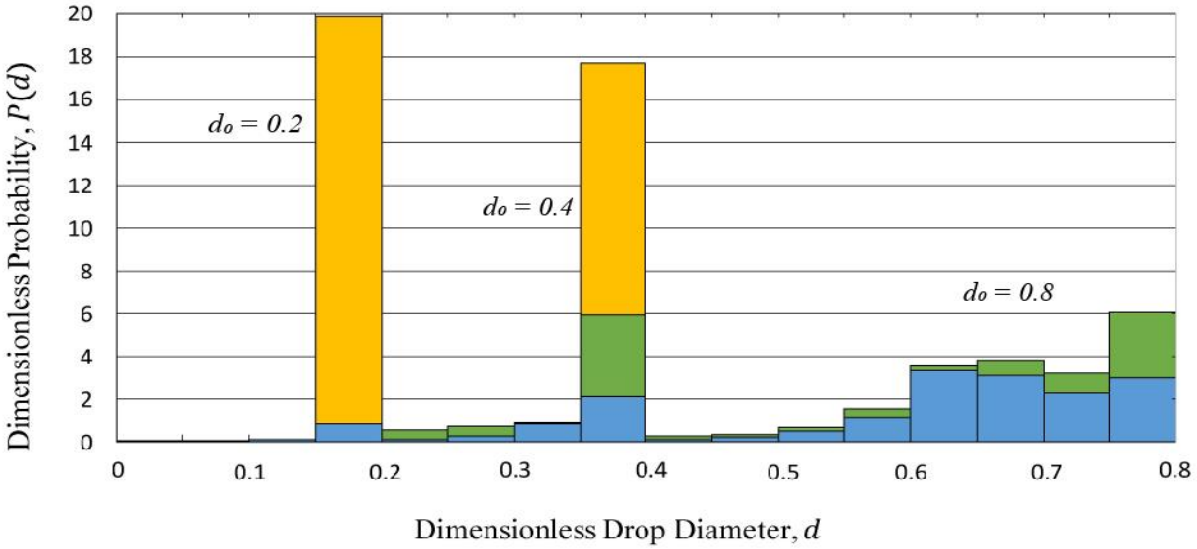

Figure 3.15. Droplet size distribution, Ca = 0.4.

Droplet size distribution by volume after exiting a pore with a Y-bifurcation for inlet drops having $\lambda = 1$, $Ca = 0.4$, and $d_0 = 0.2$, 0.4, and 0.8 (left to right). Blue (black for print) represents direct breakup, green (dark gray for print) indirect breakup, and orange (light gray for print) no breakup.

Similar results are shown in Figure 3.16 for $\mathrm{Ca} = 0.8$. There is generally more drop breakup at higher capillary numbers, due to greater deformation. Moreover, in some cases the parent drop broke into three (or even four – see Figure 3.17) daughter drops, and so the analysis was modified to account for all of the daughter drops. These results suggest a thought experiment (which could be verified by simulation, given enough time and computational resources). Suppose we started with a distribution of large drops, which could be broad or narrow. After each drop passes through

one pore, many or all would have broken, and the resulting distribution would have shifted toward smaller drops and likely broadened. Then, after that distribution passes through another set of pores, the larger drops break but the smaller ones that are below a critical size do not break. Eventually, after passing through many pores in one membrane or porous medium and/or with multiple passes through the membrane or porous medium, the distribution will have shifted to a narrow size distribution clustered around the critical size (below which breakup is negligible), plus some smaller drops (which may be many in number but small in volume percent) that represent small daughter drops from the asymmetric pinch-off process. This result is at the heart of premix emulsification, and has been observed experimentally (Kaade et al., 2020; Nazir et al., 2013; G. T. Vladisavljević et al., 2004).

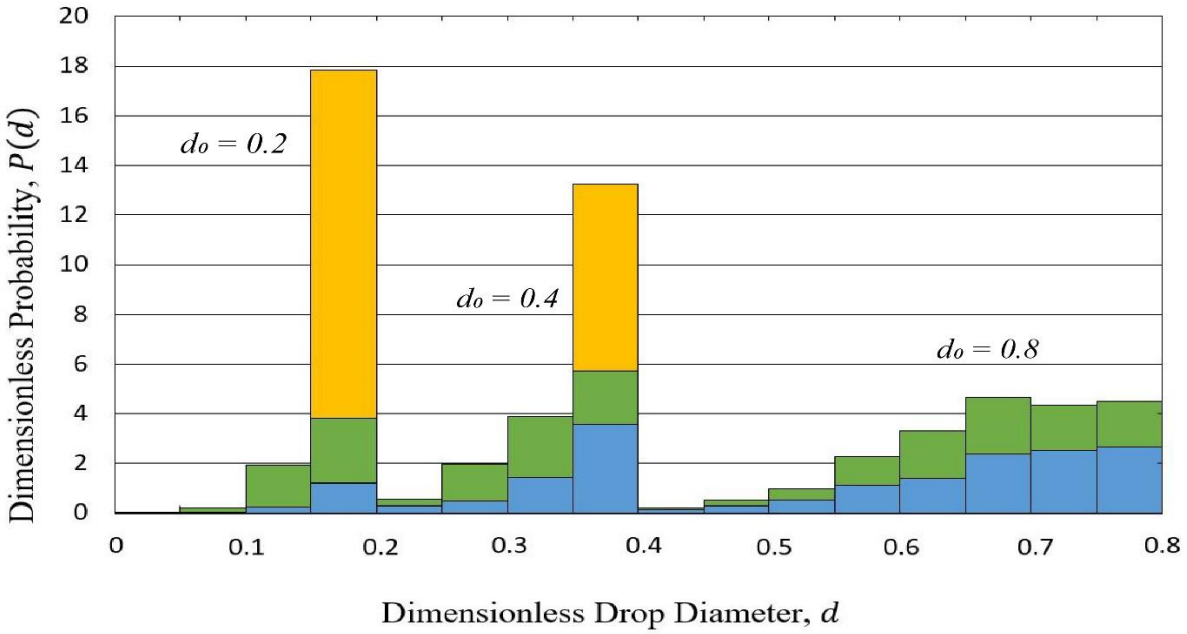

Figure 3.16. Droplet size distribution, Ca = 0.8.

Droplet size distribution by volume after exiting a pore with a Y-bifurcation for inlet drops having λ = 1, $Ca = 0.8$, and d_0 = 0.2, 0.4, and 0.8. Blue (black for print) represents direct breakup, green (dark gray for print) indirect breakup, and orange (light gray for print) no breakup.

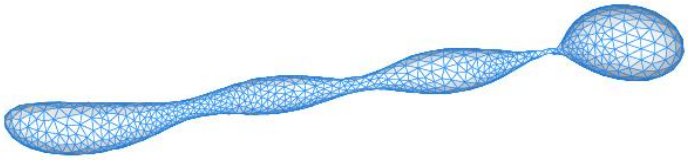

Figure 3.17. Drop breaking in multiple droplets.

Droplet with λ = 1, $Ca = 0.8$, and d_0 = 0.4 just prior to elongational breakup into four daughter drops when passing through a pore with a Y-bifurcation.

3.4. Concluding remarks

We used a moving-frame boundary-integral algorithm to predict whether a small drop would break or not when passing through a narrow pore, depending on its initial position, fluid properties, and the pore geometry. We observed three different scenarios: when the drop goes through the pore without breaking, when it breaks due to encountering a bifurcation/corner (direct breakup), and when it breaks due to elongation (indirect breakup).

For the Y-bifurcation geometry, drops with initial positions close to the center of the pore break due to the interaction with the corner of the bifurcation, regardless of the physical properties of the drop. This behavior is only observed in this geometry, since in the other geometries examined the drops do not encounter a bifurcation with a sharp corner. Relatively large drops with $d = 0.8$ (undeformed drop diameter of 80% of the channel height) always break in narrow pores with a Y-bifurcation, for all capillary numbers examined. When varying the viscosity ratio between the drop and the bulk fluid, a higher fraction of breakup events occurs with lower viscosity ratios, such as characteristic of water-in-oil emulsions

Direct breakup was not observed for droplets in the H and circular constricted-pore networks, because there are no sharp corners or physical obstacles and the lubrication layer formed

between drop and the pore walls that prevents drop-wall contact. The lubrication effects were fully resolved in the boundary-integral algorithm, with discretization of both the drop surface and pore walls at high resolution. However, indirect breakup (due to drop stretching and capillary pinch off) takes place in pores with an H-constriction when the drops are large enough to suffer large deformation but small enough (e.g, $d = 0.4$) that they elongate inside the pore and then undergo capillary pinch off at the pore exit. For the cases studied, no breakup was observed in the circular-constriction, because of the smooth nature of this kind of pore, which allows the drop deform gradually.

From a practical viewpoint, pore networks with bifurcations (such as in the Y-bifurcation model) provide for greater breakup of drops smaller than the minimum pore size, compared to pores with constrictions but not bifurcations or branches. A perhaps puzzling result is the lack of breakup predicted for the circular constriction, whereas experimental work (Kaade et al., 2020; Nazir et al., 2013) has achieved substantial reduction in drop sizes using packed beds of small spheres. The difference may be due to the 2D pore geometry of the model versus 3D bed in the experiments – indeed, Zinchenko & Davis (2013) demonstrated drop breakup in boundary-integral simulations of emulsion flow through a 3D bed of spheres. Additionally, our preliminary test indicates that multiple layers of circular constrictions may induce breakup when a single layer will not.

The post-pore drop size distributions show that large drops break into a broad distribution of daughter drop sizes. However, drops below a critical size show essentially no breakup. Thus, by passing an emulsion with large drops through many pores, or through a membrane or a packed bed multiple times, the expected result is a narrow distribution of small drops near the critical size. Indeed premix emulsification experiments have demonstrated this outcome (Nazir et al., 2013;

Vladisavljević et al., 2004). While the current algorithm and computational power are not sufficient to fully simulate emulsification and multiple passes through realistic membranes and other complex porous geometries, it is hoped that our single-pore simulations will motivate future studies in this area. Moreover, the current simulation method can identify the minimum drop size, below which further breakup is negligible, and thus assist with the design of premix emulsification to achieve a desired drop size; for example, Figure 15 shows negligible breakup of drops with $d = 0.2$ and Ca = 0.4, whereas Figure 16 shows modest breakup of drops of this size for Ca = 0.8, and so there is a smaller critical drop size for the higher capillary number or flow rate.

Chapter IV

Boundary-integral study of a viscous drop in finite-depth channels

Abstract

We developed a new, moving-frame boundary-integral algorithm to simulate the dynamics of a drop moving in a finite-depth channel. The drop size is comparable to the channel height, which is of the same order of magnitude as the channel depth. Introducing a third dimension (compared to the previous chapters of this thesis) carries computational challenges that are overcome through the introduction of an adaptation of the Monte-Carlo method to perform the channel meshing, and using Boussinesq analytical solution for the undisturbed flow in rectangular channels to calculate the flow velocity profile at the entrance(s) and exit(s) of the channel. This approach was then used to simulate the undisturbed flow field throughout a complex channel and subsequently applied on the boundaries of the moving frame around the drop to determine its motion and deformation. The effect of the channel depth on the drop behavior was studied in different scenarios. When placed in long, straight channels, smaller drops travelled faster than larger drops (which are slowed by viscous stresses when in close contact with the walls). Drops with larger capillary numbers achieved higher velocities due to their more elongated steady-state shape, reducing the friction drag coefficient exerted by the carrier fluid and increasing the distance from the drop interface to the channel walls. When the channel has a bifurcation, the depth value

can make the problem outcome change (from breakup to no breakup) or, in cases of breakup, the size of the daughter droplets.

4.1. Prior work and context for current work

Due to its multiple applications in droplet-based microfluidics, the investigation of drop motion in three-dimensional channels has recently raised attention both experimentally and computationally. In this Chapter, a novel algorithm to describe the motion of viscous drops in finite-depth channels is presented. The need for creating a new algorithm arises with the necessity of analysis and design of microfluidic systems as close to reality as possible.

In the experimental field, Ménétrier-Deremble & Tabeling (2006) studied the drop breakup in microfluidic junctions of different angles. They found a critical penetration length into the side channel for which the drop breaks. Its value is independent on the flow conditions and fluid properties, as it primarily depends on the channel geometry. Vanapalli et al. (2009) measured the excess of pressure drop due to a single droplet travelling through a confined rectangular channel. The effects of the droplet size, capillary number and viscosity ratio on the hydrodynamic resistance of the droplet were determined. They found out that, for small droplets (droplet length/channel width < 4), the pressure drop is independent of the drop size and capillary number and the viscosity ratio has a small effect. For large drops (droplet length/channel width > 4), the hydrodynamic resistance is strongly influenced by the viscosity ratio between the two fluids, as well as the drop size. Jakiela et al. (2011) presented experimental results of the motion of a single droplet going through channels of square cross-sections. They showed how the droplet dynamics is affected by several parameters, especially by the capillary number. They found out that, when a drop is less viscous than the continuous phase, the droplet and the main fluid travel at similar speeds, while

when the droplet is more viscous than the bulk fluid, the drop moves more slowly. They highlighted the necessity of designing an analytical model to characterize the drop motion in rectangular channels. Ma et al. (2014) studied the flow topology in droplets moving in a rectangular microchannel. To study the effects of the capillary number, drop size and viscosity ratio, they worked with different water/oil (W/O) mixtures. They found that the viscosity ratio between the drop and the carrier was the dominant factor in the topology of the flow. The capillary number and the drop geometry had an effect on the internal velocity magnitude and on the recirculation, but not on the intrinsic flow topology. Wang et al. (2019) experimentally studied the dynamics of drop breakup in an asymmetric Y-bifurcation. They analyzed the effects of the droplet size and capillary number on the evolution of the neck thickness and determined a critical value for which droplets break. Li et al. (2020) experimentally studied the internal flow field of drops moving in rectangular channels. They were able to determine the effects of the volumetric flow, droplet spacing, size, viscosity ratio and the depth-width ratio on the flow. Almost all these experimental studies highlighted the importance of developing a model that can predict drop behavior, and can be useful in order to validate the model.

Some authors have performed computational analysis of drop behavior in rectangular microchannels using the Volume of Fluid (VOF) method. Sarrazin et al. (2008) used a finite-volume/front capturing method to simulate the hydrodynamics inside drops in rectangular channels. They studied the droplet deformation and the velocity fields inside the drop and in the bulk fluid. The drop capillary number significantly influenced the external flow hydrodynamics and, together with the channel size, had great influence on the drop internal hydrodynamics as well. Raj et al. (2010) used the VOF method to simulate the dynamics of a water droplet in silicon oil. They studied the effect of the flow rate, channel size and viscosity ratio on the drop shape and

length and compared it with previous literature measurements. They pointed out the necessity of investigating the effects of grid refinement near the channel walls, surface wettability, and roughness on the boundary layer. Reddy Cherlo et al. (2010) used the VOF method using the commercial package FLUENT to study the flow behavior of a liquid-liquid system in a microreactor (microchannels with a rectangular cross-section) and compared it to experimental results. They found shape differences between the experimental results, and the results obtained with the simulations because the package did not describe correctly the effect of the surface tension. Yong et al. (2011) used a Lattice Boltzmann (LB) method to describe the dynamics of two liquid-liquid phase flows in microchannels. They studied different regimes, finding, in general, good agreement with experimental data. However, one of the regimes could not be solved due to limited grid resolution. Hoang et al. (2013) completed an analysis of the performance of the Volume of Fluid (VOF) method implemented in OpenFOAM, modeling the motion and breakup of confined drops and bubbles in straight channels and T-junctions. Although their results have good agreement with the experiments, some differences were observed, so the accuracy of the simulations needs to be improved. Rao & Wong (2018) also studied the motion of a long drop in a rectangular microchannel. They focused on the carrier-liquid pressure-gradient calculation and the dependence of the fluid velocity on this parameter. The VOF method is well established. However, it presents some issues for the accurate calculation of curvature and surface tension forces, and some error propagation can make simulations not physically accurate. Another inconvenience is that the computational cost may be high for large domains.

Other methods have been used to describe the drop motion in different channels. For example, Carroll & Gupta (2014) used a front-tracking method to study the motion of neutrally buoyant droplets in circular channels at finite Reynolds numbers and moderate capillary numbers.

Their results agree well with previous studies in the Stokes flow regime. For moderate-sized drops, a non-monotonic trend in the drop velocity was observed when increasing the Reynolds number, while for large drops the inertial effects further elongated the drop and the non-monotonic trend was not observed. For small drops, only an initial decrease of the velocity was observed. Although the front-tracking method is useful to describe the motion of drops in certain scenarios, it is hard to apply in surfaces with topological changes. So, a more general method that can deal with drop breakup and mesh refinements, for example, seems to be more appropriate to use in the study of droplet dynamics.

The boundary-integral (BI) method has also been used to characterize the dynamics of confined viscous droplets. Hodges et al. (2004) investigated the effect of viscosity on the motion of a drop going through a cylindrical tube. They focused on the study of the formation of a thin film (lubrication layer) between the drop and the channel wall, and studied the effect of the viscosity and the capillary number on the film thickness. Sarrazin et al. (2006) studied, numerically and experimentally, droplet hydrodynamics in rectangular microchannels. The results obtained with their interface-capturing numerical technique and with microparticle image velocimetry measurements are in good agreement, and the shape of the deformed droplet was well reproduced. Lac & Sherwood (2009) also studied the deformation of a drop moving along the axis of a circular tube. They studied the effect of the capillary number, drop size and viscosity ratio on the drop motion and the influence they had on each other. Guido & Preziosi (2010) focused on the study of the motion of a droplet moving in cylindrical and rectangular channels containing a Poiseulle flow using boundary-integral methods. They highlighted the relevance of these kind of systems in the industry and their broad range of promising applications and reported the main fluid dynamical aspects related to this kind of geometries. The BI method has been successfully used to accurately

determine the drop motion in simple three-dimensional geometries, and we believe it can be used in more complex ones, if the moving-frame method is adapted to three-dimensional channels.

In this work, a new method is developed to describe the motion of viscous drops in finite-depth channels, building on prior work for infinite-depth channels (Navarro et al., 2020). A new discretization method - partially based on the Monte Carlo method – is introduced, followed by a triangular tessellation to create the mesh for the front and back channel walls, which are used as boundaries in the boundary-integral algorithm to calculate the flow inside the geometry. Then the analytical solution of Boussinesq (1868) for undisturbed flow in rectangular channels is used at the entrances and exits of the channel and on the moving-frame (MF) that servers as the computational boundary surrounding the moving drop at each time step. The algorithm is used to study drop dynamics in a long, straight channel and in a channel with a Y-bifurcation. In the long, straight channel, smaller drops move faster than larger drops, which, because of their proximity to the channel walls, are slowed down by the hydrodynamic forces exerted on them. Drops with higher capillary numbers attained higher velocities due to their steady-state shapes: viscous forces make them more deformable and, therefore, more elongated so the drag coefficient exerted by the carrier fluid is smaller and the gap between their surface and the channels walls is larger.

4.2. Theoretical development

Part of this work was performed jointly with a former student of the group, A. Maristany. More details of his contributions can be found in his Master thesis (Maristany, 2019).

4.2.1. Problem definition

The objective of this chapter is to describe the motion of a viscous droplet in three-dimensional channels. The droplet has viscosity μ_d and density ρ_d, while the surrounding fluid

has viscosity μ_e and density ρ_e. We work at low Reynolds number regime, $\mathrm{Re} = \rho_e U H/\mu_e \ll 1$, (where *U* is the average fluid velocity and *H* is the channel height) so viscous forces dominate and the linearized Stokes equations govern the motion. It is assumed that the drop is neutrally buoyant, so $\rho_d \approx \rho_e$. The effects of adding a third dimension to the channels on the drop dynamics are studied together with a parametric analysis of the effects of the capillary number $\mathrm{Ca} = \mu_e U/\sigma$, where σ is the interfacial tension; drop relative radius $R = a/H$; and viscosity ratio between the fluids $\lambda = \mu_d/\mu_e$.

4.2.2. Channel meshing

First, it is necessary to define the channel geometry and depth. Figure 4.1 shows a three-dimensional channel with a Y-bifurcation:

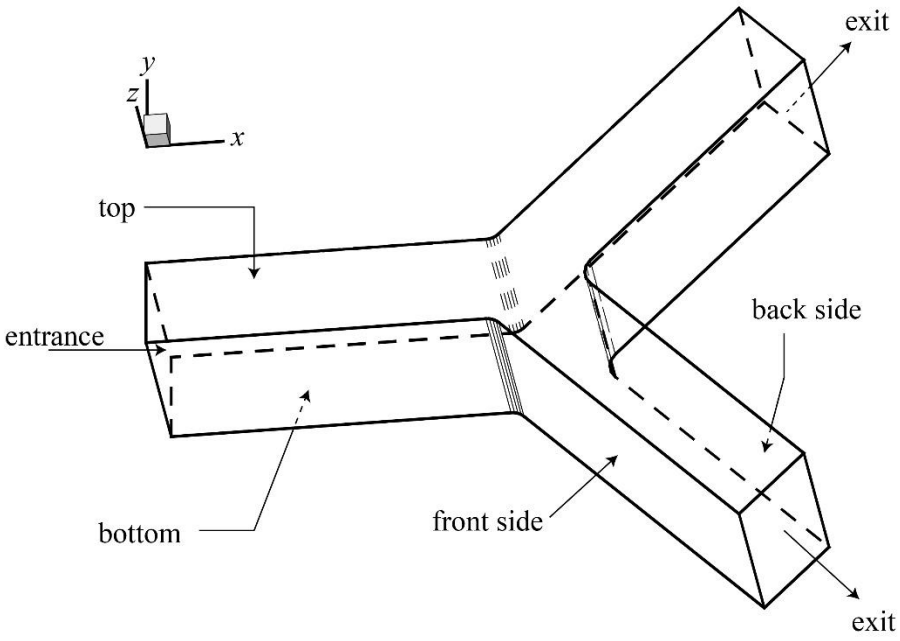

Figure 4.1. Three-dimensional view of a channel with a Y-bifurcation.

Among all the panels that form the channel only two are complex, the ones in the xy-plane (top and bottom panels); the rest are rectangles of different proportions, which are discretized using Cartesian grids. To discretize the top and bottom panels, it is necessary to set the number of points that will be part of a panel's mesh. Then, the area of the domain (panel) is calculated. After that, a statistically uniform distribution of points (or disks of zero radius) is generated on the corners of the domain and randomly within the domain (figure 4.2a) using an original algorithm partially based on the Monte Carlo method (Metropolis & Ulam, 1949), and then the points are moved to their final positions in the domain (figure 4.2b). To do so, the disks randomly move one by one while their radius increases gradually until reaching a target value. These disks cannot overlap each other. To reduce computational costs, when the disks expand, only the surrounding circles (based on a Cartesian division of the domain (Maciejko et al., 1995)), are taken into account.

a) b)

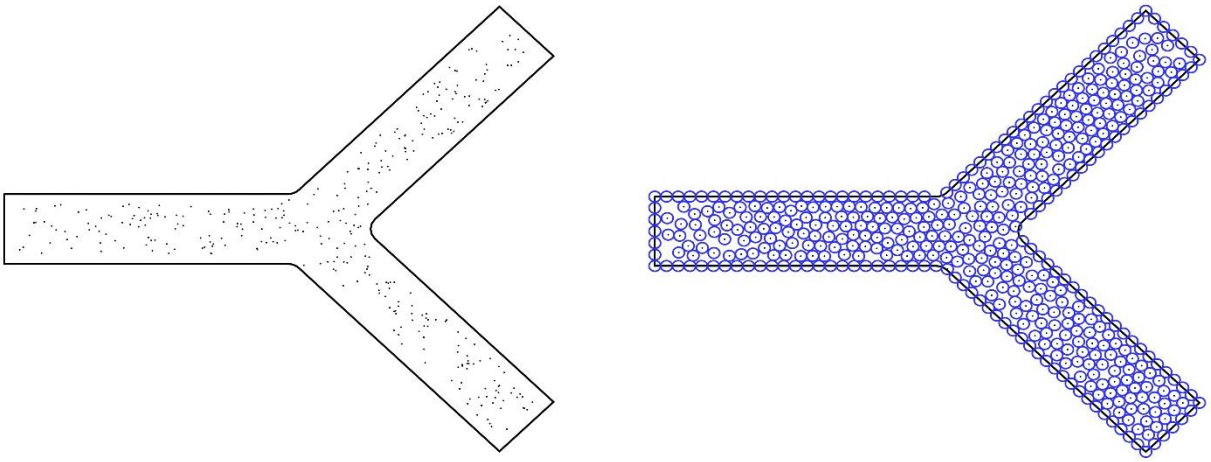

Figure 4.2. Channel meshing steps.

Representation of the 500 points a) randomly generated on the top and bottom panels of the channel and b) statistically uniform to create the panels mesh.

Then, the panels need to be tessellated into triangles. To do that, the centers of the disks are converted into triangle vertices using a 2D adaptation of the 3D Voronoi tessellation algorithm (Tanemura et al., 1983). The triangles must meet two criteria to not to be discarded from the mesh: the first one is related to the quality of the triangles, so the ratio between triangle area and perimeter squared is checked to not to have very thin triangles. The second criterion is that the centroid of the mesh triangles must lie inside the domain boundaries to not to be discarded (particularly useful for concave corners). Figure 4.3 shows the mesh obtained for the top and bottom panels of a channel with a Y-bifurcation:

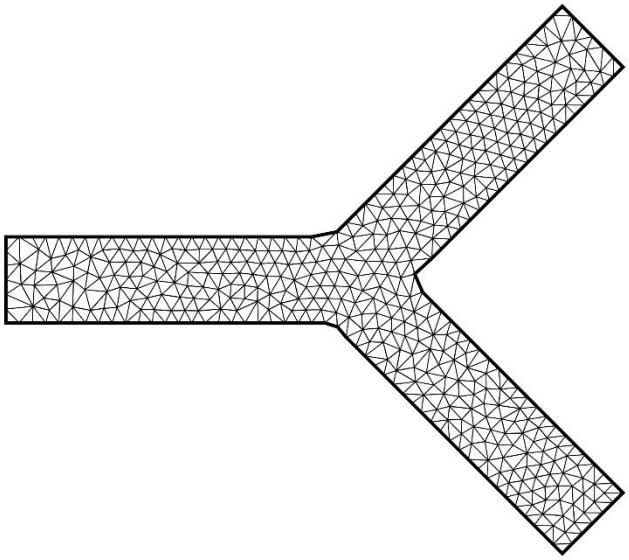

Figure 4.3. Triangular mesh of the top and bottom panels of a channel with a Y-bifurcation.

4.2.3. Velocity calculation in the inlets and outlets of the channel

To calculate the velocity at the inlets and outlets of the channel, the Boussinesq solution for a flow inside a long, rectangular channel (Joseph Boussinesq, 1868) was used:

$$\boldsymbol{u}(y,z) = \left[\frac{G}{2\mu}y(h-y) - \frac{4Gh^2}{\mu\pi^3}\sum_{n=1}^{\infty}\frac{1}{(2n-1)^3}\frac{sinh(\beta_n z)+sinh(\beta_n(l-z))}{sinh(\beta_n l)}sin(\beta_n y)\right]\boldsymbol{n}, \quad (4.1)$$

where $\beta_n = (2n-1)\pi/h$, μ is the dynamic viscosity of the fluid, $G = -dp/dx$ is the pressure gradient and $u(y,z)$ is the velocity along the channel (parallel to the bounding walls in the direction $\boldsymbol{n}$ normal to the entrance or exit) at a point with coordinates y and z in the cross-section, h is the channel height and l is the channel length.

The pressure gradient G is calculated using Bousinessq flow expression, where the flow Q is set equal to a certain value so **G** can be calculated:

$$Q = \frac{Gh^3 l}{12\mu} - \frac{16Gh^4}{\pi^5\mu}\sum_{n=1}^{\infty}\frac{1}{(2n-1)^5}\frac{cosh(\beta_n l)-1}{sinh(\beta_n l)} \quad . \quad (4.2)$$

4.2.4. Velocity calculation inside the channel

Like in the previous chapters of this thesis, the undisturbed velocity of the fluid $\boldsymbol{u}_\infty$ inside the channel is calculated in the form of a double-layer boundary-integral equation*:*

$$\boldsymbol{u}_\infty(\boldsymbol{y}) = 2\int_{S_{TOT}} \boldsymbol{q}_\infty(\boldsymbol{x})\cdot\boldsymbol{\tau}^{\mathbf{3D}}(\boldsymbol{r})\cdot\boldsymbol{n}(\boldsymbol{x})ds_x \quad , \quad (4.3)$$

where $\boldsymbol{r} = \boldsymbol{x} - \boldsymbol{y}$, S_{TOT} stands for the sum of all boundary-surfaces, and $\boldsymbol{\tau}(\boldsymbol{r})$ *is* the 3D fundamental stresslet, defined as

$$\boldsymbol{\tau}(\boldsymbol{r}) = \frac{3}{4\pi}\frac{\boldsymbol{rrr}}{r^5} \ , \quad r = |\boldsymbol{r}|. \quad (4.4)$$

Desingularizing (4.3), for a point $\boldsymbol{y}$ inside the channel we obtain:

$$\boldsymbol{u}_\infty(\boldsymbol{y}) = 2\int_{S_{TOT}}[\boldsymbol{q}_\infty(\boldsymbol{x}) - \boldsymbol{q}_\infty(\boldsymbol{x_o})]\cdot\boldsymbol{\tau}(\boldsymbol{x}-\boldsymbol{y})\cdot\boldsymbol{n}(\boldsymbol{x})ds_x + \mathbf{2}\boldsymbol{q}_\infty(\boldsymbol{x_o})\int_{S_{TOT}}\boldsymbol{\tau}(\boldsymbol{x}-\boldsymbol{y})\cdot$$

$$\boldsymbol{n}(\boldsymbol{x})ds_x \ , \quad (4.5)$$

where $\boldsymbol{x_o}$ is the boundary point nearest to $\boldsymbol{y}$. Then, taking the limiting value of the first integral at $\boldsymbol{y}\to\boldsymbol{x_o}$, the potential density $\boldsymbol{q}_\infty(\boldsymbol{y})$ becomes*:*

$$\boldsymbol{q}_{\infty}(\boldsymbol{y}) = \boldsymbol{u^b}(\boldsymbol{y}) - 2\int_{S_{TOT}} \boldsymbol{q}_{\infty}(\boldsymbol{x}) \cdot \boldsymbol{\tau}(\boldsymbol{x}-\boldsymbol{y}) \cdot \boldsymbol{n}(\boldsymbol{x}) ds_x \ . \tag{4.6}$$

In contrast to the infinite-depth solution, only partial deflation is used herein (without the rigid-body projection term), which still provides convergent iterations. Thus, adding an additional term to ensure zero total flux through the boundary, the prescribed velocity on the boundaries $\boldsymbol{u^b}$ becomes:

$$\boldsymbol{u^b}(\boldsymbol{y}) = \widetilde{\boldsymbol{q}}_{\infty}(\boldsymbol{y}) + 2\int_{S_{TOT}} \widetilde{\boldsymbol{q}}_{\infty}(\boldsymbol{x}) \cdot \boldsymbol{\tau}(\boldsymbol{x}-\boldsymbol{y}) \cdot \boldsymbol{n}(\boldsymbol{x}) ds_x - \frac{\boldsymbol{n(y)}}{S}\int_{S_{TOT}} \widetilde{\boldsymbol{q}}_{\infty}(\boldsymbol{x}) \cdot \boldsymbol{n}(\boldsymbol{x}) ds_x \ . \tag{4.7}$$

To avoid severe convergence difficulties due to the presence of sharp corners, equation (4.7) is solved using a biconjugate-gradient method (Zinchenko et al., 2012).

4.2.5. Velocity calculation of the 3D drop

To calculate the velocity $\boldsymbol{u}(\boldsymbol{y})$ of the drop at each of its surface nodes, $\boldsymbol{u}_{\infty}(\boldsymbol{y})$ is applied on the boundaries of the moving frame:

$$\boldsymbol{u}(\boldsymbol{y}) = \frac{2}{(\lambda+1)}\left[\boldsymbol{u}_{\infty}(\boldsymbol{y}) + F(\boldsymbol{y}) + 2\int_{S_{\infty}} \boldsymbol{q}(\boldsymbol{x}) \cdot \boldsymbol{\tau}(\boldsymbol{x}-\boldsymbol{y}) \cdot \boldsymbol{n}(\boldsymbol{x}) dS_x\right] + \frac{2(\lambda-1)}{(\lambda+1)}\int_{Sd} \boldsymbol{u}(\boldsymbol{x}) \cdot \boldsymbol{\tau}(\boldsymbol{x}-\boldsymbol{y}) \cdot \boldsymbol{n}(\boldsymbol{y}) dS_x, \tag{4.8}$$

where S_{∞} is the moving-frame surface, S_d is the drop surface, and $\lambda = \mu_d/\mu_e$ is the ratio between the droplet and the fluid viscosities. The boundary-integral equation for the density function is:

$$\boldsymbol{q}(\boldsymbol{y}) = -\boldsymbol{F}(\boldsymbol{y}) - (\lambda-1)\int_{Sd} \boldsymbol{u}(\boldsymbol{x}) \cdot \boldsymbol{\tau}(\boldsymbol{x}-\boldsymbol{y}) \cdot \boldsymbol{n}(\boldsymbol{x}) dSx - 2\int_{S_{\infty}} \boldsymbol{q}(\boldsymbol{x}) \cdot \boldsymbol{\tau}(\boldsymbol{x}-\boldsymbol{y}) \cdot \boldsymbol{n}(\boldsymbol{x})\, dSx - \frac{\boldsymbol{n(y)}}{S_{\infty}}\int_{S_{\infty}} \boldsymbol{q}(\boldsymbol{x}) \cdot \boldsymbol{n}(\boldsymbol{x}) dS_x \ , \tag{4.9}$$

where $\boldsymbol{F}(\boldsymbol{y}) = \frac{1}{\mu_e}\int_{Sb} \boldsymbol{G}(\boldsymbol{x}-\boldsymbol{y}) \cdot 2\sigma k(\boldsymbol{x}) \cdot \boldsymbol{n}(\boldsymbol{x}) dSx$, $\boldsymbol{G}$ is the free-space Green tensor defined as $\boldsymbol{G} = (\boldsymbol{I}/r + \boldsymbol{rr}/r^3)/8\pi$, which is a velocity field associated with a point force acting at $\boldsymbol{y}$, $\boldsymbol{\tau}(\boldsymbol{x}-\boldsymbol{y}) = (3/4\pi)\boldsymbol{rrr}/r^5$ is the fundamental stresslet, and $k(\boldsymbol{x})$ is the curvature of the drop surface. Further discussion of the method and its convergence can be found in Navarro et al. (2020).

4.3. Results and discussion

4.3.1. Effect of the channel depth on drop motion

To study the effect of the channel depth, we compared the value of the steady-state drop velocity (Griggs et al., 2007), defined as the average of $\boldsymbol{u}$ over the drop volume, obtained for a drop after travelling distance of $10H$ in a long, straight channel, for various relative depths (D/H), to that obtained using the infinite-depth BI algorithm, ($D/H \rightarrow \infty$):

$$\boldsymbol{U_d} = \frac{1}{V}\int_V \boldsymbol{u}(\boldsymbol{x})dV = \frac{1}{V}\int_S [\boldsymbol{u}(\boldsymbol{x}) \cdot \boldsymbol{n}(\boldsymbol{x})](\boldsymbol{x} - \boldsymbol{x_c})dS_x \,, \tag{4.10}$$

where $\boldsymbol{x_c}$ is the drop centroid. In the simulations, the dimensionless volumetric flow rate was set equal to the dimensionless channel depth for the finite-depth cases, while in the infinite-depth calculations it was set equal to unity. In all cases, the drop was centered in the entry channel, midway between the two side walls of distance H apart and between the top and bottom walls of distance D apart. The effects of the following parameters were studied: drop relative radius $R = a/H$, where a is the spherical radius of the drop; capillary number $\mathrm{Ca} = \mu_e U_{av}/\sigma$, where μ_e is the bulk fluid viscosity, σ is the interfacial tension, U_{av} is the average fluid velocity; and $\lambda = \mu_d/\mu_e$, where μ_d is the drop viscosity. A modified capillary number $\mathrm{Ca}^* = \mu_e U_{max}/\sigma$, where U_{max} is the maximum undisturbed fluid velocity, which occurs in the channel center, was used in some of the comparisons.

4.3.1.1. Channels with the same maximum undisturbed fluid velocity

Two competing effects take place when the motion of a drop in a three-dimensional channel is studied: the form drag exerted by the imposed flow pushing the drop through the channel and the friction exerted on the drop interface near the channel walls. In this section, the effect of

the channel depth on the drop velocity is presented. To do so, instead of using the same capillary number in the different simulations, a modified capillary number Ca* = 0.25 is used so the effect of the channel depth is taken into account by using the maximum velocity of the undisturbed fluid, while the "regular" capillary number only considers the effects of the inlet flow with the average fluid velocity in its definition. In particular, channels with different depths but the same average fluid velocity will have different maximum fluid velocities at the center of the channel where the drop resides. By using the same modified capillary number, the drops in this analysis experience similar ratios of viscous deforming forces to interfacial-tension restoring forces. Figures 4.4 shows the steady-state velocities obtained for a drop of relative radius R = 0.4, Ca* = 0.25 and λ = 1 travelling in a channel of relative depth *D/H* = 1, 1.25, 1.5, 1.75, 2 and 5, and in a 2D channel ($D/H \rightarrow \infty$). Note that $U_{max}/U_{av} =$ 2.10, 2.08, 2.06, 2.03, 1.99, 1.69 and 1.50 for D/H = 1.0, 1.25, 1.5, 1.75, 2.0, 5.0 and ∞, respectively. The values were calculated using the Fourier series from the undisturbed Boussinesq flow.

a) b)

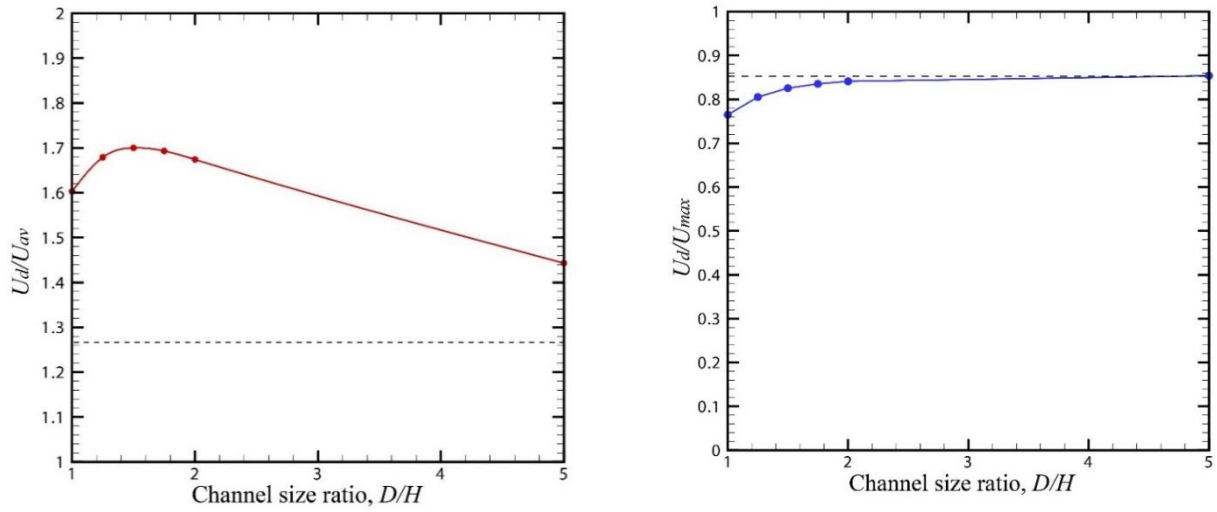

Figure 4.1. Steady-state velocities obtained for a drop of relative radius R = 0.4, Ca* = 0.25 and λ = 1

Results for a drop of relative radius R = 0.4, viscosity ratio λ = 1 and modified capillary number Ca = 0.25 of the a) drop steady-state velocity over average fluid velocity in the x-direction in a long straight channel and b) drop steady-state velocity over the maximum velocity in the channel without the drop (U_{max}) vs channel size ratio. The solid circles are the numerical simulations and the curves are fits to through the data; the dashed lines are the corresponding results for an infinite-depth channel ($D/H \rightarrow \infty$). The maximum drop velocity is found for D/H=1.5 because in shallower channels the drop is slowed down by the hydrodynamic forces exerted by the walls. Better convergence is observed when the drop velocity is non-dimensionalized with the maximum fluid velocity because the effect of the channel walls is taken into account in its calculation.*

Figure 4.4a shows how the drop highest velocity is achieved when D/H = 1.5, which demonstrates that the effect of the hydrodynamic forces exerted by the wall is significant (otherwise, the maximum velocity would take place at D/H = 1 due to higher maximum fluid velocity in the channel center). Better convergence is found when the drop velocity is normalized with the maximum velocity of the undisturbed fluid, because it not only takes into account the inlet volumetric inflow and area, but also the geometry of its cross section.

4.3.1.2. Effect of the drop relative radius

To study the effect of the drop relative radius, three different drop sizes were considered: R = 0.645, 0.4 and 0.25. The larger drop ($2a/H > 1$) had an initial prolate spheroidal shape (a_1/R = 0.31, where a_1 is the minor half-axis), while the smaller drops ($2a/H < 1$) were placed in the channel with an initial spherical shape. Figure 4.5 shows the results obtained for a drop with capillary number Ca = 0.1, viscosity ratio λ = 1, and relative radii R = 0.645, R = 0.4 and R = 0.25.

a) b)

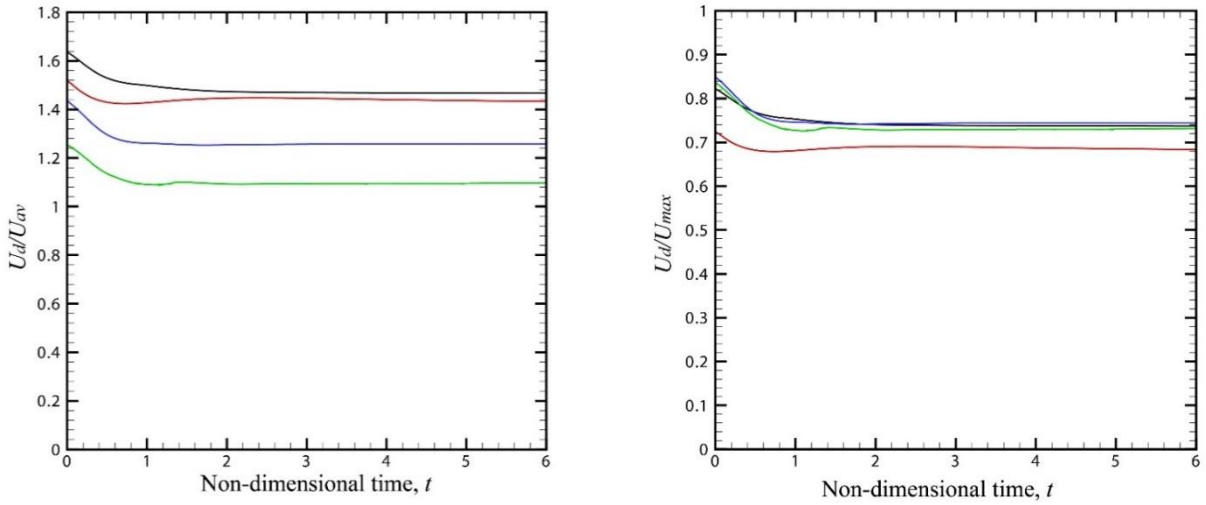

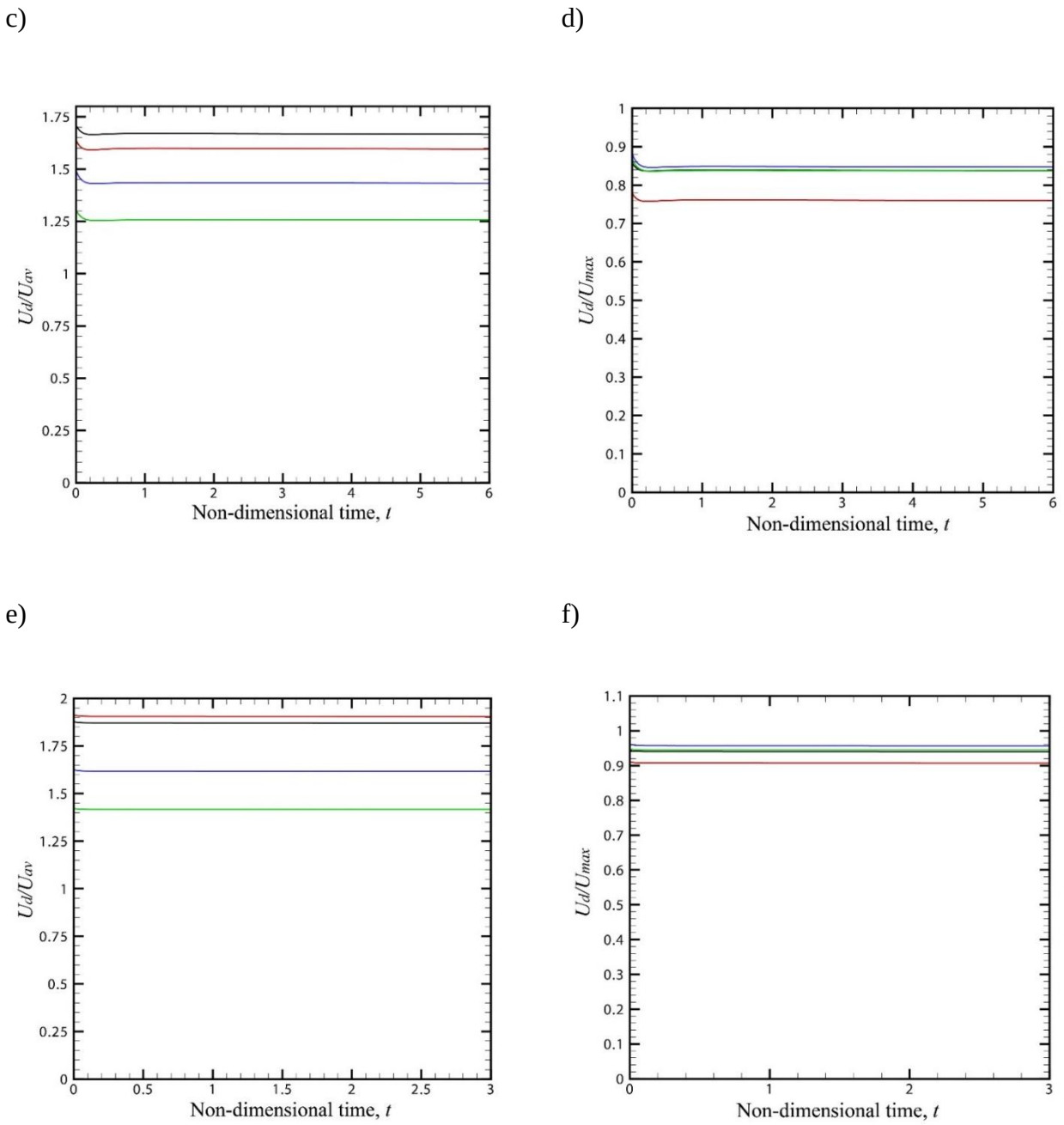

Figure 4.5. Velocities for drops of capillary number Ca = 0.1, viscosity ratio λ = 1, and relative radii R = 0.645, R = 0.4 and R = 0.25.

Drop velocity made dimensionless with the average fluid velocity in the x-direction in a long, straight channel of depth D/H = 1 (red line), 2 (black line), and 5 (blue line), and in a 2D channel (green line) vs time for a drop of capillary number Ca = 0.1 and viscosity ratio λ = 1 and relative radii a) R = 0.645, c) R = 0.4 and e) R = 0.25. Drop velocity made dimensionless

with the maximum velocity in the channel without the drop (U_{max})) vs time for the same drops of b) R = 0.645, d) R = 0.4 and f) R = 0.25. Drops with small relative radii achieve faster velocities in shallow channels due to higher velocity gradients across them, while larger drops are slowed down by the proximity of the channel walls.

Larger drops take more time to achieve a steady-state velocity and shape because they are more deformable than smaller drops, which are more compact. However, in all cases, an initial decrease of the drop velocity occurs as the drop deforms and has an increased drag coefficient. When the drop relative radius is R = 0.645 and the channel relative size is D/H = 1, a transition into a more elongated form is observed and, therefore, the drop velocity slightly increases at longer times as the drop-wall gap becomes larger (see figure 4.6).

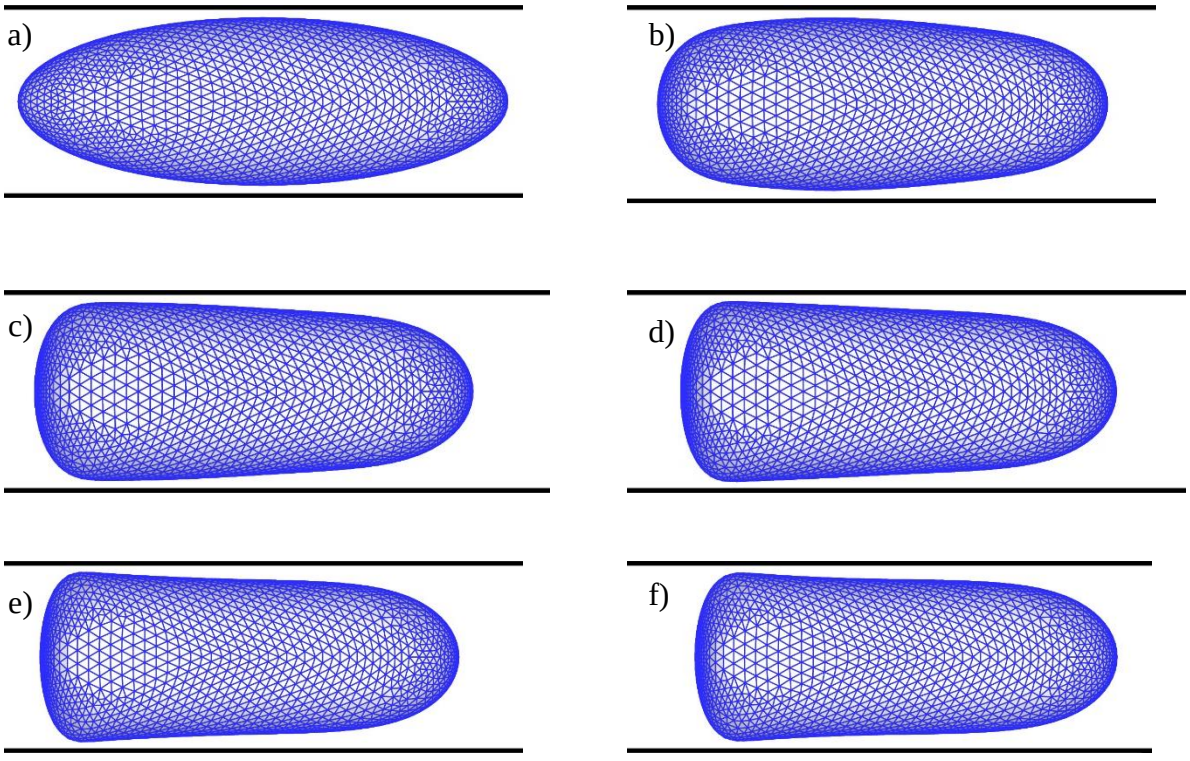

Figure 4.6. Shape evolution for a drop of R = 0.645, = Ca = 0.1 and λ = 1.

Shape evolution for a drop of relative radius R = 0.645, capillary number Ca = 0.1 and viscosity ratio λ = 1 in a long straight channel of D/H = 1. The frames correspond to the non-dimensional times a) t = 0, b) t = 0.2, c) t = 0.5, d) t = 0.7, e) t = 1.2 and f) t = 1.5.

Large drops that nearly fill the channel cross section ($2a/H$ =1.29 and 0.8, and D/H = 1), experience a decrease in their velocity because of the hydrodynamic forces exerted by the channel walls, while smaller drops experience higher velocities when travelling in narrow channels because the interaction with the walls is minimum due to the distance between them and higher velocities take place at the centerline of the channel. Again, better convergence is observed when the drop velocity is nondimensionalized with the undisturbed fluid maximum velocity because the effect of the channel walls and fluid velocity at the channel center is taken into account (see figure 4.7).

a) b)

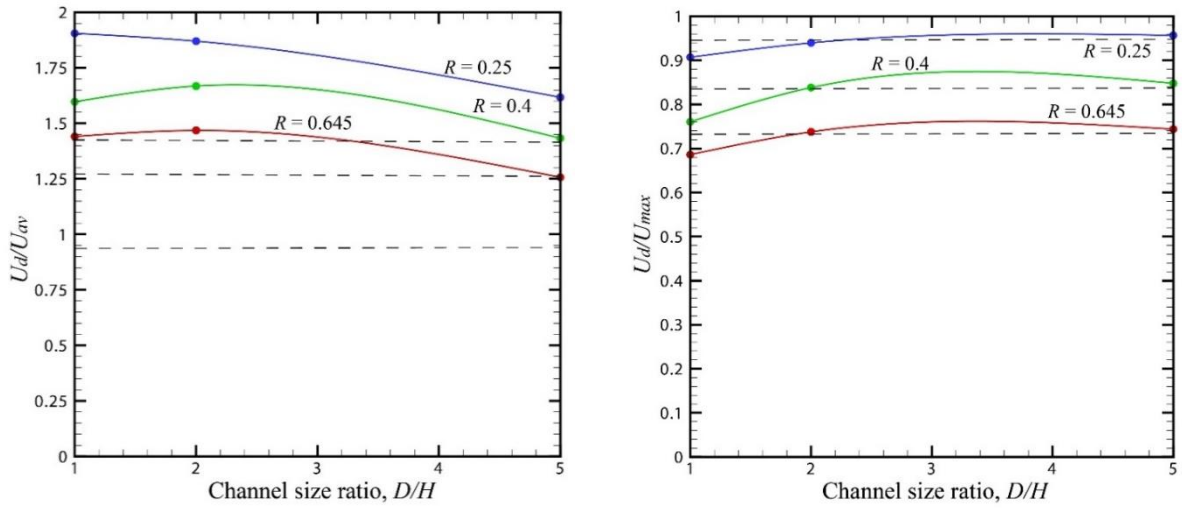

Figure 4.7. Steady-state velocities for drops of Ca = 0.1, λ = 1 and relative radii R = 0.25, 0.4 and 0.645

Results for a drop of capillary number Ca = 0.1, viscosity ratio λ = 1 and relative radii R = 0.25, 0.4 and 0.645 of the a) steady drop velocity over average fluid velocity in the x-direction in a long straight channel and b) steady drop velocity over the maximum velocity in the channel without the drop (U_{max}) vs channel size ratio. The solid circles are the numerical simulations and the curves are fits to through the data; the dashed lines are the corresponding results for an infinite-depth channel ($D/H \rightarrow \infty$). Better convergence is observed when the drop velocity is non-dimensionalized with the maximum fluid velocity because the effect of the hydrodynamic forces exerted by the channel walls is taken into account in its calculation.

4.3.1.3. Effect of the capillary number

Figure 4.8 shows the results obtained for a drop with relative radius R = 0.645, viscosity ratio λ = 1 and capillary numbers Ca = 0.1 and 0.2. The drop was introduced in the channel with an initial prolate spheroidal shape (a_1/R = 0.31).

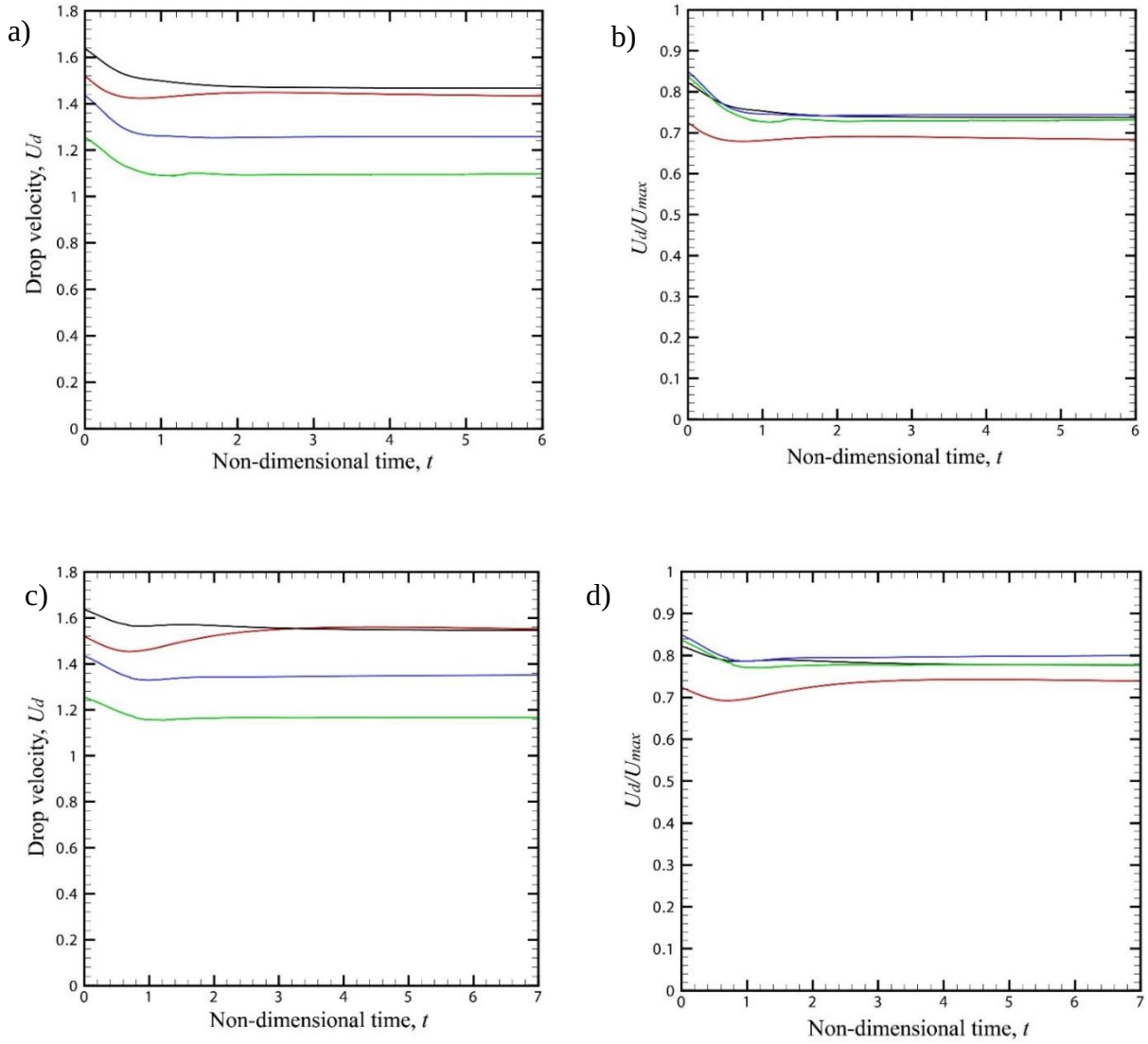

Figure 4.8. Velocities of drops of R = 0.645, λ = 1 and Ca = 0.1 and Ca = 0.2.

Drop velocity in the x-direction in a long straight channel of depth D/H = 1 (red line), 2 (black line), 5 (blue line), and of a 2D channel (green line) vs time for a drop of relative radius R = 0.645, viscosity ratio λ = 1 and capillary number a) Ca = 0.1 and c) Ca = 0.2. Normalized drop velocity (drop velocity over the maximum velocity in the channel without the drop (U_{max})) vs time

for the same drops of b) Ca = 0.1 and d) Ca = 0.2. Drops with larger capillary travel faster but, in both cases, the drop velocity is slowed down in shallow channels due to the proximity between the drop surface and the channel walls.

When the effect of the capillary number is studied, the difference between drop velocities is caused by the steady-state shape of the drop in each case. Figure 8 shows the steady-state shapes obtained for a drop in a long straight channel of depth D/H = 1. When the capillary number is larger, Ca = 0.2 (figure 4.8b), the drop acquires a more elongated shape, so the friction drag coefficient exerted by the surrounding fluid is smaller compared to when Ca = 0.1 (figure 4.8a) so the drop is able to travel faster. The gap between the drop surface and the channel walls is larger, so the drop is not slowed down as much due their proximity. For Ca = 0.2, the higher drop velocities are coincident and achieved when D/H = 1 and 2. The non-monotonic trend of the drop velocity when D/H = 1 is due it shape evolution: initially, it has an ellipsoidal shape (figure 4.9a); then, it acquires a shape where the clearance between its surface and the channel walls is small and the friction drag is larger because of this thin gap (figure 4.9b); and finally it reaches an elongated steady-state shape (figure 4.9c) with a larger gap and reduced friction drag.

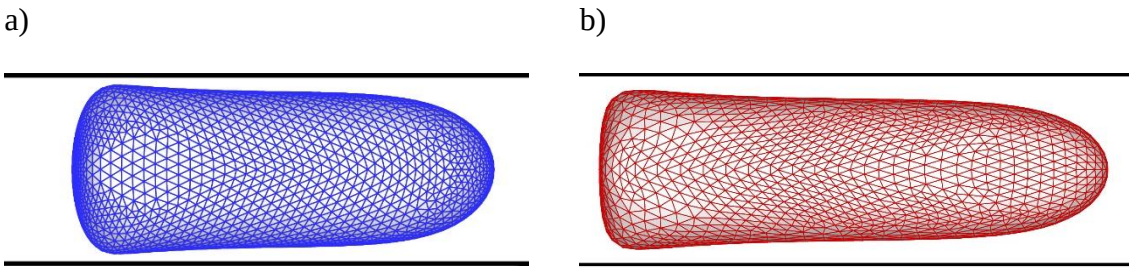

Figure 4.8. Steady-state shapes for Ca = 0.1 and 0.2.

Steady-state shapes for a drop of relative radius R = 0.645, viscosity ratio λ = 1 and capillary number a) Ca = 0.1 and b) Ca = 0.2 in a long straight channel of D/H = 1. More elongated steady-state shapes are achieved with larger capillary numbers.

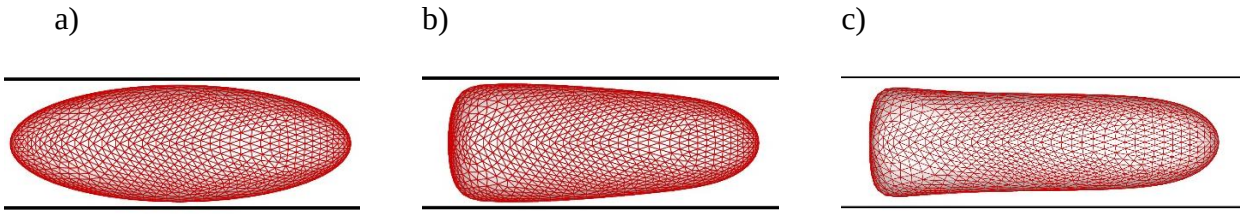

Figure 4.9. Shape evolution for a drop of R = 0.645, λ = 1 and Ca = 0.2.

Shape evolution for a drop of relative radius R = 0.645, viscosity ratio λ = 1 and capillary number Ca = 0.2 in a long straight channel of D/H = 1. The frames correspond to the non-dimensional times a) t = 0, b) t = 0.5 and c) t = 3.0.

Figure 4.10 shows the drop steady-state velocity for the different channel size ratios. Again, better convergence is obtained when the drop is nondimensionalized with the maximum velocity of the undisturbed fluid.

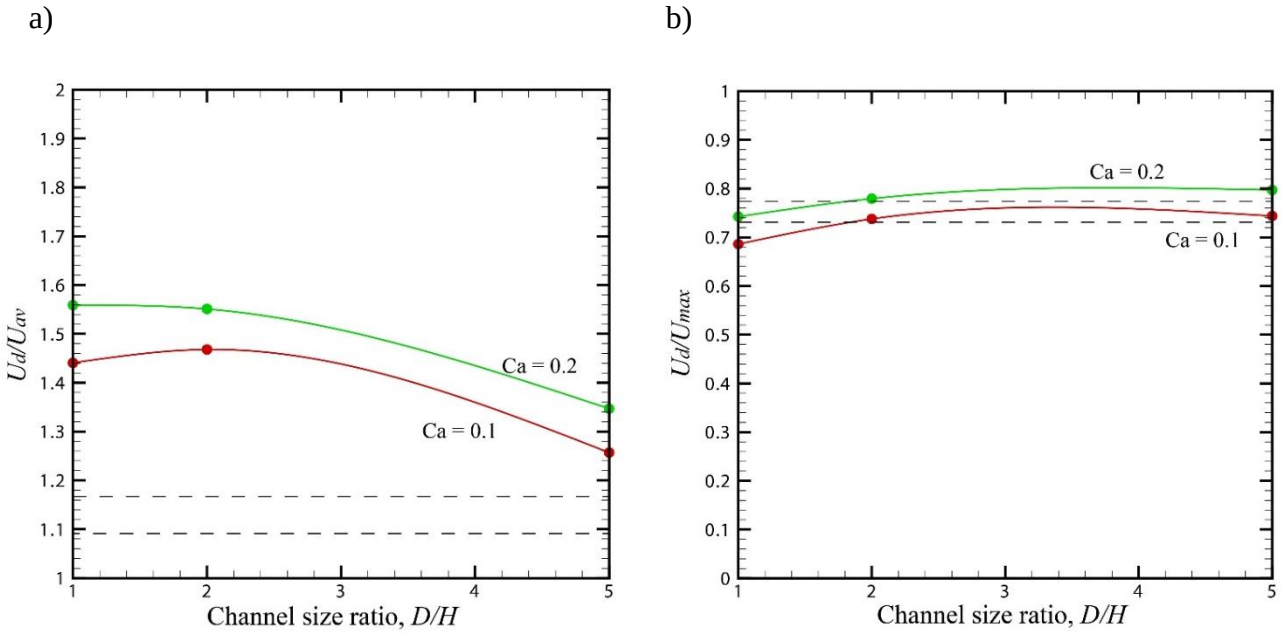

Figure 4.10. Steady-state velocities for a drop of R = 0.645, λ = 1 and Ca = 0.1 and 0.2.

Results for a drop of relative radius R = 0.4, viscosity ratio λ = 1 and capillary numbers Ca = 0.1 and 0.2 of the a) steady drop velocity over average fluid velocity in the x-direction in a long

straight channel and b) steady drop velocity over the maximum velocity in the channel without the drop (U_{max}) vs channel size ratio. The solid circles are the numerical simulations and the curves are fits to through the data; the dashed lines are the corresponding results for an infinite-depth channel ($D/H \rightarrow \infty$). Better convergence is observed when the drop velocity is non-dimensionalized with the maximum fluid velocity because the effect of the hydrodynamic forces exerted by the channel walls is taken into account in its calculation.

4.3.1.4. Effect of the viscosity ratio

Figure 4.11 shows the results obtained for a drop with relative radius R = 0.645, capillary number Ca = 0.1 and viscosity ratios λ = 0.5, 1 and 4. The drop was introduced in the channel with an initial prolate spheroidal shape (a_1/R = 0.31).

a) b)

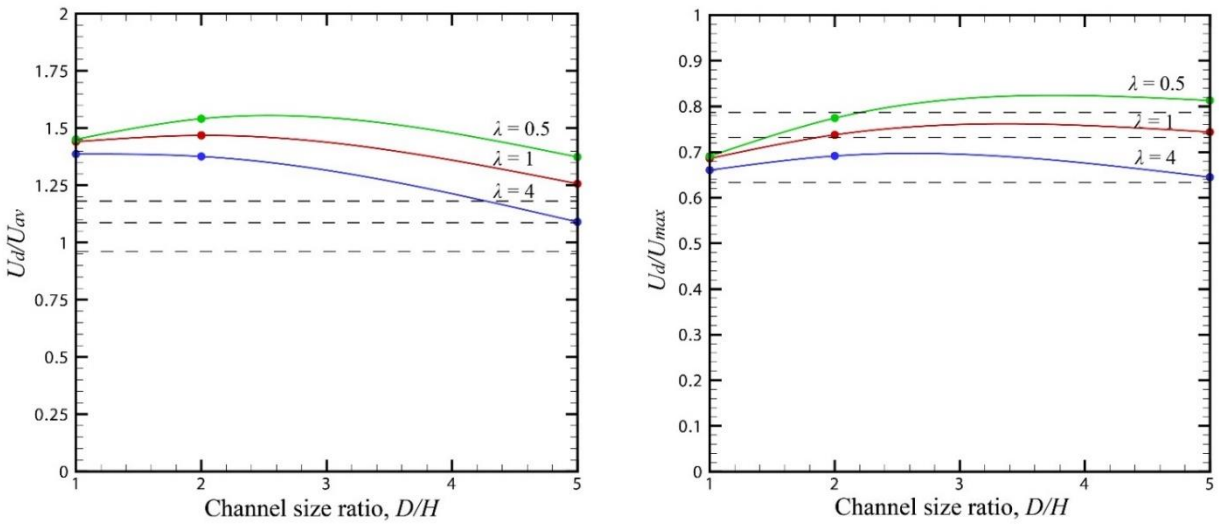

Figure 4.11. Steady-state velocities for a drop of R = 0.645, Ca = 0.1 and λ = 0.5, 1 and 4.

Results for a drop of relative radius R = 0.4, capillary number Ca = 0.1 and viscosity ratios λ = 0.5, 1 and 4 of the a) steady drop velocity over average fluid velocity in the x-direction in a long straight channel and b) steady drop velocity over the maximum velocity in the channel without the drop (U_{max}) vs channel size ratio. The solid circles are the numerical simulations and the curves are fits to through the data; the dashed lines are the corresponding results for an infite-depth channel ($D/H \rightarrow \infty$). Better convergence is observed when the drop velocity is non-dimensionalized with the maximum fluid velocity because the effect of the hydrodynamic forces exerted by the channel walls is taken into account in its calculation.

In this case, the drop reaches higher velocities when its viscosity is smaller than the viscosity of the bulk fluid. When the drop viscosity is lower, with all else equal, the higher tangential mobility of the drop interface reduces the shear stress from the narrow gap between the drop and the wall, so the drop moves faster.

4.3.2. Drop motion in a channel with a Y-bifurcation

To study the effects of the channel depth on the drop behavior (path selection and breakup), the motion of a drop going through a three-dimensional channel with a Y-bifurcation was analyzed. Two different drop sizes were considered, R = 0.645 and 0.25; the value of the capillary number was Ca = 0.1 in both cases and the viscosity ratio λ = 1. Three different relative channel sizes were used, D/H = 1, 2 and 5, and three different flow ratios between the channel branches were studied for each case, $Q_1/Q_2 = 0.5$, 0.75 and 0.95, where Q_1 is the flow rate exiting the upper branch and Q_2 is the flow rate exiting the lower branch.

For small drops, no breakup was observed in any of the studied cases. Figure 4.12 shows the results obtained for a drop of relative radius R = 0.25, capillary number Ca = 0.1 and viscosity ratio λ = 1 in a channel of relative size D/H = 2 where the flow ratio between the branches in the bifurcation is $Q_1/Q_2 = 0.95$:

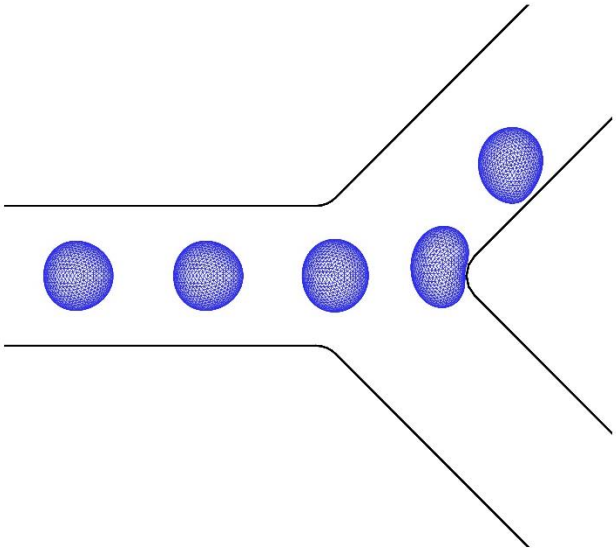

Figure 4.12. Motion of a drop of R =0.25, Ca =0.1 and λ = 1.

Snaps of a drop of R = 0.25, capillary number Ca = 0.1 and viscosity ratio λ = 1 going through the upper branch of a channel of D/H = 2 without breaking. The flow ratio between the branches is $Q_1/Q_2 = 0.95$.

In Figure 4.13, the results for a drop of relative radius R = 0.645, modified capillary number Ca* = 0.21 and viscosity ratio λ = 1 in a channel of relative size D/H = 2, where the flow ratio between the branches in the bifurcation is $Q_1/Q_2 = 0.75$, are presented. Although the drop neck is thinning, an impending breakup situation is not reached before the simulations crash when the drop travels in a finite-depth channel (due to the very close proximity of the drop and the bifurcation corner). For that reason, simulations with larger capillary numbers have been processed, so the viscous forces allow the drop to deform further and a proper analysis of the volume partition of the drop can be performed. However, the same simulations were performed for an infinite-depth channel and, as observed in figure 4.13b, the drop behavior differs from the finite-depth channel simulations as in this case the drop is able to achieve an impending breakup situation.

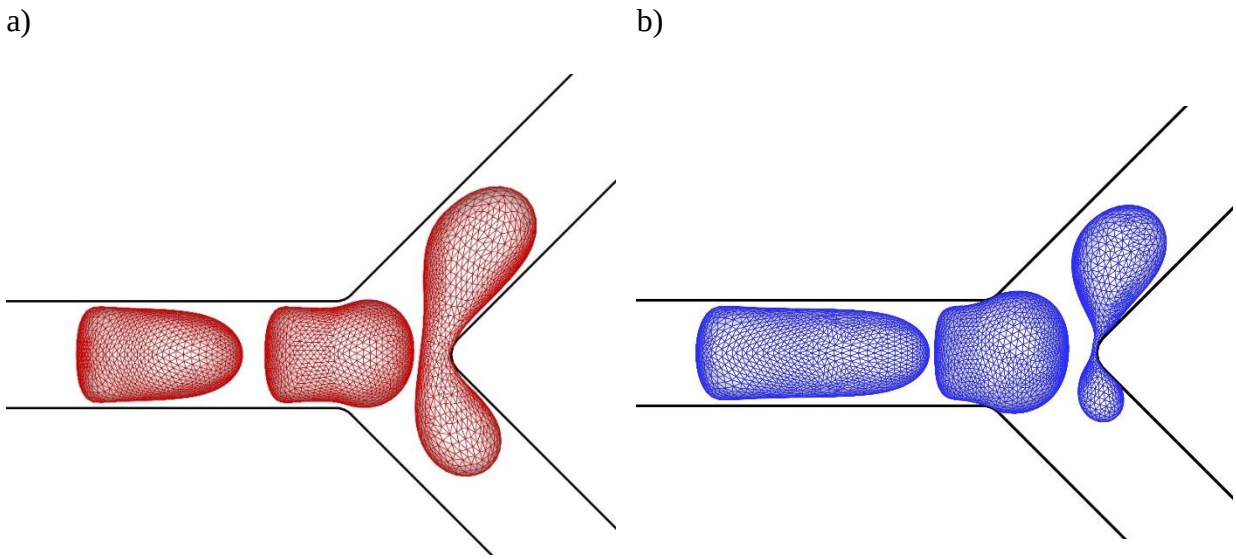

Figure 4.13. Motion of a drop of R =0.645, Ca* =0.21 and λ = 1.

Snaps of a drop of R = 0.645, capillary number Ca = 0.21 and viscosity ratio λ = 1 in a bifurcated channel of a) D/H = 2 and b) infinite-depth interacting with its corner. The flow ratio between the branches is $Q_1/Q_2 = 0.75$. Due to interfacial forces, the simulations stop before the drop can reach an impending breakup situation.*

Figure 4.14 shows the results obtained for a drop of relative radius R = 0.645, capillary number Ca = 0.25 and viscosity ratio λ = 1 in channels of relative sizes D/H =1, 2, and 5 with different flow ratios between the branches $Q_1/Q_2 = 0.5$, 0.75 and 0.95. When the flow ratio between the branches is close to unity (i.e. the volumetric flow going through each branch is similar), the volume partition of the drop is barely affected by the channel non-dimensional depth. However, when the flow going through each branch is considerably different ($Q_1/Q_2 = 0.5$), the drop volume partition ratio is affected by the relative size of the channel and the portion of the drop going through the branch with more volumetric flow increases with the non-dimensional channel depth.

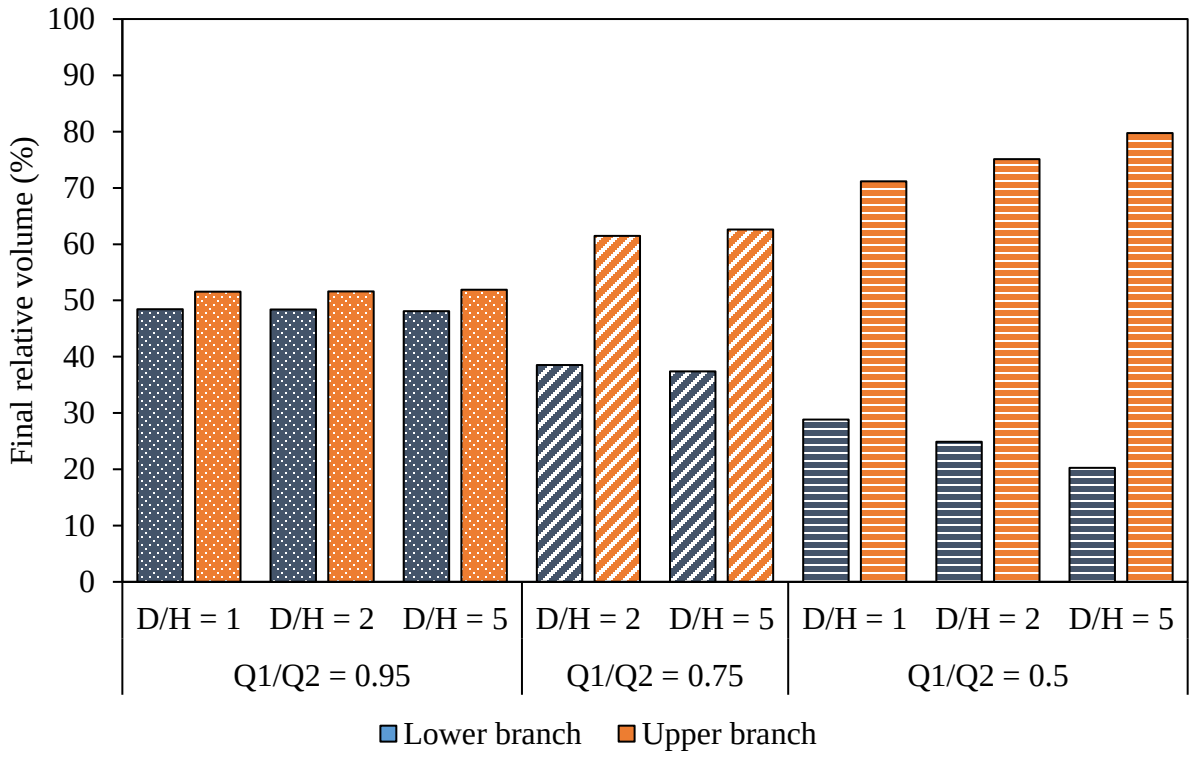

Figure 4.14. Volume partition percentage for a drop breaking in channels with a Y-bifurcation.

Volume partition percentage of a drop with relative radius R = 0.645, capillary number Ca = 0.25 and viscosity ratio λ = 1.0 in channels with a Y-bifurcation and non-dimensional depths D/H = 1, 2 and 5 with flow ratios between the branches Q_1/Q_2 = 0.5, 0.75 and 0.95. The drop partition ratio is only affected when the flow going through each branch is considerably different.

4.4. Concluding remarks

A novel boundary-integral technique to describe drop motion in finite-depth microchannels was presented in this Chapter. A new wall meshing method was introduced, followed by a triangular tessellation to create the mesh for the top and bottom walls of the channel and for the moving-frame around the drop. The analytical solution of Boussinesq (1868) for the undisturbed flow in rectangular channels was used at the entrance(s) and exit(s) of the channel. Then, the

undisturbed flow field throughout a complex channel was calculated in the form of a double-layer boundary-integral equation and applied to the boundaries of the moving-frame.

The effect of the channel depth on the drop velocity in long, straight channels was studied. Smaller drops achieved faster velocities than larger drops (which are slowed by viscous stresses when in close contact with the walls). Two competing effects were observed in the motion of large drops nearly filling the channel cross section: the forces exerted by the imposed flow (higher velocities take place at the centerline of shallow channels due to higher velocity gradients across them) and hydrodynamic forces exerted by the channel walls that slowed down the drops. As a result, the maximum drop velocity occurred for an intermediate value of the channel aspect ratio (depth over width). Perhaps surprisingly, drops with higher capillary numbers achieved higher velocities due to the shape they acquired: because of viscous forces, they became more elongated and so the drop-wall clearance was larger and the friction drag coefficient exerted by the surrounding fluid was smaller.

Next, the effects of channel depth on drop motion and potential breakup in Y-channels was investigated using the finite-depth code. Results show that larger drops are more likely to break than smaller drops, and the volume partition ratio of the drop is affected only when the flow going through each branch of the bifurcation is considerably different. Different volume partition ratios are observed when comparing finite- and infinite-depth simulations.

Chapter V

Experiments on drops in microchannels

Abstract

In this chapter, microvideo experiments to observe deformable drops are described for two different channel geometries. The results obtained from the experimental work are presented and compared to the results obtained computationally. Our boundary-integral algorithm is shown to accurately characterize the drop motion and deformation that take place in T-shaped and cross-shaped microchannels, including with and without pending breakup.

5.1. Introduction

5.1.1. Background and overview

With the intent of gaining experimental tools to observe drop deformation in microchannels, I visited the laboratory of Professor Patrick Spicer at the University of New South Wales for four weeks during November-December 2019. Guidance on the experimental setup was provided by Mr. Haoda Zhao, a Ph.D. student in Professor Spicer's group. The experiments employed silicon droplets suspended in glycerin/water mixtures. The drops were passed through a T-junction or a cross-shaped channel, and the dynamics of the drop shapes were recorded with a video camera through a microscope.

Our goal was to stablish the experimental methods and obtain preliminary results, and this goal was met. I then planned to build a similar setup at the University of Colorado, but with larger

channels for ease of drop visualization. However, the labs were closed during March-May 2020 due to COVID-19, and these plans were set aside due to the time requirements for the machine shop to construct the channel and then the experiments to be performed.

5.1.2. Literature review and context for current work

Controlling and manipulating the shape, size and composition of droplets is of significant interest in the food industry (Desai & Jin Park, 2005), in the cosmetic industry, in the pharmaceutical industry for drug delivery (Hsieh et al., 1983), and in biotechnology in general. For this reason, several authors described multiple techniques in their reviews (Champion et al., 2007; Glotzer & Solomon, 2007; Shum et al., 2010; Wang et al., 2011). In particular, droplet-based microfluidic devices have obtained special relevance to obtain complex particles with desired properties (Wang et al., 2011).

Shum et al. (2010) used droplet microfluidics to create non-spherical particles. With their proposed techniques (i.e., arrested coalescence, asymmetric polymer solidification, polymerization in microfluidic flow, and evaporation-driven clustering), they were able to create single and multiple emulsion droplets of different shapes.

Kim & Vanapalli (2013) used crystallizable oils to produce spherical and non-spherical fat particles. They generated the oil droplets using a cross-junction and then thermally solidified them in a microcapillary. Changing the production conditions and the temperature of the microcapillary, they proved that the size, shape, and crystallinity of the drops can be controlled.

Raj et al. (2014) created a technique to deposit droplets of desired shapes. They could modify droplet shapes ranging from squares, rectangles, hexagons, octagons, to dodecagons via the design of the structure or chemical heterogeneity on the surface. They also studied the physical insights to develop a universal model for the three-dimensional droplet shape by characterizing the

droplet side and top profiles. Using standard contact photolithography and deep-reactive ion etching, they were able to produce cylindrical and cuboidal silicon arrays arranged in square, rectangular and hexagonal patterns. They demonstrated that arrays of droplets with controlled shapes can be created using their approach.

Wang et al. (2018) were able to produce soft rotationally symmetric (hexosome) particles using a simple emulsion precursor process. They showed that the droplet size, crystallization rate, and surfactant packing parameter have a significant effect and can control the particle final shape.

Caggioni et al. (2018) were able to create non-spherical, oil-in-water emulsion droplets by crystallizing a portion of the oil phase. They used a continuous microfluidic flow to produce droplets and, controlling the exit temperature, they could obtain different shapes: spheres, ellipsoids, and rods.

The research described above has experimentally demonstrated that drops and particles of various shapes can be produced in microchannels with junctions and flow control. A complementary goal of the current dissertation is to demonstrate that desired, complex shapes can be predicted via boundary-integral simulations. In this chapter, the aim is to investigate the ability of our algorithms (infinite-depth channels – Chapters 2 & 3, and finite-depth channels – Chapter 4) to successfully characterize and predict the motion and shape that a drop obtains when placed inside a microchannel with a controlled flow.

5.2. Experimental setup

5.2.1. Channel preparation

The first step is to make a polydimethylsiloxane (PDMS) channel. To do so, square-shaped capillaries (cross section: 1.4 x 1.4 mm) are glued on a glass slide with the desired channel shape

to create a mold. Then, the mold is covered with a PDMS paste (the ratio of the curing agent and silicone base is 1:8). The paste must be vacuumed for an hour to remove any trapped air bubbles. Then, it is necessary to let the PDMS channel solidify at 50˚C overnight. A glass slide is used as a lid to the mold. The mold and the glass slide are rinsed separately with pure ethanol and Milli-Q water and dried with pressured air. Then, both pieces are inserted into a plasma cleaner (figure 5.1), vacuumed for about 3 minutes, and then subjected to plasma treatment for 1 min to oxidize them and make them hydrophilic so the glass slide can stick together with the PDMS channels.

Figure 5.1. Plasma cleaner.

Plasma cleaner used to oxidize the components that form the microchannel in order to make them hydrophilic.

After the plasma treatment, the mold and the glass are put together and the channel is rinsed with 1 wt% of polyvinyl alcohol (PVA) solution for 10 minutes. Then, the channel is blow dried and, subsequently, heated at 110 ˚C for 15 minutes to evaporate any water that may be left inside it. Figure 5.2 shows the appearance of the channel in each step.

a) b) c)

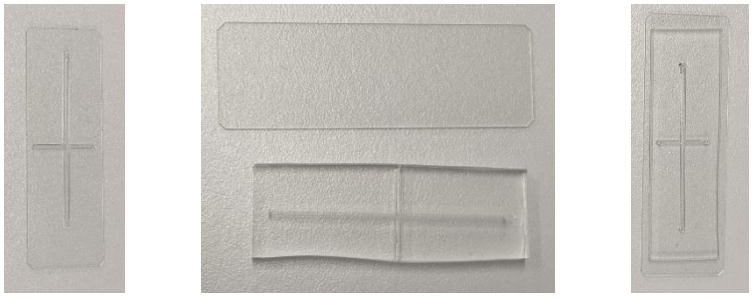

Figure 5.2. Channel molds.

Pictures of the a) mold to create the cross-shaped channel, b) solid PDMS paste and covering glass slide before the PVA treatment and c) finished channel used in the experiments.

5.2.2. Flow and optical setups

A schematic representation of a cross-shaped channel with the fluid inlets and outlets is presented in figure 5.3. Both fluids are inserted in the geometry by two different syringe pumps connected by a T-shaped microfluidic junction where the droplets are formed (Thorsen et al., 2001; Tice et al., 2003; Van Der Graaf et al., 2005). The microscope used was the model Leica DM 2500M, the camera was QImaging optiMOS^{TM}, and the images were recorded using the software Micro-Manager 1.4 every 100 ms. The inlet flowrates were controlled with calibrated syringe pumps, SyringeONE NE-1000, which are fully programmable with their keypad interface. The outlet flow rates were not controlled.

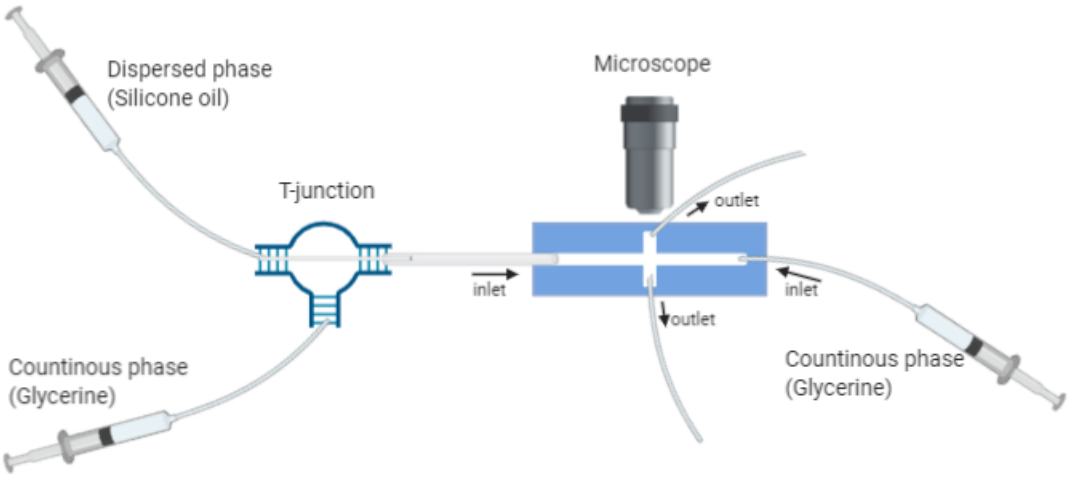

Figure 5.3. Schematic representation of the experimental setup.

Schematic of the flow and optical used in the experiments for a cross-shaped microchannel (not to scale). Not shown are the calibrated pumps that drive the syringes.

5.2.3. Fluid properties

As mentioned before, the fluid used to create the drops is silicone oil, and the bulk fluid is made of glycerin and water. In order to be able to computationally reproduce the experiments, it is necessary to calculate the drop modified capillary number $\mathrm{Ca_m} = (a/H)\,\mathrm{Ca}$, Reynolds number $\mathrm{Re} = \rho_e U H/\mu_e$, dimensionless radius $\hat{a} = a/H$, and viscosity ratio $\lambda = \mu_d/\mu_e$, where a is the non-deformed drop radius, H is the channel height, $\mathrm{Ca} = \mu_e U/\sigma$ is the capillary number, μ_e is the carrier fluid viscosity, μ_d is the drop viscosity, σ is the interfacial tension between the fluids, U is the average fluid velocity, and ρ_e is the density of the bulk fluid. The modified capillary number must be $\mathrm{Ca_m} \sim \mathrm{O}(0.1 - 1)$ to observe enough drop deformation, and the Reynolds number should be $\mathrm{Re} \leq \mathrm{O}(1)$ to satisfy the Stokes equation. Both fluids are Newtonian, and no surfactants were added. Table 5.1 shows the fluid properties for a mixture of 10:1 v:v glycerin/water, and for a

mixture of 20:1 v:v glycerin/water and table 5.2 shows the and experiment parameters for each case. The flow rate is $Q = UH^2$.

Table 5.1. Properties of the fluids used in the experiments.

Fluid	**Silicone oil**	**Glycerin/water (10:1 v:v)**	**Glycerin/water (20:1 v:v)**
Density, ρ (g/cm^3)	0.97	1.24 (Volk & Kähler, 2018)	1.25 (Volk & Kähler, 2018)
Viscosity, μ (g/cm-s)	3.17	3.43 (Volk & Kähler, 2018)	5.92 (Volk & Kähler, 2018)

Density and viscosity of silicone oil and the mixtures of glycerin and water at 21°C.

Table 5.2. Experimental parameters.

Volumetric flow, Q (mL/min)	**Glycerin/water 10:1 v:v**		**Glycerin/water 20:1 v:v**	
	Capillary number, Ca	**Reynolds number, Re**	**Capillary number, Ca**	**Reynolds number, Re**
0.5	0.032	0.022	0.067	0.013
1	0.063	0.043	0.133	0.025
1.5	0.095	0.065	0.200	0.038
2	0.127	0.086	0.267	0.050
2.5	0.159	0.108	0.334	0.063

3	0.190	0.129	0.400	0.075
3.5	0.222	0.151	0.467	0.088

Capillary number and Reynolds number for different flow rates.

To determine the interfacial tension between the droplets and the carrier fluid, the pendant drop method is used (Stauffer, 1965). This method is based in the analysis of the drop shape (using the Young-Laplace equation) and measurement of the contact angle between the fluids. Figure 4a shows the experimental equipment used, and figure 4b shows an example of the drop deformation recorded by the camera during the experiments. Table 5.3 the results obtained for droplets made of silicone oil and pure glycerin, a 20:1 v:v mixture of glycerin/water and a 10:1 v:v mixture of glycerin/water. For each system, three measurements were made.

a) b)

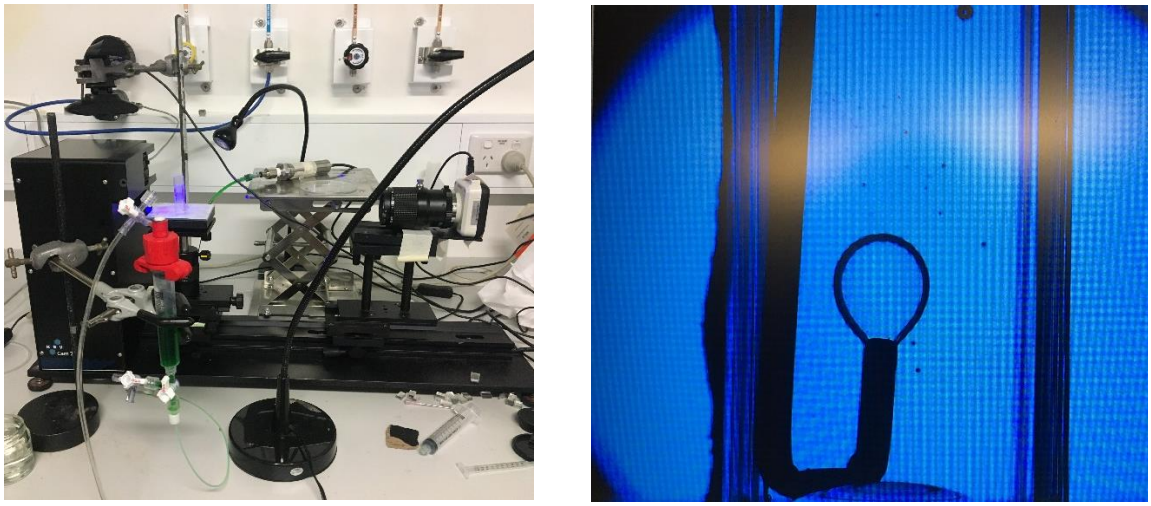

Figure 5.4. Pendant droplet method.

a) Experimental setup of the pendant droplet method and b) example of the outcome of the method used in the analysis of the drop shape.

Table 5.3. Interfacial tension between the fluids used in the experiments.

Droplet fluid	**Bulk fluid**	**v_g:v_w (bulk fluid)**	**Interfacial tension, σ (g/s^2)**
Silicone oil	Glycerin	-	35 ± 1
Silicone oil	Glycerin/water	20:1	38 ± 2
Silicone oil	Glycerin/water	10:1	46 ± 2

Measured values and standard deviation of the interfacial tension between silicone oil and different mixtures of glycerin and water (shown as volume ratios).

5.2.4. Channel geometries

Figure 5.5 shows the two different channel geometries that have been used in the experiments: a) T-junction and b) cross-shaped channel. The cross section of each channels is 1.4 mm x 1.4 mm, and the lengths of the channels are 25 mm for the stem of the T, 37.5 mm for each arm of the T, 18.8 mm for the shorter arms of the cross-shaped channel and 37.5 mm for the longer arms of the cross-shaped channel.

a) b)

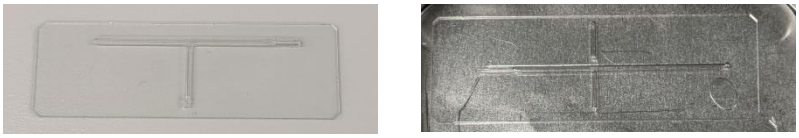

Figure 5.5. Molds of the channels.

Molds used to create the a) T-junction and b) cross-shaped channel.

5.2.5. Experimental conditions

The room temperature during the experiments was 21°C, so the properties of the fluids are those in Table 5.1. Droplets were generated on-the-fly in a T-junction positioned upstream of the channels: the disperse phase was introduced through one of the side branches using a syringe that had a needle attached to it, while the continuous phase was introduced through the stem of the channel (see figure 3), making the disperse phase break into drops. The flow rate of the continuous phase (bulk fluid) ranged from 0.5 mL/min to 3.5 mL/min, while the flow rate of the disperse phase (droplets) was 0.1 mL/min. In order to have enough separation between droplets, the disperse phase flow was stopped after the creation of some droplets and switched on again when needed. The inlet flowrates were controlled using the keypad of the fully programmable syringe pumps, while there was no control over the flowrates of the outlets. In the experiments with the T-shaped channel, we used a tubing clamp to partially constrict one of the exit branches, which gave a flow ratio different than the unity so the drops would exit through one of the branches instead of breaking in the middle of the junction. Unfortunately, the resulting flow ratio was difficult to control and was not directly measured.

5.2.6. Computational conditions

To compare the experimental results to our boundary-integral algorithm (Navarro et al., 2020), initially spherical drops with 2160 triangles on their surface were placed in the two-dimensional and three-dimensional representations of the channels created by connecting straight segments. Two-dimensional (Zinchenko et al., 2012) and three-dimensional (Chapter 4 of this dissertation) moving frames around the drop were used. The details of the algorithm are described by Navarro et al. (2020) and in Chapter 2 of this dissertation for the two-dimensional simulations,

and in Chapter 4 of this dissertation for the three-dimensional simulations. Figure 5.6 shows where the initially spherical drops were released in the channels for the simulations.

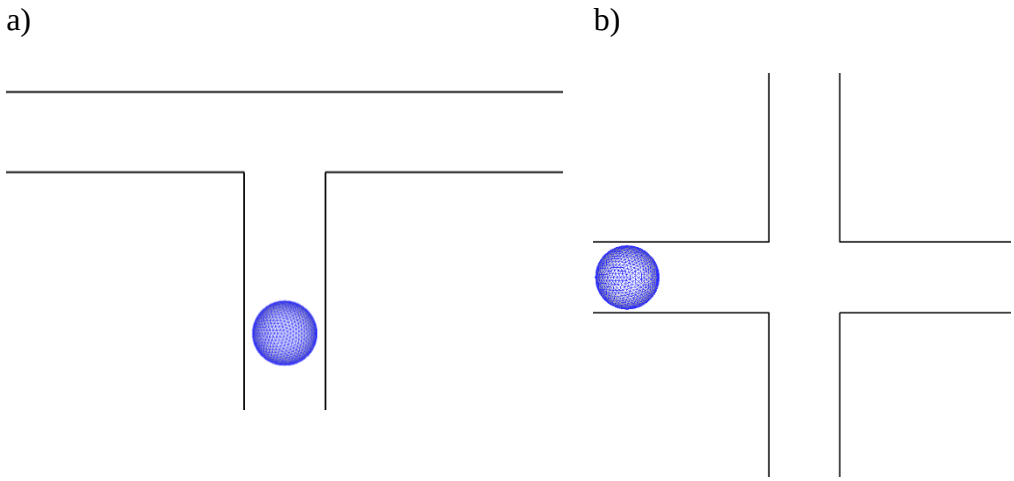

Figure 5.6. Schematic representation of the start of the simulations.

Initial drop shape and position in a) T-junction and b) cross-shaped channel.

5.3. Results and discussion

Several dozen experiments were performed over the course of my four-week visit to the University of New South Wales. However, the majority of them was done to develop the experimental procedures and establish the appropriate conditions. Near the end of my stay, we were able to obtain clear microvideos of drop motion and deformation. In what follows are images from the best clips from a T-junction and a cross-shaped channel.

5.3.1. T-shaped channel

A drop of radius $a \approx 0.56$ mm was introduced through the stem branch of the T-shaped channel that contained a flow of glycerin/water 10:1 v:v of 2.0 mL/min. The corresponding dimensionless radius is $\hat{a} \approx 0.40$ and the modified capillary number is $Ca_m = 0.051$. The viscosity

ratio between the fluids is λ = 0.924. The equipment used did not allow to control precisely the flow ratio between the two outlets, so several simulations were needed to obtain the value that most closely reproduces the observed drop behavior, which is $Q_{left}/Q_{right} \approx 0.33$. This value can also be estimated by comparing how fast the drop travels while in the stem of the T and how fast it travels when in the right arm of the T. It was not possible to create drops with a drop-to-drop separation of at least one radius with the equipment provided, so in the experiments the drop shape and velocity were affected by the presence of other drops, while in the computational simulations only one drop at a time was studied. For both infinite- and finite-depth channel simulations, the drop was started as spherical, with its center located a distance 2*H* below the top of the stem of the T. The time at which the drop had just begun to enter the top of the T was chosen as t = 0 for both the simulations and experiment. The capillary number is based on using the same average flow velocity in the infinite-depth channel simulation as for the finite-depth channel simulation and experiment. Figure 5.7 shows the results obtained experimentally, while figure 5.8 contains the results obtained with the channel of infinite-depth simulations and figure 5.9 shows the results for the finite-depth channel simulations.

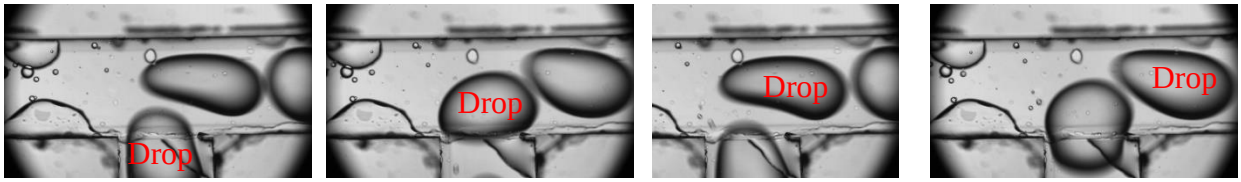

Figure 5.7. Experimental results for a T-shaped channel.

Experimental results for a silicon oil droplet entering through the stem and deforming and going through the right branch of a T-shaped microchannel. The snapshots correspond to times t = 0, 0.1, 0.2 and 0.3 s.

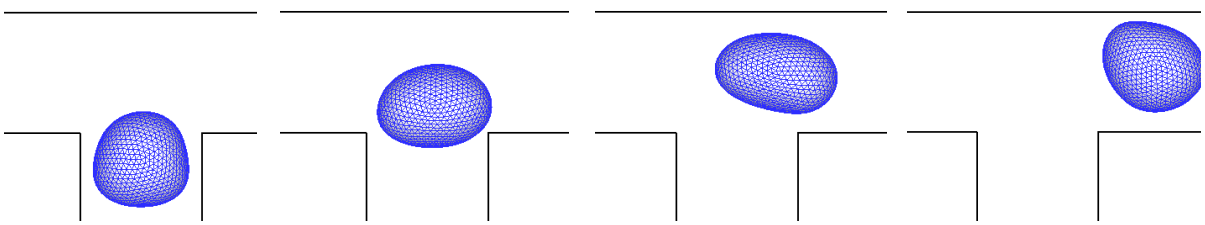

Figure 5.8. Computational results for an infinite-depth T-shaped channel.

Computational results for a silicon oil droplet deforming and going through the right branch of a 2D T-shaped microchannel, with $\hat{a} \approx 0.40$, $Ca_m = 0.05$, $\lambda = 0.924$, *and* $Q_{left}/Q_{right} \approx 0.33$ *at t = 0, 0.03, 0.07 and 0.13 s.*

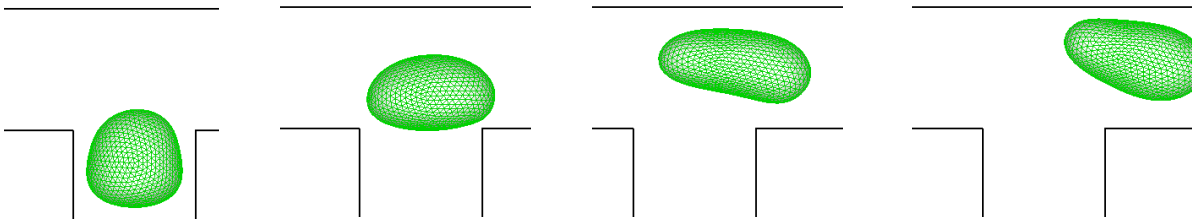

Figure 5.9. Computational results for a finite-depth T-shaped channel.

Computational results for a silicon oil droplet deforming and going through the right branch of a 3D T-shaped microchannel, with $\hat{a} \approx 0.40$, $Ca_m = 0.05$, $\lambda = 0.924$, *and* $Q_{left}/Q_{right} \approx 0.33$. *The channel depth is the same as the height of the channel branches. The snapshots are at times t = 0, 0.03, 0.07 and 0.1 s.*

The agreement between the simulations and the experiment is good, although the drop moved faster in the simulations. This difference is likely due to presence of other drops nearby in the experiment, which slowed down the principal drop. When the results between the simulations are compared, the drop in the infinite-depth channel moves slower than the drop in the finite-depth channel. As described in Chapter 4, this difference is likely due to the lower velocity of fluid at

the center of the channel, and lower velocity gradients across the channel, for the infinite-depth case than for the finite-depth case with the same flow rate per unit depth and, hence, the same average fluid velocity. The infinite-depth simulation shows less deformation compared to the finite-depth simulation or the experiment because of the absence of the front and bottom walls of the channel causing hydrodynamic stress on the drop. The amount of deformation in the finite-depth simulation shows good agreement with the experiment. If, as in the previous Chapter of this dissertation, the maximum velocity of the fluid in a finite-depth channel (i.e. the maximum velocity of the fluid in the experiments) is used in the capillary number definition, $\mathrm{Ca}_m^* = \left(\frac{a}{H}\right)\mu_e U_{max}/\sigma$, better agreement is found between the results for the simulations with an infinite-depth channel and the experimental results due to higher deformability of the drop. Figure 5.10 shows the shapes obtained for a drop in an infinite-depth T-shaped channel of $\mathrm{Ca}_m^* = 0.105$.

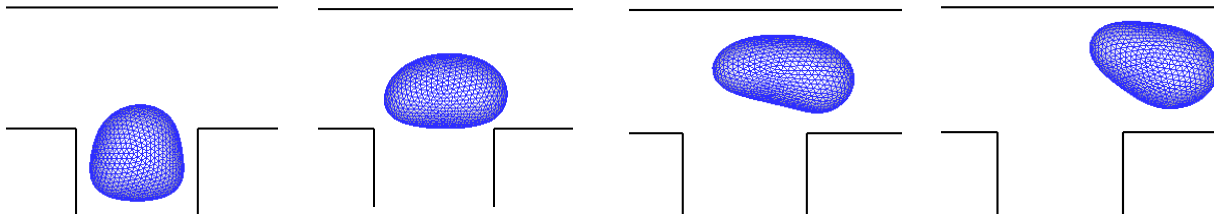

Figure 5.10. Computational results for an infinite-depth T-shaped channel.

Computational results for a silicon oil droplet deforming and going through the right branch of an infinite-depth T-shaped microchannel, with $\hat{a} \approx 0.40$, $Ca_m^* = 0.105$, $\lambda = 0.924$, *and* $Q_{left}/Q_{right} \approx 0.33$ *at t = 0, 0.04, 0.07 and 0.11 s. With the new definition of the capillary number which includes the maximum velocity of the fluid instead of its average velocity, the drop is able to deform more and better agreement is found between the experimental results and the simulations.*

5.3.2. Cross-shaped channel

A drop of a ≈ 0.63 mm was introduced in the one of the branches of the cross-shaped channel that contained a flow of 20:1 v:v glycerin/water of 2.5 mL/min, yielding $\hat{a} \approx 0.45$ and $Ca_m = 0.15$. The viscosity ratio between the fluids is $\lambda = 0.535$. The channel contained two inlets and two outlets opposite to each other, with essentially equal flow rates in each microchannel. Figure 5.11 shows the deformation of the drop at different times during the experiment, figure 5.12 shows the drop deformation in the equivalent simulations for a channel with infinite depth, and figure 5.13 contains the results obtained in similar simulations with a finite-depth channel of square cross-section. Very good agreement is observed when comparing the drop shapes experimentally and computationally. Furthermore, the time needed by the drop to reach impending breakup in the experiments and in the simulations for the finite-depth channel is very similar. In the infinite-depth channel simulation, the drop experienced less stretching (shorter and more regular neck, and more rounded lobes), if compared to the finite-depth channel frames. Due to code limitations, simulations stopped before the neck of the drop was as thin as in the experiments. However, in Chapter 2, an extensive study of the drop neck approaching impending breakup is presented, which shows a very rapid pinch-off in the final stages and favorably compares to asymptotic theory. Note also that, although the imposed base fluid flow is symmetric, the introduction of the drop (or several drops, in the case of the experiments) in one arm of the cross-channel causes an asymmetry. This asymmetry is most evident in the experiment and the simulation for a channel of finite depth, and less so for the infinite-depth channel simulation where the drop does not have a large effect on blocking the flow in the entry arm of the cross-channel.

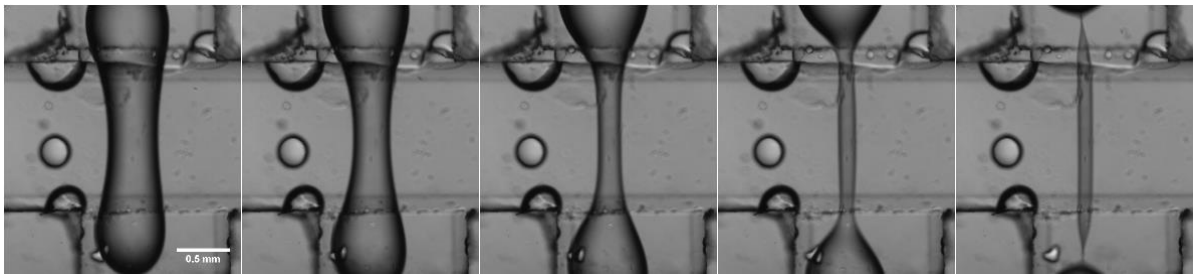

Figure 5.11. Experimental results for a T-shaped channel.

Experimental results for a silicon oil droplet deforming and breaking inside a cross-shaped microchannel. The snapshots are at times t = 0, 0.1, 0.2, 0.3 and 0.4 s.

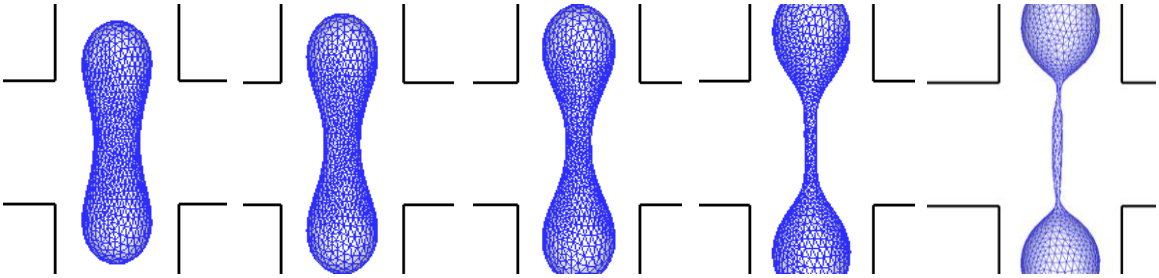

Figure 5.12. Computational results for an infinite-depth cross-shaped channel.

Computational results for a silicon oil droplet deforming and breaking inside an infinite-depth cross-shaped microchannel, with $\hat{a} \approx 0.45$, $Ca_m = 0.15$, $\lambda = 0.535$, *and* $Q_{top} = Q_{bottom} = Q_{left} = Q_{right} = Q$. *The snapshots are at times t = 0, 0.06, 0.12, 0.28 and 0.31 s.*

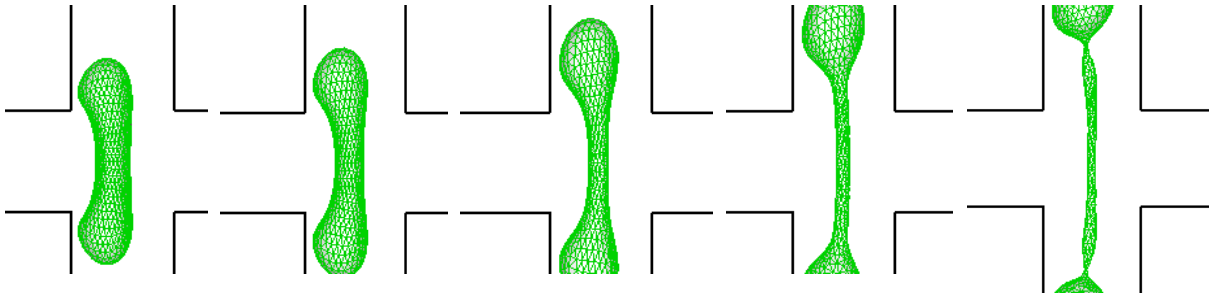

Figure 5.13. Computational results for a finite-depth cross-shaped channel.

Computational results for a silicon oil droplet deforming and breaking inside a finite-depth cross-shaped microchannel with $\hat{a} \approx 0.45$, $Ca_m = 0.15$, $\lambda = 0.535$, and $Q_{top} = Q_{bottom} = Q_{left} = Q_{right} = Q$. The channel depth is the same as the height of the channel branches. The snapshots correspond to times t = 0, 0.13, 0.20, 0.26, and 0.38 s.

Figure 5.14 shows the results obtained for a drop in an infinite-depth cross-shaped channel using the definition of the modified capillary number $\mathrm{Ca}_m^* = \left(\frac{a}{H}\right)\mu_e U_{max}/\sigma = 0.315$. Again, better agreement is found between the simulations and the experimental results because the effect of the channel walls is taken into account in the calculation of the maximum velocity of the fluid. In this case, the asymmetry of the problem becomes evident in the drop shape evolution.

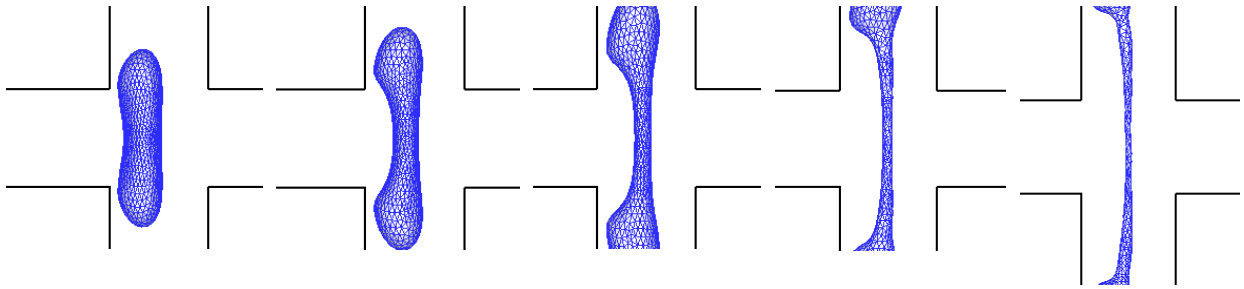

Figure 5.14. Computational results for an infinite-depth cross-shaped channel.

Computational results for a silicon oil droplet deforming and breaking inside an infinite-depth cross-shaped microchannel, with $\hat{a} \approx 0.45$, $Ca_m^* = 0.315$, $\lambda = 0.535$, and $Q_{top} = Q_{bottom} = Q_{left} = Q_{right} = Q$. The snapshots are at times t = 0, 0.06, 0.16, 0.28 and 0.38 s. When the maximum velocity of the surrounding fluid is included in the definition of the capillary number, better agreement is found between the simulations and the experiments.

5.4. Concluding remarks

Our boundary-integral algorithm was shown to accurately describe the drop motion and deformation inside a T-shaped channel and a cross-shaped channel. Very different shapes were obtained with those two geometries. Simulations were performed for infinite- and finite-depth channels, and quantitative differences in the drop behavior are observed when comparing them: faster and more pronounced drop deformation takes place when the drop is confined in a finite-depth channel. However, if the capillary number is defined using the maximum velocity of the carrier fluid instead of its average velocity, the drop behavior and deformation is similar in both simulations (infinite- and finite-depth channels).

In the case of the T-shaped channel, we did not have the proper equipment to measure the independently measure flow ratio between the two exit branches of the channel. For that reason, multiple simulations were performed to find the flow ratio that gave the best fit of experiments and theory. A similar flow ratio was also estimated independently by comparing the experimental drop speeds before and after it passed through the T junction. The drop shape evolution for the infinite- and finite-depth channel simulations differ due to the effect of the top and bottom walls of the channel on the drop motion and deformation, with the finite-depth channel simulations showing more deformation and better agreement with the experiments. When the effect of the channel walls is taken into account in the definition of the capillary number in the infinite-depth channel simulations, the drop is able to deform more and its deformation is closer to the deformation observed in the experimental results. In the experiments, the drop velocity is slowed down by the presence of other drops, so it takes longer for it to pass through the T-junction.

In the case of the cross-shaped channel, the flow in each of the branches is the same (the problem is symmetric in this case) and the drop shapes are similar for all three cases (experiments,

infinite-depth channel simulations and finite-depth channel simulations). The rate of drop deformation is most similar for the experiments and the finite-depth channel simulations, because the algorithm is able to accurately reproduce the experimental conditions. The infinite-depth channel simulations were stopped at an earlier time because of code limitations, but the difference with the other results is small.

In the future, it will be interesting to explore more complex channel geometries with equipment that allows the control of the flow ratio between the inlet(s) and outlet(s) to make the comparison with the results obtained computationally more accurate. Hypocycloids (deltoids, astroids, etc.) could be created with channels that combine inlets and outlets of the same flowrates, while oval, ellipsoidal and crescent shapes could be created with cross-shaped channels where the inlets and outlets have different flowrates.

Chapter VI

Concluding remarks and recommendations for future work

6.1. Concluding remarks

6.1.1. Dissertation synopsis

Emulsions are present in many aspects of our day-to-day life. Due to their broad range of applications (pharmaceutical industry, food industry, oil recovery, etc.), many authors have conducted research related to the topic. Prior research has often been experimental, while theoretical research has typically been with simple geometries (e.g. straight tubes) or approximate methods. In this dissertation, a boundary-integral (BI) algorithm was used to describe the dynamics of a 3D viscous drop in more complex channel geometries that represent microfluidic channels, membrane pores, and other confined geometries. Combining the boundary-integral method (BIM) with a moving-frame (MF) technique (Zinchenko et al., 2012), it was possible to perform simulations of high accuracy at low computational cost. In this chapter, a summary of the conclusions reached in each study is presented.

The moving-frame, boundary-integral algorithm presented in this dissertation has been shown to be effective in determining the motion and deformation of a viscous deformable 3D drop in different microchannels. Unlike other methods, the algorithm allows us to work with complex geometries (both two- and three-dimensional), including junctions and constrictions, without losing any mesh quality. It has also been demonstrated as a powerful tool to accurately predict breakup of confined drops due to the nature of the channel (drop-wall contact) and the fluid

properties (interfacial tension, viscosity), with forces acting on the drop to produce elongation and later breakup.

The results presented in the previous chapters can be used in the design and fabrication of microfluidics when it is necessary to control the drop path and breakup (i.e. drug delivery in the pharmaceutical industry, oil recovery, etc.); in premix membrane emulsification, when it is important to define and predict the properties (drop size and distribution) of an emulsion (i.e. food industry, pharmaceutical industry); or to predict and control a drop can achieve in order for the emulsion to obtain specific properties and functionality, with applications in the food and pharmaceutical industries, amongst others.

6.1.2. Drops in a T-shaped microchannel

In Chapter 2, it was demonstrated that the moving-frame, boundary-integral algorithm is effective in describing the motion and deformation of a 3D viscous drop in a T-shaped microchannel. The dynamics of drop neck thinning just prior breakup was successfully compared with the local, self-similar solution of Lister & Stone (1998). Although the algorithm was formulated for $Re << 1$, it was shown to apply at much higher Reynolds numbers of $Re \sim 10$ (and, approximately, even for $Re = 30$).

In the principal study, a drop was placed in one of the lateral arms of the channel and, depending on the flow ratio Q_1/Q_2 between the stem branch and the other lateral branch, it may either continue straight, be diverted into the stem, or break due to the contact with the corner of the channel. In case of breakup, the size of the daughter droplets going into each branch was calculated. The interaction between the drop and the corner of the channel was strong, so it was necessary to "smooth" (divide into small panels) the corner to provide a lubrication layer that

allowed the simulations to proceed further. A parametric study was performed with the drop physical properties. When the relative radius of the drop was small, the drop was more likely to avoid contact with the corner and go through one of the branches without breaking. For small capillary numbers, the drop did not deform much, so it did not wrap around the corner and was able to leave the channel without breaking. A drop with different viscosity than the bulk fluid also deformed less, so, again, it was more likely to go through one of the branches without breaking.

6.1.3. Drops passing through narrow pores

In Chapter 3, the moving-frame, boundary-integral algorithm was used to predict whether a drop would break or not when passing through a narrow pore, depending on its initial position, fluid properties, and the pore geometry. Three different geometries were studied: Y-bifurcation, and H and circular constriction-pore networks. Three different outcomes were observed: when the drop goes through the pore without breaking, when it breaks due to encountering a bifurcation/corner (direct breakup), and when it breaks due to elongation (indirect breakup).

For the Y-bifurcation geometry, drops with initial positions close to the center of the pore break due to the interaction with the corner of the bifurcation, regardless of the physical properties of the drop. Direct breakup was not observed for droplets in the H and circular constricted-pore networks, due to the absence of interaction with sharp corners. Indirect breakup (due to elongation and then neck thinning with capillary pinch off) was observed in Y-bifurcations and H-constricted pores for drops with starting positions close to the upper and lower walls of the membrane reservoirs. Little or no breakup was observed in the circular-constriction because of the smooth nature of this kind of pore, which allowed the drop to deform gradually and go back to a compact shape again.

For the Y-bifurcation, geometry the post-pore size distribution was calculated. Large drops broke into a broad distribution of daughter sizes, but below a critical size (identified in the study) no breakup was observed. It could be concluded from the study that a narrow distribution of small drops near the critical size can be expected after passing an emulsion with large drops through many pores, or through a membrane or a packed bed multiple times, as has been observed in practice (Nazir et al., 2013; G. T. Vladisavljević et al., 2004).

6.1.4. Drops in 3D channels

In Chapter 4, a novel technique to characterize drop motion in three-dimensional microchannels was presented. A new method - partially based on the Monte Carlo discretization method for complex geometries - was introduced, followed by a triangular tessellation to create the mesh for the front and back channel walls, which are used as boundaries in the boundary-integral algorithm to calculate the flow inside the geometry. The analytical solution of Boussinesq (1868) for the undisturbed flow in rectangular channels was used at the entrance(s) and exit(s) of the channel. This approach allowed for calculation of the undisturbed flow field throughout a complex channel, which was then applied on the boundaries of a moving frame to follow the drop motion and deformation.

The new, fully 3D algorithm (i.e. channels with finite depth) was first used to study the effect of the channel depth on the drop velocity in long, straight channels. As expected, it was observed that smaller drops travelled faster than larger drops (which are slowed by viscous stresses when in close contact with the walls). Two competing effects were observed in the motion of large drops nearly filling the channel cross section: the forces exerted by the imposed flow (higher velocities take place at the centerline of shallow channels due to higher velocity gradients across them) and hydrodynamic forces exerted by the channel walls that slowed down the drops. As a

result, the maximum drop velocity occurred for an intermediate value of the channel aspect ratio (depth over width). Perhaps surprisingly, drops with higher capillary numbers achieved higher velocities due to the shape they acquired: because of viscous forces, they became more elongated and so the drop-wall clearance was larger and the friction drag coefficient exerted by the surrounding fluid was smaller.

Next, the effects of channel depth on drop motion and potential breakup in Y-channels was investigated using the 3D code. Results showed how the drop partition ratio is affected by the channel non-dimensional depth when the flow going through each branch of the bifurcation is considerably different. The size of the drop going through the branch with larger flow increases with the channel aspect ratio.

6.1.5. Experimental work

In Chapter 5, experiments performed at the University of New South Wales (UNSW) in the laboratory of Professor Patrick Spicer are presented. The boundary-integral algorithm was used to compare the simulated drop motion and deformation inside a T-shaped channel and a cross-shaped channel with the microvideo observations of the experiments.

In the case of the T-shaped channel, the drop shape evolutions for the infinite- and finite-depth channel simulations differ, due to the effect of the front and back walls of the channel, with the finite-depth channel simulations showing better agreement with the experiments. For the finite-depth channel simulations, the drop experienced more deformation, before, during and after going through the T-junction, while in the infinite-depth simulations the drop kept a more compact shape during the whole process. However, when the capillary number is defined used the maximum velocity of the fluid velocity instead of its average velocity, the drop deformation in the simulations for a channel with infinite depth is similar to the deformation observed in the experimental results.

In the experiments, the drop velocity was slowed down by the presence of other drops, so it took longer for it to pass through the T-junction; otherwise, its shape evolution during passage through the junction was found to be very similar to the predictions of the finite-depth simulations.

In the case of the cross-shaped channel, the flow in each of the branches was the same and the drop shape evolution was similar for all three cases (experiments, infinite-depth channel simulations and finite-depth channel simulations). In the simulation with a channel of infinite depth, the drop experienced less stretching (shorter and more regular neck, and more rounded lobes), when compared to the finite-depth channel frames. Again, the rate of drop deformation was most similar for the experiments and the finite-depth channel simulations, because of the effect of the front and back walls of the channel. However, if the maximum fluid velocity is included in the capillary number, the motion and deformation of the drop in the infinite-depth channel and in the experiments become even more similar. Overall, good agreement was found between the experiments and the simulations.

6.2. Suggestions for future work

One area for future work is the development of an algorithm, compatible with the moving-frame boundary-integral algorithm presented in this work, which is able to describe drop breakup. A drop fragmentation algorithm (Zinchenko & Davis, 2013) would be useful to demonstrate that, indeed, the parent drop breaks and the daughter drops could be followed for a few time steps after that moment. To follow the daughter drops for longer times, it would be necessary to increase the moving frame size (which would defeat its purpose) or divide the moving frame in as many parts as daughter droplets formed.

Future studies could also include simulations with curved geometries, as commonly found in nature. Another development would be to recast the simulations in terms of a prescribed pressure drop, rather than prescribing the flow rates at the entrance(s) and exit(s). Amongst other applications, this work would be useful in medical research related to drug release.

Another interesting study would consist of having large drops in constricted channels. Depending on the drop physical properties, a fourth outcome besides the three observed in Chapter 3 would be expected: drop trapping. Being able to predict the conditions under which the drop would not be able to go through the constriction and would obstruct the membrane pore would be very useful to predict membrane fouling.

It would also be interesting to design experiments to observe drop behavior in different situations that could be easily reproduced with the boundary-integral algorithm to compare the experimental and the numerical results. To obtain different drop shapes, hypocycloids (deltoids, astroids, etc.) could be created with channels that combine inlets and outlets of the same flowrates, while oval, ellipsoidal and crescent shapes could be created with cross-shaped channels where the inlets and outlets have different flowrates. Following the work of Professor Spicer (Caggioni et al., 2018; J. Song et al., 2019; H. Wang et al., 2018), the shapes could potentially be "frozen" using complex fluids that crystallize with subtle changes in temperature or shear. An undergraduate student and I did simulations with the 2D code to demonstrate various exotic shapes that could be obtained, but because of the lab and shop closure during the COVID-19 pandemic, we were unable to implement experiments to observe these shapes.

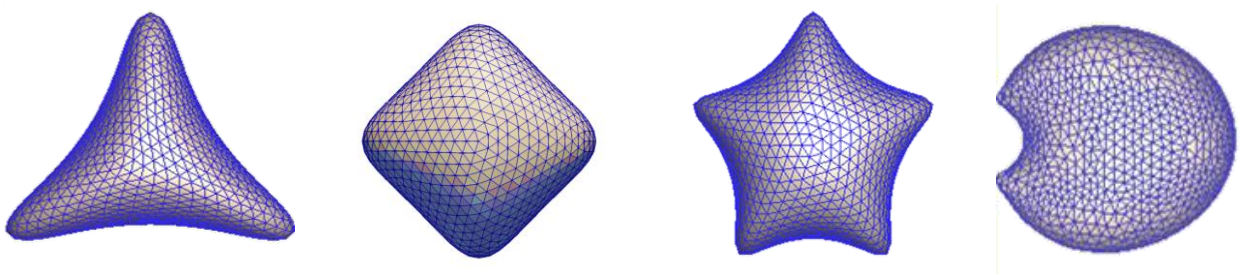

Figure 6.1. Example drop shapes achieved by boundary-integral simulations.

Bibliography

Abbas, S., da Wei, C., Hayat, K., & Xiaoming, Z. (2012). Ascorbic acid: microencapsulation techniques and trends - A review. *Food Reviews International*, *28*(4), 343–374. https://doi.org/10.1080/87559129.2011.635390

Adams, F., & Walstra, P. (1998). *Modern Aspects of Emulsion Science* (B. P. Binks (Ed.)). Royal Society of Chemistry, Information Services.

Agustin Suarez, J., & Veza, J. M. (2000). Dead-end microfiltration as advanced treatment for wastewater. *Desalination*, *127*(1), 47–58. https://doi.org/10.1016/S0011-9164(99)00191-5

Allen, T. M., & Cullis, P. R. (2004). Drug delivery systems: entering the mainstream. *Science*, *303*(5665), 1818–1822. https://doi.org/10.1126/science.1095833

Alliod, O., Almouazen, E., Nemer, G., Fessi, H., & Charcosset, C. (2019). Comparison of three processes for parenteral nanoemulsion production: ultrasounds, microfluidizer, and premix membrane emulsification. *Journal of Pharmaceutical Sciences*, *108*(8), 2708–2717. https://doi.org/10.1016/j.xphs.2019.03.026

Apel, P. (2001). Track etching technique in membrane technology. *Radiation Measurements*, *34*(1–6), 559–566. https://doi.org/10.1016/S1350-4487(01)00228-1

Barber, J. O., Alberding, J. P., Restrepo, J. M., & Secomb, T. W. (2008). Simulated two-dimensional red blood cell motion, deformation, and partitioning in microvessel bifurcations. *Annals of Biomedical Engineering*, *36*(10), 1690–1698. https://doi.org/10.1007/s10439-008-9546-4

Barnocky, G., & Davis, R. H. (1989). The lubrication force between spherical drops, bubbles and rigid particles in a viscous fluid. *International Journal of Multiphase Flow*, *15*(4), 627–638.

https://doi.org/10.1016/0301-9322(89)90057-8

Baroud, C. N., Gallaire, F., & Emi Dangla, R. (2010). Dynamics of microfluidic droplets. *Lab on a Chip*, *10*, 2032–2045. https://doi.org/10.1039/c001191f

Barthes-Biesel, D., & Acrivos, A. (1972). Deformation and burst of a liquid droplet freely suspended in a linear shear field. *J. Fluid Mech*, *61*(1), 1–21. https://doi.org/10.1017/S0022112073000534

Becher, P. (1965). *Emulsions: Theory and Practice*. American Chemical Society.

Bhardwaj, S., Dalal, A., Biswas, G., & Mukherjee, P. P. (2018). Analysis of droplet dynamics in a partially obstructed confinement in a three-dimensional channel. *Physics of Fluids*, *30*(10), 102102. https://doi.org/10.1063/1.5030738

Blake, J. R. (1971). A note on the image system for a stokeslet in a no-slip boundary. *Mathematical Proceedings of the Cambridge Philosophical Society*, *70*(2), 303–310. https://doi.org/10.1017/S0305004100049902

Bobra, M. (1990). A study of the formation of water-in-oil emulsions. *Proceedings of the Thirteenth Arctic and Marine Oilspill Program Technical Seminar*, 6–8.

Boussinesq, Joseph. (1868). Mémoire sur l'influence des frottements dans les mouvements réguliers des fluids. *Journal de Mathématiques Pures et Appliquées*, *13.2*(3), 377–424.

Caggioni, M., Traini, D., Young, P. M., & Spicer, P. T. (2018). Microfluidic production of endoskeleton droplets with controlled size and shape. *Powder Technology*, *329*, 129–136. https://doi.org/10.1016/j.powtec.2018.01.050

Carlson, A., Do-Quang, M., & Amberg, G. (2010). Droplet dynamics in a bifurcating channel. *International Journal of Multiphase Flow*, *36*(5), 397–405. https://doi.org/10.1016/j.ijmultiphaseflow.2010.01.002

Carroll, R. M., & Gupta, N. R. (2014). Inertial and surfactant effects on the steady droplet flow in cylindrical channels. *Physics of Fluids*, *26*(12), 122102. https://doi.org/10.1063/1.4902902

Casadevall i Solvas, X., & De Mello, A. (2011). Droplet microfluidics: recent developments and future applications. *Chemical Communications*, *47*(7), 1936–1942. https://doi.org/10.1039/c0cc02474k

Champion, J. A., Katare, Y. K., & Mitragotri, S. (2007). Particle shape: a new design parameter for micro- and nanoscale drug delivery carriers. *Journal of Controlled Release*, *121*(1–2), 3–9. https://doi.org/10.1016/j.jconrel.2007.03.022

Charcosset, C. (2009). Preparation of emulsions and particles by membrane emulsification for the food processing industry. *Journal of Food Engineering*, *92*(3), 241–249. https://doi.org/10.1016/j.jfoodeng.2008.11.017

Charcosset, C. (2012). Membranes for the preparation of emulsions and particles. *Membrane Processes in Biotechnology and Pharmaceutics*. https://doi.org/10.1016/b978-0-444-56334-7.00006-x

Chen, X., Xue, C., Zhang, L., Hu, G., Jiang, X., & Sun, J. (2014). Inertial migration of deformable droplets in a microchannel. *Physics of Fluids*, *26*(11), 112003. https://doi.org/10.1063/1.4901884

Chen, Y., & Deng, Z. (2017). Hydrodynamics of a droplet passing through a microfluidic T-junction. *Journal of Fluid Mechanics*, *819*, 401–434. https://doi.org/10.1017/jfm.2017.181

Chou, W. L., Lee, P. Y., Yang, C. L., Huang, W. Y., & Lin, Y. S. (2015). Recent advances in applications of droplet microfluidics. *Micromachines*, *6*(9), 1249–1271. https://doi.org/10.3390/mi6091249

Christopher, G. F.; Anna, S. L. (2007). Microfluidic methods for generating continuous droplet streams. *Journal of Physics D: Applied Physics*, *40*(19). https://iopscience.iop.org/article/10.1088/0022-3727/40/19/R01/meta

Chung, C., Hulsen, M. A., Kim, J. M., Ahn, K. H., & Lee, S. J. (2008). Numerical study on the effect of viscoelasticity on drop deformation in simple shear and 5:1:5 planar contraction/expansion microchannel. *Journal of Non-Newtonian Fluid Mechanics*, *155*(1–2), 80–93. https://doi.org/10.1016/j.jnnfm.2008.06.002

Chung, C., Lee, M., Char, K., Ahn, K. H., & Lee, S. J. (2010). Droplet dynamics passing through obstructions in confined microchannel flow. *Microfluidics and Nanofluidics*, *9*(6), 1151–1163. https://doi.org/10.1007/s10404-010-0636-x

Ciurans Oset, M., Nordin, J., & Akhtar, F. (2018). Processing of macroporous alumina ceramics using pre-expanded polymer microspheres as sacrificial template. *Ceramics*, *1*(2), 329–342. https://doi.org/10.3390/ceramics1020026

Cobos, S., Carvalho, M. S., & Alvarado, V. (2009). Flow of oil-water emulsions through a constricted capillary. *International Journal of Multiphase Flow*, *35*(6), 507–515. https://doi.org/10.1016/j.ijmultiphaseflow.2009.02.018

Cristini, V., Blawzdziewicz, J., & Loewenberg, M. (2001). An adaptive mesh algorithm for evolving surfaces: simulations of drop breakup and coalescence. *Journal of Computational Physics*, *168*(2), 445–463. https://doi.org/10.1006/jcph.2001.6713

Cristini, V., & Tan, Y.-C. (2004). Theory and numerical simulation of droplet dynamics in complex flows - a review. *The Royal Society of Chemistry*, *4*, 257–264. https://doi.org/10.1039/b403226h

Davis, R. H. (2019). Microfiltration in pharmaceutics and biotechnology. In A. Basile & C.

Charcosset (Eds.), *Current Trends and Future Developments on (Bio-) Membranes: Membrane Processes in the Pharmaceutical and Biotechnological Field* (pp. 29–67). Elsevier. https://doi.org/10.1016/B978-0-12-813606-5.00002-6

Davis, R. H., & Zinchenko, A. Z. (2009). Motion of deformable drops through granular media and other confined geometries. *Journal of Colloid and Interface Science*, *334*(2), 113–123. https://doi.org/10.1016/j.jcis.2009.02.062

Desai, K. G. H., & Jin Park, H. (2005). Recent developments in microencapsulation of food ingredients. *Drying Technology*, *23*(7), 1361–1394. https://doi.org/10.1081/DRT-200063478

Dhakal, S. P., & He, J. (2020). Microencapsulation of vitamins in food applications to prevent losses in processing and storage: a review. *Food Research International*, *137*, 109326. https://doi.org/10.1016/j.foodres.2020.109326

Dressler, O. J., Maceiczyk, R. M., Chang, S. I., & Demello, A. J. (2014). Droplet-based microfluidics: enabling impact on drug discovery. *Journal of Biomolecular Screening*, *19*(4), 483–496. https://doi.org/10.1177/1087057113510401

Eisinaite, V., Juraite, D., Schroën, K., & Leskauskaite, D. (2016). Preparation of stable food-grade double emulsions with a hybrid premix membrane emulsification system. *Food Chemistry*, *206*, 59–66. https://doi.org/10.1016/j.foodchem.2016.03.046

Fingas, M, Fieldhouse, B., Bobra, M., & Tennyson, E. (1993). *The Physics and Chemistry of Emulsions*.

Fingas, Merv. (1995). Water-in-oil emulsion formation: a review of physics and mathematical modelling. *Spill Science and Technology Bulletin*, *2*(1), 55–59. https://doi.org/10.1016/1353-2561(95)94483-Z

Gañán-Calvo, A. M. (1998). Generation of steady liquid microthreads and micron-sized monodisperse sprays in gas streams. *Physical Review Letters*, *80*(2), 285–288. https://doi.org/10.1103/PhysRevLett.80.285

Gehrmann, S., & Bunjes, H. (2017). Preparation of nanoemulsions by premix membrane emulsification: which parameters have a significant influence on the resulting particle size? *Journal of Pharmaceutical Sciences*, *106*(8), 2068–2076. https://doi.org/10.1016/j.xphs.2017.04.066

Giorno, L., De Luca, G., Figoli, A., Piacentini, E., & Drioli, E. (2009). Membrane emulsification: principles and applications. In E. Drioli & L. Giorno (Eds.), *Membrane Operations* (pp. 463–497). Wiley-VCH Verlag GmbH & Co. KGaA. https://doi.org/10.1002/9783527626779.ch21

Gissinger, J. R., Zinchenko, A. Z., & Davis, R. H. (2019). Drops with insoluble surfactant squeezing through interparticle constrictions. *Journal of Fluid Mechanics*, *878*, 324–355. https://doi.org/10.1017/jfm.2019.678

Glotzer, S. C., & Solomon, M. J. (2007). Anisotropy of building blocks and their assembly into complex structures. *Nature Materials*, *6*(8), 557–562. https://doi.org/10.1038/nmat1949

Griggs, A. J., Zinchenko, A. Z., & Davis, R. H. (2007). Low-Reynolds-number motion of a deformable drop between two parallel plane walls. *International Journal of Multiphase Flow*, *33*(2), 182–206. https://doi.org/10.1016/j.ijmultiphaseflow.2006.06.012

Guido, S., & Preziosi, V. (2010). Droplet deformation under confined Poiseuille flow. *Advances in Colloid and Interface Science*, *161*(1–2), 89–101. https://doi.org/10.1016/j.cis.2010.04.005

Günther, A., & Jensen, K. F. (2006). Multiphase microfluidics: from flow characteristics to

chemical and materials synthesis. *Lab on a Chip*, *6*, 1487–1503. https://doi.org/10.1039/b609851g

Haan, A. B., & Bosch, H. (2013). *Industrial separation processes: Fundamentals*. https://www.worldcat.org/title/industrial-separation-processes-fundamentals/oclc/824608909

Haber, S., Hetsroni, G., & Solan, A. (1973). On the low Reynolds number motion of two droplets. *International Journal of Multiphase Flow*, *1*(1), 57–71. https://doi.org/10.1016/0301-9322(73)90004-9

He, M., Kuo, J. S., & Chiu, D. T. (2005). Electro-generation of single femtoliter- and picoliter-volume aqueous droplets in microfluidic systems. *Applied Physics Letters*, *87*(3), 031916. https://doi.org/10.1063/1.1997280

Hebeker, F.-K. (1986). Efficient boundary element methods for three-dimensional exterior viscous flows. *Numerical Methods for Partial Differential Equations*, *2*(4), 273–297. https://doi.org/10.1002/num.1690020404

Hetsroni, G., Haber, S., & Wacholder, E. (1970). The flow fields in and around a droplet moving axially within a tube. *Journal of Fluid Mechanics*, *41*(4), 689–705. https://doi.org/10.1017/S0022112070000848

Higdon, J. J. L., & Muldowney, G. P. (1970). A spectral boundary element approach for the three dimensional Stokes equations applied to free surface flows. *WIT Transactions on Modelling and Simulation*, *10*. https://doi.org/10.2495/BE950661

Ho, B. P., & Leal, L. G. (1975). The creeping motion of liquid drops through a circular tube of comparable diameter. *Journal of Fluid Mechanics*, *71*(2), 361–383. https://doi.org/10.1017/S0022112075002625

Hoang, D. A., Portela, L. M., Kleijn, C. R., Kreutzer, M. T., & Steijn, V. Van. (2013). Dynamics of droplet breakup in a t-junction. *Journal of Fluid Mechanics*, *717*. https://doi.org/10.1017/jfm.2013.18

Hoang, Duong A., van Steijn, V., Portela, L. M., Kreutzer, M. T., & Kleijn, C. R. (2013). Benchmark numerical simulations of segmented two-phase flows in microchannels using the Volume of Fluid method. *Computers and Fluids*, *86*, 28–36. https://doi.org/10.1016/j.compfluid.2013.06.024

Hoang, V. T., Lim, J., Byon, C., & Park, J. M. (2018). Three-dimensional simulation of droplet dynamics in planar contraction microchannel. *Chemical Engineering Science*, *176*, 59–65. https://doi.org/10.1016/j.ces.2017.10.020

Hodges, S. R., Jensen, O. E., & Rallison, J. M. (2004). The motion of a viscous drop through a cylindrical tube. *Journal of Fluid Mechanics*, *501*, 279–301. https://doi.org/10.1017/S0022112003007213

Holzapfel, S., Rondeau, E., Mühlich, P., & Windhab, E. J. (2013). Drop detachment from a micro-engineered membrane surface in a dynamic membrane emulsification process. *Chemical Engineering & Technology*, *36*(10), 1785–1794. https://doi.org/10.1002/ceat.201300256

Hsieh, D. S. T., Rhine, W. D., & Langer, R. (1983). Zero-order controlled-release polymer matrices for micro- and macromolecules. *Journal of Pharmaceutical Sciences*, *72*(1), 17–22. https://doi.org/10.1002/jps.2600720105

Huang, J. S., & Varadaraj, R. (1996). Colloid and interface science in the oil industry. *Current Opinion in Colloid & Interface Science*, *1*(4), 535–539. https://doi.org/10.1016/S1359-0294(96)80124-5

Huisman, I. H. (2000). Membrane separations | Microfiltration. In *Encyclopedia of Separation Science*. https://doi.org/10.1016/b0-12-226770-2/05251-0

Jakiela, S., Makulska, S., Korczyk, P. M., & Garstecki, P. (2011). Speed of flow of individual droplets in microfluidic channels as a function of the capillary number, volume of droplets and contrast of viscosities. *Lab on a Chip*, *11*(21), 3603–3608. https://doi.org/10.1039/c1lc20534j

Janssen, P. J. A., & Anderson, P. D. (2008). A boundary-integral model for drop deformation between two parallel plates with non-unit viscosity ratio drops. *Journal of Computational Physics*, *227*(20), 8807–8819. https://doi.org/10.1016/j.jcp.2008.06.027

Joscelyne, S. M., & Trägårdh, G. (2000). Membrane emulsification - A literature review. *Journal of Membrane Science*, *169*(1), 107–117. https://doi.org/10.1016/S0376-7388(99)00334-8

Jose, B. M., & Cubaud, T. (2014). Formation and dynamics of partially wetting droplets in square microchannels. *The Royal Society of Chemistry*, *4*, 14962–14970. https://doi.org/10.1039/c4ra00654b

Joseph, S., & Bunjes, H. (2012). Preparation of nanoemulsions and solid lipid nanoparticles by premix membrane emulsification. *Journal of Pharmaceutical Sciences*, *101*(7), 2479–2489. https://doi.org/10.1002/jps.23163

Jullien, M. C., Tsang Mui Ching, M. J., Cohen, C., Menetrier, L., & Tabeling, P. (2009). Droplet breakup in microfluidic T-junctions at small capillary numbers. *Physics of Fluids*, *21*(7), 072001. https://doi.org/10.1063/1.3170983

Kaade, W., Güell, C., Ballon, A., Mellado-Carretero, J., De Lamo-Castellví, S., & Ferrando, M. (2020). Dynamic membranes of tunable pore size for lemon oil encapsulation. *LWT*, *123*. https://doi.org/10.1016/j.lwt.2020.109090

Kawakatsu, T., Kikuchi, Y., & Nakajima, M. (1997). Regular-sized cell creation in microchannel emulsification by visual microprocessing method. *Journal of the American Oil Chemists' Society*, *74*(3), 317–321. https://doi.org/10.1007/s11746-997-0143-8

Khan, B. A., Akhtar, N., Muhammad, H., Khan, S., Waseem, K., Mahmood, T., Rasul, A., Iqbal, M., & Khan, H. (2011). Basics of pharmaceutical emulsions: a review. *African Journal of Pharmacy and Pharmacology*, *5*(25), 2715–2725. https://doi.org/10.5897/AJPP11.698

Kim, J., & Vanapalli, S. A. (2013). Microfluidic production of spherical and nonspherical fat particles by thermal quenching of crystallizable oils. *Langmuir*, *29*(39), 12307–12316. https://doi.org/10.1021/la401338m

Labrot, V., Schindler, M., Guillot, P., Collin, A., & Joanicot, M. (2009). Extracting the hydrodynamic resistance of droplets from their behavior in microchannel networks. *Biomicrofluidics*, *3*(1), 012804. https://doi.org/10.1063/1.3109686

Lac, E., & Sherwood, J. D. (2009). Motion of a drop along the centreline of a capillary in a pressure-driven flow. *Journal of Fluid Mechanics*, *640*, 27–54. https://doi.org/10.1017/S0022112009991212

Leal-Calderon, F., Schmitt, V., & Bibette, J. (2007). *Emulsion Science: Basic Principles* (F. Leal-Calderon, V. Schmitt, & J. Bibette (Eds.); Second Edition). Springer Science+Business Media, LLC.

Leal-Calderon, F., Thivilliers, F., & Schmitt, V. (2007). Structured emulsions. *Current Opinion in Colloid and Interface Science*, *12*(4–5), 206–212. https://doi.org/10.1016/j.cocis.2007.07.003

Lepercq-Bost, É., Giorgi, M. L., Isambert, A., & Arnaud, C. (2008). Use of the capillary number for the prediction of droplet size in membrane emulsification. *Journal of Membrane*

Science, *314*(1–2), 76–89. https://doi.org/10.1016/j.memsci.2008.01.023

Leshansky, M. A., & Pismen, M. L. (2009). Breakup of drops in a microfluidic T junction. *Physics of Fluids*, *21*(2), 023303. https://doi.org/10.1063/1.3078515

Levan, M. D. (1981). Motion of a droplet with a newtonian interface. *Journal of Colloid And Interface Science*, *83*(1), 11–17. https://doi.org/10.1016/0021-9797(81)90003-5

Li, M., Liu, Z., Pang, Y., Yan, C., Wang, J., Zhao, S., & Zhou, Q. (2020). Flow topology and its transformation inside droplets traveling in rectangular microchannels. *Physics of Fluids*, *32*(5), 052009. https://doi.org/10.1063/5.0004549

Liang, M., Yang, S., Miao, T., & Yu, B. (2015). Minimum applied pressure for a drop through an abruptly constricted capillary. *Microfluidics and Nanofluidics*, *19*(1), 1–8. https://doi.org/10.1007/s10404-014-1541-5

Link, D. R., Anna, S. L., Weitz, D. A., & Stone, H. A. (2004). Geometrically mediated breakup of drops in microfluidic devices. *Physical Review Letters*, *92*(5), 4. https://doi.org/10.1103/PhysRevLett.92.054503

Liron, N., & Mochon, S. (1976). Stokes flow for a stokeslet between two parallel flat plates. *Journal of Engineering Mathematics*, *10*(4), 287–303. https://doi.org/10.1007/BF01535565

Lister, J. R., & Stone, H. A. (1998). Capillary breakup of a viscous thread surrounded by another viscous fluid. *Physics of Fluids*, *10*(11), 2758–2764. http://ojps.aip.org/phf/phfcr.jsp

Liu, W., Yang, X. L., & Winston Ho, W. S. (2011). Preparation of uniform-sized multiple emulsions and micro/nano particulates for drug delivery by membrane emulsification. *Journal of Pharmaceutical Sciences*, *100*(1), 75–93. https://doi.org/10.1002/jps.22272

Lorenz, R. M., Edgar, J. S., Jeffries, G. D. M., & Chiu, D. T. (2006). Microfluidic and optical systems for the on-demand generation and manipulation of single femtoliter-volume

aqueous droplets. *Analytical Chemistry*, *78*(18), 6433–6439. https://doi.org/10.1021/ac060748l

Ma, S., Sherwood, J. M., Huck, W. T. S., & Balabani, S. (2014). On the flow topology inside droplets moving in rectangular microchannels. *Lab on a Chip*, *14*(18), 3611–3620. https://doi.org/10.1039/c4lc00671b

Maan, A. A., Nazir, A., Khan, M. K. I., Boom, R., & Schroën, K. (2015). Microfluidic emulsification in food processing. *Journal of Food Engineering*, *147*, 1–7. https://doi.org/10.1016/j.jfoodeng.2014.09.021

Maciejko, R., Goano, M., & Abou-Khalil, M. (1995). Memory-efficient technique for inclusion of carrier degeneracy in Monte Carlo transport simulation. *Electronics Letters*, *31*(17), 1516–1517.

Maristany, A. (2019). *Droplet motion through membrane pores*. University of Colorado.

Martinez, M. J., & Udell, K. S. (1990). Axisymmetric creeping motion of drops through circular tubes. *Journal of Fluid Mechanics*, *210*(565), 565–591. https://doi.org/10.1017/S0022112090001409

Martinez, M. J., & Udell, K. S. (2008). Axisymmetric creeping motion of drops through a periodically constricted tube. *AIP Conference Proceedings*, *197*(1), 222–234. https://doi.org/10.1063/1.38959

Mashaghi, S., Abbaspourrad, A., Weitz, D. A., & van Oijen, A. M. (2016). Droplet microfluidics: A tool for biology, chemistry and nanotechnology. *TrAC - Trends in Analytical Chemistry*, *82*, 118–125. https://doi.org/10.1016/j.trac.2016.05.019

Mason, T. G., & Bibette, J. (1997). Shear rupturing of droplets in complex fluids. *Langmuir*, *13*(17), 4600–4613. https://doi.org/10.1021/la9700580

Ménétrier-Deremble, L., & Tabeling, P. (2006). Droplet breakup in microfluidic junctions of arbitrary angles. *Physical Review E - Statistical, Nonlinear, and Soft Matter Physics*, *74*(3), 035303. https://doi.org/10.1103/PhysRevE.74.035303

Metropolis, N., & Ulam, S. (1949). The Monte Carlo Method. *Journal of the American Statistical Association*, *44*(247), 335–341. https://doi.org/10.1080/01621459.1949.10483310

Moritz, T., Benfer, S., Árki, P., & Tomandl, G. (2001). Influence of the surface charge on the permeate flux in the dead-end filtration with ceramic membranes. *Separation and Purification Technology*, *25*(1–3), 501–508. https://doi.org/10.1016/S1383-5866(01)00080-6

Mosler, A. B., & Shaqfeh, E. S. G. (1997). Drop breakup in the flow through fixed beds via stochastic simulation in model Gaussian fields. *Physics of Fluids*, *9*(11), 3209–3226. https://doi.org/10.1063/1.869437

Muschiolik, G. (2007). Multiple emulsions for food use. *Current Opinion in Colloid & Interface Science*, *12*(4–5), 213–220. https://doi.org/10.1016/j.cocis.2007.07.006

Myers, F. B., & Lee, L. P. (2008). Innovations in optical microfluidic technologies for point-of-care diagnostics. *Lab on a Chip*, *8*(12), 2015–2031. https://doi.org/10.1039/b812343h

Nagy, E. (2018). Basic equations of mass transport through a membrane layer. In *Basic Equations of Mass Transport through a Membrane Layer* (Second Ed). Elsevier. https://doi.org/10.1016/C2016-0-04043-3

Nakano, M. (2000). Places of emulsions in drug delivery. *Advanced Drug Delivery Reviews*, *45*, 1–4. www.elsevier.com/locate/drugdeliv

Nakashima, T., Shimizu, M., & Kukizaki, M. (2000). Particle control of emulsion by membrane

emulsification and its applications. *Advanced Drug Delivery Reviews*, *45*(1), 47–56. https://doi.org/10.1016/S0169-409X(00)00099-5

Navarro, R., Zinchenko, A. Z., & Davis, R. H. (2020). Boundary-integral study of a freely suspended drop in a T-shaped microchannel. *International Journal of Multiphase Flow*, 103379. https://doi.org/10.1016/j.ijmultiphaseflow.2020.103379

Nazir, A., Boom, R. M., & Schroën, K. (2013). Droplet break-up mechanism in premix emulsification using packed beds. *Chemical Engineering Science*, *92*, 190–197. https://doi.org/10.1016/j.ces.2013.01.021

Nazir, A., Schroën, K., & Boom, R. (2010). Premix emulsification: a review. *Journal of Membrane Science*, *362*(1–2), 1–11. https://doi.org/10.1016/j.memsci.2010.06.044

Nekouei, M., & Vanapalli, S. A. (2017). Volume-of-fluid simulations in microfluidic T-junction devices: Influence of viscosity ratio on droplet size. *Physics of Fluids*, *29*(3), 032007. https://doi.org/10.1063/1.4978801

Nemer, M. B. (2004). *Near-contact motion of liquid drops in emulsions and foams*. Yale University.

Nemer, M. B., Chen, X., Papadopoulos, D. H., Bławzdziewicz, J., & Loewenberg, M. (2004). Hindered and enhanced coalescence of drops in Stokes flows. *Physical Review Letters*, *92*(11), 114501. https://doi.org/10.1103/PhysRevLett.92.114501

Nguyen, N. T., Wereley, S. T., & Shaegh, S. A. M. (2019). *Fundamentals and Applications of Microfluidics* (Third Ed). Artech House.

Nishihora, R. K., Luhede, L., Fritsching, U., Novy Quadri, M. G., Hotza, D., Rezwan, K., & Wilhelm, M. (2020). Premix membrane emulsification using flat microfiltration inorganic membranes with tailored structure and composition. *Journal of Membrane Science*, *608*,

118124. https://doi.org/10.1016/j.memsci.2020.118124

Nisisako, T., Torii, T., & Higuchi, T. (2002). Droplet formation in a microchannel network. *Lab on a Chip*, *2*(1), 24–26. https://doi.org/10.1039/b108740c

Nourbakhsh, A., Mortazavi, S., & Afshar, Y. (2011). Three-dimensional numerical simulation of drops suspended in Poiseuille flow at non-zero Reynolds numbers. *Physics of Fluids*, *23*(12), 123303. https://doi.org/10.1063/1.3663565

Olbricht, W. L., & Leal, L. G. (1982). The creeping motion of liquid drops through a circular tube of comparable diameter: the effect of density differences between the fluids. *Journal of Fluid Mechanics*, *115*, 187–216. https://doi.org/10.1017/S0022112082000718

Pan, F. Y., & Acrivos, A. (1968). Shape of a drop or bubble at low Reynolds number. *Industrial and Engineering Chemistry Fundamentals*, *7*(2), 227–232. https://pubs.acs.org/sharingguidelines

Patel, P. D., Shaqfeh, E. S. G., Butler, J. E., Cristini, V., Bławzdziewicz, J., & Loewenberg, M. (2003). Drop breakup in the flow through fixed fiber beds: an experimental and computational investigation. *Physics of Fluids*, *15*(5), 1146–1157. https://doi.org/10.1063/1.1557051

Piacentini, E., Drioli, E., & Giorno, L. (2014). Membrane emulsification technology: twenty-five years of inventions and research through patent survey. *Journal of Membrane Science*, *468*, 410–422. https://doi.org/10.1016/j.memsci.2014.05.059

Pozrikidis, C. (1992). *Boundary Integral and Singularity Methods for Linearized Viscous Flow*. Cambridge University Press. https://doi.org/10.1017/CBO9780511624124

Raj, Richa, Mathur, N., & Buwa, V. V. (2010). Numerical simulations of liquid-liquid flows in microchannels. *Industrial and Engineering Chemistry Research*, *49*(21), 10606–10614.

https://doi.org/10.1021/ie100626a

Raj, Rishi, Adera, S., Enright, R., & Wang, E. N. (2014). High-resolution liquid patterns via three-dimensional droplet shape control. *Nature Communications*, *5*(1), 1–8. https://doi.org/10.1038/ncomms5975

Rallison, J. M., & Acrivos, A. (1978). A numerical study of the deformation and burst of a viscous drop in an extensional flow. *Journal of Fluid Mechanics*, *89*(1), 191–200. https://doi.org/10.1017/S0022112078002530

Ramakrishnan, S., Ferrando, M., Aceña-Muñoz, L., De Lamo-Castellví, S., & Güell, C. (2013). Fish oil microcapsules from O/W wmulsions produced by premix membrane emulsification. *Food and Bioprocess Technology*, *6*(11), 3088–3101. https://doi.org/10.1007/s11947-012-0950-2

Rao, S. S., & Wong, H. (2018). The motion of long drops in rectangular microchannels at low capillary numbers. *Journal of Fluid Mechanics*, *852*, 60–104. https://doi.org/10.1017/jfm.2018.521

Ratcliffe, T., & Davis, R. H. (2012). Drop trapping in axisymmetric constrictions with arbitrary contact angle. *Physics of Fluids*, *24*(6), 062102. https://doi.org/10.1063/1.4727922

Ratcliffe, T., Zinchenko, A. Z., & Davis, R. H. (2010). Buoyancy-induced squeezing of a deformable drop through an axisymmetric ring constriction. *Physics of Fluids*, *22*(8), 082101. https://doi.org/10.1063/1.3464343

Ratcliffe, T., Zinchenko, A. Z., & Davis, R. H. (2012). Simulations of gravity-induced trapping of a deformable drop in a three-dimensional constriction. *Journal of Colloid and Interface Science*, *383*(1), 167–176. https://doi.org/10.1016/j.jcis.2012.06.014

Ré, M.-I. (2006). Formulating drug delivery systems by spray drying. *Drying Technology*, *24*(4),

433–446. https://doi.org/10.1080/07373930600611877

Reddy Cherlo, S. K., Kariveti, S., & Pushpavanam, S. (2010). Experimental and numerical investigations of two-phase (liquid-liquid) flow behavior in rectangular microchannels. *Industrial and Engineering Chemistry Research*, *49*(2), 893–899. https://doi.org/10.1021/ie900555e

Roache, P. (1972). *Computational fluid mechanics*. Hermosa Publishers.

Rosenfeld, L., Fan, L., Chen, Y., Swoboda, R., & Tang, S. K. Y. (2014). Break-up of droplets in a concentrated emulsion flowing through a narrow constriction. *Soft Matter*, *10*(3), 421–430. https://doi.org/10.1039/c3sm51843d

Sackmann, E. K., Fulton, A. L., & Beebe, D. J. (2014). The present and future role of microfluidics in biomedical research. *Nature*, *507*(7491), 181–189. https://doi.org/10.1038/nature13118

Sadek, C., Tabuteau, H., Schuck, P., Fallourd, Y., Pradeau, N., Le Floch-Fouéré, C., & Jeantet, R. (2013). Shape, shell, and vacuole formation during the drying of a single concentrated whey protein droplet. *Langmuir*, *29*(50), 15606–15613. https://doi.org/10.1021/la404108v

Sarrazin, F., Bonometti, T., Prat, L., Gourdon, C., & Magnaudet, J. (2008). Hydrodynamic structures of droplets engineered in rectangular micro-channels. *Microfluid Nanofluid*, *5*, 131–137. https://doi.org/10.1007/s10404-007-0233-9

Sarrazin, Flavie, Loubière, K., Prat, L., Gourdon, C., Bonometti, T., & Magnaudet, J. (2006). Experimental and numerical study of droplets hydrodynamics in microchannels. *AIChE Journal*, *52*(12), 4061–4070. https://doi.org/10.1002/aic.11033

Sato, K., Mawatari, K., & Kitamori, T. (2008). Microchip-based cell analysis and clinical diagnosis system. *Lab on a Chip*, *8*(12), 1992–1998. https://doi.org/10.1039/b814098g

Secomb, T. W., Styp-Rekowska, B., & Pries, A. R. (2007). Two-dimensional simulation of red blood cell deformation and lateral migration in microvessels. *Annals of Biomedical Engineering*, *35*(5), 755–765. https://doi.org/10.1007/s10439-007-9275-0

Sekerka, R. F. (2001). Fundamentals of phase field theory. *Advances in Crystal Growth Research*, 21–41. https://doi.org/10.1016/B978-044450747-1/50029-6

Shah, R. K., Shum, H. C., Rowat, A. C., Lee, D., Agresti, J. J., Utada, A. S., Chu, L. Y., Kim, J. W., Fernandez-Nieves, A., Martinez, C. J., & Weitz, D. A. (2008). Designer emulsions using microfluidics. *Materials Today*, *11*(4), 18–27. https://doi.org/10.1016/S1369-7021(08)70053-1

Shewan, H. M., & Stokes, J. R. (2013). Review of techniques to manufacture micro-hydrogel particles for the food industry and their applications. *Journal of Food Engineering*, *119*(4), 781–792. https://doi.org/10.1016/j.jfoodeng.2013.06.046

Shum, H. C., Abate, A. R., Lee, D., Studart, A. R., Wang, B., Chen, C. H., Thiele, J., Shah, R. K., Krummel, A., & Weitz, D. A. (2010). Droplet microfluidics for fabrication of non-spherical particles. *Macromolecular Rapid Communications*, *31*(2), 108–118. https://doi.org/10.1002/marc.200900590

Song, H., Tice, J. D., & Ismagilov, R. F. (2003). A microfluidic system for controlling reaction networks in time. *Angewandte Chemie - International Edition*, *42*(7), 768–772. https://doi.org/10.1002/anie.200390203

Song, J., Babayekhorasani, F., & Spicer, P. T. (2019). Soft bacterial cellulose microcapsules with adaptable shapes. *Biomacromolecules*, *20*(12), 4437–4446. https://doi.org/10.1021/acs.biomac.9b01143

Squires, T. M., & Quake, S. R. (2005). Microfluidics: Fluid physics at the nanoliter scale. *The*

American Physical Society, *77*(3), 977–1026.

Staben, M. E., Zinchenko, A. Z., & Davis, R. H. (2006). Dynamic simulation of spheroid motion between two parallel plane walls in low-Reynolds-number Poiseuille flow. *Journal of Fluid Mechanics*, *553*, 187–226. https://doi.org/10.1017/S0022112006008731

Stauffer, C. E. (1965). The measurement of surface tension by the pendant drop technique. *Journal of Physical Chemistry*, *69*(6), 1933–1938. https://doi.org/10.1021/j100890a024

Stone, H. A. (1994). Dynamics of drop deformation and breakup in viscous fluids. *Annual Review of Fluid Mechanics*, *26*(1), 65–102. https://doi.org/10.1146/annurev.fl.26.010194.000433

Stone, H. A., Bentley, B. J., & Leal, L. G. (1986). An experimental study of transient effects in the breakup of viscous drops. *Journal of Fluid Mechanics*, *173*, 131–158. https://doi.org/10.1017/S0022112086001118

Sugiura, S., Nakajima, M., Iwamoto, S., & Seki, M. (2001). Interfacial tension driven monodispersed droplet formation from microfabricated channel array. *Langmuir*, *17*(18), 5562–5566. https://doi.org/10.1021/la010342y

Surh, J., Jeong, Y. G., & Vladisavljević, G. T. (2008). On the preparation of lecithin-stabilized oil-in-water emulsions by multi-stage premix membrane emulsification. *Journal of Food Engineering*, *89*(2), 164–170. https://doi.org/10.1016/j.jfoodeng.2008.04.023

Suzuki, K., Fujiki, I., & Hagura, Y. (1998). Preparation of corn oil/water and water/corn oil emulsions using PTFE membranes. *Food Science and Technology International, Tokyo*, *4*(2), 164–167. https://doi.org/10.3136/fsti9596t9798.4.164

Tabeling, P. (2005). *Introduction to Microfluidics*. Oxford University Press.

Tan, Y. C., & Lee, A. P. (2005). Microfluidic separation of satellite droplets as the basis of a

monodispersed micron and submicron emulsification system. *Lab on a Chip*, *5*(10), 1178–1183. https://doi.org/10.1039/b504497a

Tanemura, M., Ogawa, T., & Ogita, N. (1983). A new algorithm for thre-dimensional Voronoi tessellation. *Journal of Computational Physics*, *207*, 191–207.

Tawfik, D. S., & Griffiths, A. D. (1998). Man-made cell-like compartments for molecular evolution. *Nature Biotechnology*, *16*(7), 652–656. https://doi.org/10.1038/nbt0798-652

Taylor, G. I. (1932). The viscosity of a fluid containing small drops of another fluid. *Proceedings of the Royal Society of London. Series A, Containing Papers of a Mathematical and Physical Character*, *138*(834), 41–48. https://doi.org/10.1098/rspa.1932.0169

Taylor, G. I. (1934). The formation of emulsions in definable fields of flow. *Proceedings of the Royal Society of London. Series A, Containing Papers of a Mathematical and Physical Character*, *146*(858), 501–523. https://doi.org/10.1098/rspa.1934.0169

Teh, S. Y., Lin, R., Hung, L. H., & Lee, A. P. (2008). Droplet microfluidics. *Lab on a Chip*, *8*(2), 198–220. https://doi.org/10.1039/b715524g

Temam, R. (Ed.). (1977). *Chapter I - The Steady-State Stokes Equations*, *Studies in Mathematics and Its Applications*. Elsevier. https://doi.org/https://doi.org/10.1016/S0168-2024(09)70069-4

Thorsen, T., Roberts, R. W., Arnold, F. H., & Quake, S. R. (2001). Dynamic pattern formation in a vesicle-generating microfluidic device. *Physical Review Letters*, *86*(18), 4163–4166. https://doi.org/10.1103/PhysRevLett.86.4163

Tice, J. D., Song, H., Lyon, A. D., & Ismagilov, R. F. (2003). Formation of droplets and mixing in multiphase microfluidics at low values of the Reynolds and the capillary numbers. *Langmuir*, *19*(22), 9127–9133. https://doi.org/10.1021/la030090w

Tjahjadi, M., Ottino, J. M., & Stone, H. A. (1992). Satellite and subsatellite formation in capillary breakup. *Journal of Fluid Mechanics*, *243*, 297–317. https://doi.org/10.1017/S0022112092002738

Trofa, M., Villone, M. M., D'Avino, G., Hulsen, M. A., Netti, P. A., & Maffettone, P. L. (2016). Numerical simulations of the separation of elastic particles in a T-shaped bifurcation. *Journal of Non-Newtonian Fluid Mechanics*, *233*, 75–84. https://doi.org/10.1016/j.jnnfm.2016.01.015

Tsai, T. M., & Miksis, M. J. (1994). Dynamics of a drop in a constricted capillary tube. *Journal of Fluid Mechanics*, *274*, 197–217. https://doi.org/10.1017/S0022112094002090

Uijttewaal, W. S. J., Nijhof, E. J., & Heethaar, R. M. (1992). Droplet migration, deformation, and orientation in the presence of a plane wall: A numerical study compared with analytical theories. *Physics of Fluids A*, *5*(4), 819–825. https://doi.org/10.1063/1.858629

Umbanhowar, P. B., Prasad, V., & Weitz, D. A. (2000). Monodisperse emulsion generation via drop break off in a coflowing stream. *Langmuir*, *16*(2), 347–351. https://doi.org/10.1021/la990101e

Unverdi, S. O., & Tryggvason, G. (1992). A front-tracking method for viscous, incompressible, multi-fluid flows. *Journal of Computational Physics*, *100*(1), 25–37. https://doi.org/10.1016/0021-9991(92)90307-K

Van Der Graaf, S., Steegmans, M. L. J., Van Der Sman, R. G. M., Schroën, C. G. P. H., & Boom, R. M. (2005). Droplet formation in a T-shaped microchannel junction: a model system for membrane emulsification. *Colloids and Surfaces A: Physicochemical and Engineering Aspects*, *266*(1–3), 106–116. https://doi.org/10.1016/j.colsurfa.2005.06.019

Van Der Zwan, E. A., Schroën, C. G. P. H., & Boom, R. M. (2008). Premix membrane

emulsification by using a packed layer of glass beads. *AIChE Journal*, *54*(8), 2190–2197. https://doi.org/10.1002/aic.11508

Van Der Zwan, E., Schroën, K., Van Dijke, K., & Boom, R. (2006). Visualization of droplet break-up in pre-mix membrane emulsification using microfluidic devices. *Colloids and Surfaces A: Physicochemical and Engineering Aspects*, *277*(1–3), 223–229. https://doi.org/10.1016/j.colsurfa.2005.11.064

Van Dijke, K., Kobayashi, I., Schroën, K., Uemura, K., Nakajima, M., & Boom, R. (2010). Effect of viscosities of dispersed and continuous phases in microchannel oil-in-water emulsification. *Microfluidics and Nanofluidics*, *9*(1), 77–85. https://doi.org/10.1007/s10404-009-0521-7

Vanapalli, S. A., Banpurkar, A. G., Van Den Ende, D., Duits, M. H. G., & Mugele, F. (2009). Hydrodynamic resistance of single confined moving drops in rectangular microchannels. *Lab on a Chip*, *9*(7), 982–990. https://doi.org/10.1039/b815002h

Vasiljevic, D., Parojcic, J., Primorac, M., & Vuleta, G. (2006). An investigation into the characteristics and drug release properties of multiple W/O/W emulsion systems containing low concentration of lipophilic polymeric emulsifier. *International Journal of Pharmaceutics*, *309*, 171–177. https://doi.org/10.1016/j.ijpharm.2005.11.034

Vehring, R. (2008). Pharmaceutical particle engineering via spray drying. *Pharmaceutical Research*, *25*(5), 999–1022. https://doi.org/10.1007/s11095-007-9475-1

Villone, M. M., Trofa, M., Hulsen, M. A., & Maffettone, P. L. (2017). Numerical design of a T-shaped microfluidic device for deformability-based separation of elastic capsules and soft beads. *Physical Review E*, *96*(5), 053103. https://doi.org/10.1103/PhysRevE.96.053103

Vladisavljević, G. T. (2019). Preparation of microemulsions and nanoemulsions by membrane

emulsification. *Colloids and Surfaces A: Physicochemical and Engineering Aspects*, *579*, 123709. https://doi.org/10.1016/j.colsurfa.2019.123709

Vladisavljević, G. T., Kobayashi, I., & Nakajima, M. (2012). Production of uniform droplets using membrane, microchannel and microfluidic emulsification devices. *Microfluidics and Nanofluidics*, *13*(1), 151–178. https://doi.org/10.1007/s10404-012-0948-0

Vladisavljević, G. T., Shimizu, M., & Nakashima, T. (2004). Preparation of monodisperse multiple emulsions at high production rates by multi-stage premix membrane emulsification. *Journal of Membrane Science*, *244*(1–2), 97–106. https://doi.org/10.1016/j.memsci.2004.07.008

Vladisavljević, Goran T., Shimizu, M., & Nakashima, T. (2004). Preparation of monodisperse multiple emulsions at high production rates by multi-stage premix membrane emulsification. *Journal of Membrane Science*, *244*(1–2), 97–106. https://doi.org/10.1016/j.memsci.2004.07.008

Volk, A., & Kähler, C. J. (2018). Density model for aqueous glycerol solutions. *Experiments in Fluids*, *59*(5), 1–4. https://doi.org/10.1007/s00348-018-2527-y

Walstra, P. (1993). Principles of emulsion formation. *Chemical Engineering Science*, *48*(2), 333–349. https://doi.org/10.1016/0009-2509(93)80021-H

Wang, H., Zetterlund, P. B., Boyer, C., Boyd, B. J., Atherton, T. J., & Spicer, P. T. (2018). Large hexosomes from emulsion droplets: Particle shape and mesostructure control. *Langmuir*, *34*(45), 13662–13671. https://doi.org/10.1021/acs.langmuir.8b02638

Wang, J., Byrne, J. D., Napier, M. E., & Desimone, J. M. (2011). More effective nanomedicines through particle design. *Small*, *7*(14), 1919–1931. https://doi.org/10.1002/smll.201100442

Wang, J. T., Wang, J., & Han, J. J. (2011). Fabrication of advanced particles and particle-based

materials assisted by droplet-based microfluidics. *Small*, *7*(13), 1728–1754. https://doi.org/10.1002/smll.201001913

Wang, K., Lu, Y. C., Xu, J. H., Tan, J., & Luo, G. S. (2011). Generation of micromonodispersed droplets and bubbles in the capillary embedded T-junction microfluidic devices. *AIChE Journal*, *57*(2), 299–306. https://doi.org/10.1002/aic.12263

Wang, X., Liu, Z., & Pang, Y. (2019). Breakup dynamics of droplets in an asymmetric bifurcation by MPIV and theoretical investigations. *Chemical Engineering Science*, *197*, 258–268. https://doi.org/10.1016/j.ces.2018.12.030

Wang, Z., Sui, Y., Salsac, A. V., Barthès-Biesel, D., & Wang, W. (2018). Path selection of a spherical capsule in a microfluidic branched channel: towards the design of an enrichment device. *Journal of Fluid Mechanics*, *849*, 136–162. https://doi.org/10.1017/jfm.2018.414

Weigl, B., Domingo, G., LaBarre, P., & Gerlach, J. (2008). Towards non- and minimally instrumented, microfluidics-based diagnostic devices. *Lab on a Chip*, *8*(12), 1999–2014. https://doi.org/10.1039/b811314a

Woolfenden, H. C., & Blyth, M. G. (2011). Motion of a two-dimensional elastic capsule in a branching channel flow. *Journal of Fluid Mechanics*, *669*, 3–31. https://doi.org/10.1017/S0022112010004829

Xu, J. H., Li, S. W., Chen, G. G., & Luo, G. S. (2006). Formation of monodisperse microbubbles in a microfluidic device. *AIChE Journal*, *52*(6), 2254–2259. https://doi.org/10.1002/aic.10824

Yong, Y., Yang, C., Jiang, Y., Joshi, A., Shi, Y., & Yin, X. (2011). Numerical simulation of immiscible liquid-liquid flow in microchannels using lattice Boltzmann method. *Science China Chemistry*, *54*(1), 244–256. https://doi.org/10.1007/s11426-010-4164-z

Zhang, Z., Drapaca, C., Chen, X., & Xu, J. (2017). Droplet squeezing through a narrow constriction: Minimum impulse and critical velocity. *Physics of Fluids*, *29*(7), 072102. https://doi.org/10.1063/1.4990777

Zhao, W., & Van Den Berg, A. (2008). Lab on paper. *Lab on a Chip*, *8*(12), 1988–1991. https://doi.org/10.1039/b814043j

Zhou, H., & Pozrikidis, C. (1994). Pressure-driven flow of suspensions of liquid drops. *Physics of Fluids*, *6*(1), 80–94. https://doi.org/10.1063/1.868048

Zinchenko, A. Z., Ashley, J. F., & Davis, R. H. (2012). A moving-frame boundary-integral method for particle transport in microchannels of complex shape. *Physics of Fluids*, *24*(4), 043302. https://doi.org/10.1063/1.4704816

Zinchenko, A. Z., & Davis, R. H. (2000). An efficient algorithm for hydrodynamical interaction of many deformable drops. *Journal of Computational Physics*, *157*(2), 539–587. https://doi.org/10.1006/jcph.1999.6384

Zinchenko, A. Z., & Davis, R. H. (2006). A boundary-integral study of a drop squeezing through interparticle constrictions. *Journal of Fluid Mechanics*, *564*, 227–266. https://doi.org/10.1017/S0022112006001479

https://doi.org/10.1017/S0022112006001479

Zinchenko, A. Z., & Davis, R. H. (2013). Emulsion flow through a packed bed with multiple drop breakup. *Journal of Fluid Mechanics*, *725*, 611–663. https://doi.org/10.1017/jfm.2013.197

Zinchenko, A. Z., & Davis, R. H. (2017). Motion of deformable drops through porous media. *Annual Review of Fluid Mechanics*, *49*(1), 71–90. https://doi.org/10.1146/annurev-fluid-010816-060331

Zinchenko, A. Z., & Davis, R. H. (2008). Squeezing of a periodic emulsion through a cubic lattice of spheres. *Physics of Fluids*, *20*(4), 040803. https://doi.org/10.1063/1.2912119

Zinchenko, A. Z., Rother, M. A., & Davis, R. H. (1997). A novel boundary-integral algorithm for viscous interaction of deformable drops. *Physics of Fluids*, *9*(6), 1493–1511. https://doi.org/10.1063/1.869275

Zinchenko, A. Z., Rother, M. A., & Davis, R. H. (1999). Cusping, capture, and breakup of interacting drops by a curvatureless boundary-integral algorithm. *Journal of Fluid Mechanics*, *391*, 249–292. https://doi.org/10.1017/S0022112099005285

Appendix A.

Comparison of steady velocities in a straight channel

Table A1. Drop velocities in a straight channel.

R	Ca	λ	N_Δ	Method	U/U_c
0.3	0.333	1	6000	A = 3, MFBIM	0.9215
				A = 4.5, MFBIM	0.9203
				A = 5, MFBIM	0.9201
				A = ∞, MFBIM	0.9193
				2WBIM	0.9192
0.49	0.167	1	8640	A = 3, MFBIM	0.7927
				A = 4.5, MFBIM	0.7875
				A = 6, MFBIM	0.7854
				A = ∞, MFBIM	0.7836
				2WBIM	0.7841
0.635	0.333	1	8640	A = 3, MFBIM	0.8117
				A = 4.5, MFBIM	0.8098

				A = 6, MFBIM	0.8096
				A = ∞, MFBIM	0.8094
				2WBIM	0.8090
0.635	0.333	4	8640	A = 3, MFBIM	0.7294
				A = 4.5, MFBIM	0.7202
				A = 6, MFBIM	0.7181
				A = ∞, MFBIM	0.7154
				2WBIM	0.7176

Average drop velocity parallel to walls of a long and wide channel with two parallel walls, using the MF algorithm with different frame sizes and using the exact two-wall Green's function.

Appendix B.

Details of the stream function evaluation

Evaluating the integral

$$R(\Lambda)=\frac{3}{2\pi}\int_{-1/2}^{1/2}\left[1-(2y)^2\right]e^{i\Lambda y}dy=\frac{12}{\pi\Lambda^2}\left[\frac{2\sin(\Lambda/2)}{\Lambda}-\cos(\Lambda/2)\right] \tag{B1}$$

and using the inverse Fourier transform, we obtain

$$\int_0^\infty R(\Lambda)\cos(\Lambda y)\,d\Lambda=\begin{Bmatrix}\frac{3}{2}[1-(2y)^2]\ \text{for}\ |y|\le\frac{1}{2}\\ 0\qquad\qquad\ \text{for}\ |y|\ge\frac{1}{2}\end{Bmatrix}. \tag{B2}$$

Using (2.18), (2.19) and (B2), a system of equations easily follows from the boundary conditions:

$$\begin{aligned}
&Ae^{-\Lambda}-Be^{-\Lambda}+C=R(\Lambda),\\
&Ae^{-\Lambda}\Lambda+Be^{-\Lambda}(1-\Lambda)-C\Lambda+D=0,\\
&A+Ce^{-\Lambda}+De^{-\Lambda}=0,\\
&A\Lambda+B-Ce^{-\Lambda}\Lambda+De^{-\Lambda}(1-\Lambda)=0,
\end{aligned} \tag{B3}$$

which can be solved for *A*, *B*, *C* and *D* at every Λ. However, the integrals (2.18) are slowly convergent for small *z* (which may present difficulties when a large drop spans the entire gap between the walls). A useful yet simple additional step is to first subtract the leading behaviors

$C \sim R(\Lambda)$, $D \sim \Lambda R(\Lambda)$ from C and D before calculating $\boldsymbol{u}_\infty$ by (2.18). The added-back contribution to $\boldsymbol{u}_\infty(y_0, z_0)$ comes from

$$-\frac{3}{\pi} z_0^2 \int_{-1/2}^{1/2} \frac{\left[1-(2y)^2\right]\mathbf{r}}{r^4} dy \tag{B4}$$

with $\mathbf{r} = (y - y_0, -z_0)$, and is evaluated analytically.

Appendix C.

Sensitivity of partitioning to triangulation and smoothing

Table C1 shows the volume partitioning into the stem of the T-channel for several flow ratios and number of triangles used to discretize the drop surface. There is only a weak effect of the discretization, with all discretizations predicting that the drop goes into the straight branch for $Q_1/Q_2 = 0.25$, goes into the side (stem) branch for $Q_1/Q_2 = 3.6$, and partitions between these two branches for $0.3 < Q_1/Q_2 < 3.5$. Moreover, the volume of the daughter drop partitioning to the side branch (V_1) changes by no more than 1% of the total drop volume (V) with increased resolution.

Table AII. Volume partition (V_1/V) for a drop with $R = 0.4$, Ca= 0.8, $\lambda = 1.0$, and various flow ratios and drop surface discretizations.

Q_1/Q_2	$N_\triangle = 2160$	$N_\triangle = 3840$	$N_\triangle = 6000$	$N_\triangle = 8640$
0.25	0	0	0	0
0.3	0.022	0.025	0.029	0.032
0.75	0.376	0.372	0.374	0.375
1.5	0.704	0.712	0.717	0.717
3.5	0.991	0.992	0.992	0.992
3.6	1	1	1	1

The left panel of Figure C1 shows additional results for the volume partitioning from the lowest and highest resolutions, showing excellent agreement. The right panel in Figure C1 shows similar results but for a fixed triangulation of $N_\Delta = 2160$ and different sizes of the panels used to

smooth the corners. The volume partitioning is the same for $h = 0.075H, 0.10H$, and $0.125H$, except near the critical flow ratios, which determine whether the drop breaks or proceeds into one of the branches without breaking.

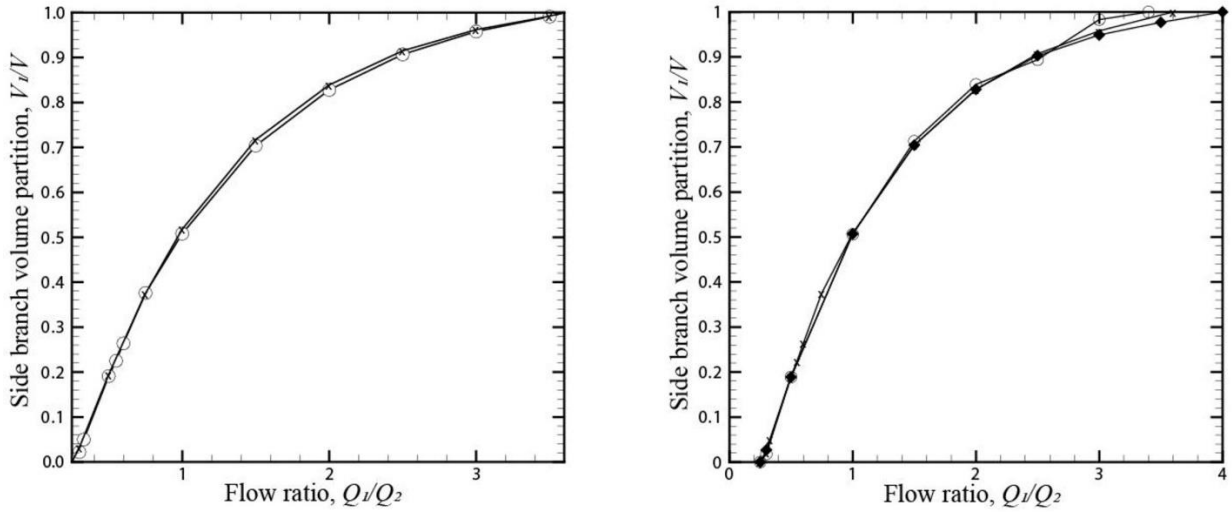

Figure C1. Volume partition ratios for different drop triangulations and corner smoothing.

Volume partition of the drop going through the side branch of the channel versus flow ratio for R = 0.4, Ca = 0.8, and λ = 1.0, with $h = 0.1H$ and $N_\triangle$ = 2160 (○) and 8640 (×) for the left panel. For the right panel, $N_\triangle$ = 2160, with corners smoothed by three panels, each of length 3.9% (◆), 5.2 % (╳) or 6.5% (○) of the channel height, so the values of the circle radius h inscribed into the corner (see Section 2.5) are in a range of 10% ± 2.5% of the channel height H.

The results obtained for completely sharp corners (0% smoothing, as in Figure 2a) are not represented in Figure C1, since it was not possible to determine the volume partition of the drop in this case. The lack of lubrication with sharp corners does not allow us to proceed far enough to an impending breakup. However, it is possible to calculate the critical flow ratio range when the drop is not able to go completely through one of the branches without breaking, which is Q_1/Q_2 = [0.25, 4.2] for sharp corners, so the drop will hit the corner for any value of Q_1/Q_2 within this range.